Alma Mater Studiorum – Università di Bologna

DOTTORATO DI RICERCA IN SCIENZE CHIMICHE

Ciclo XXI

Settore scientifico disciplinari di afferenza: CHIM/03

INTERACTION BETWEEN BIOMIMETIC INORGANIC MATERIALS AND BIOMOLECULES: TOWARDS NANOTECHNOLOGICAL APPLICATIONS

Presentata da: Dr. Michele Iafisco

Coordinatore Dottorato **Relatore**

Chiar.mo Prof. Giuliano Longoni **Chiar.mo Prof. Norberto Roveri**

Bologna 2009

INTERACTION BETWEEN BIOMIMETIC INORGANIC MATERIALS AND BIOMOLECULES: TOWARDS NANOTECHNOLOGICAL APPLICATIONS

ABSTRACT

Hydroxyapatite (HA), [$Ca_{10}(PO_4)_6(OH)_2$], is one of the most stable forms of the calcium orthophosphates and the major inorganic component of bone and teeth in mammals. HA is object of extensive research in numerous interdisciplinary areas from a better understanding the mechanisms of formation in natural mineralization processes to applicability as a biomedical or industrial material. The biocompatibility, bioactivity, bioreasorbibility, osteoconductivity, size dimension, morphology and surface functionalisation represent the physical-chemical properties which should be tailored in synthetic HA crystals for optimising their specific biomedical applications.

The recent trend in biomaterials research is focused on overcoming the limitations of calcium phosphates, precisely hydroxyapatite ceramics and in improving their biological properties via exploring the unique advantages of nanotechnology. The trend is shifting towards nanotechnology to improve the biological responses of HA because nano-HA is a constituent of bone.

The use of nano-HA in orthopedics is therefore considered to be very promising, owing to its dimensional similarity with the bone crystals. It has been established that nanotechnology offers a unique approach to overcome shortcomings of many conventional materials. From nanomedicine to nanofabrics, this promising technology has encompassed almost all disciplines of human life. Nanostructured materials offer much improved performances than their larger particle sized counterparts due to their large surface to volume ratio and unusual chemical/electronic synergistic effects.

The surface functionalization of HA nano-crystals with bioactive molecules makes them able to transfer information to and to act selectively on the biological environment, and this represents a main challenge for innovative bone substitute materials. In this context, the synthesis of apatite nanocrystals loaded with antitumor drugs that can be released by a controlled kinetic process represents an attractive goal. The application of such a material to the chemotherapeutic treatments of osteosarcoma could result in tumor inhibition accompanied by low levels of systemic toxicity.

One of the aim of the this thesis is to develop new biomimetic apatite nanocrystals for potential use in bone implantation, which in addition function as a local targeted delivery system for anti-cancer and anti–metastatic drugs with controlled release properties. The adsorption and release of bioactive molecules are strongly affected not only by the chemical properties of the drug molecule but also by the chemical and structural characteristics of the HA substrates. Thus, in this study we have

investigated the adsorption and release of several anti-cancer drug using different bio-mimetic synthetic hydroxyapatite nanocrystals with different physico-chemical properties.

In the biomaterials field, protein-surface adhesion is the first event in the integration of an implanted device or material with biological tissues. The exposure of biomaterials to plasma proteins, blood or biological fluids normally leads to the adsorption of blood proteins onto the biomaterials surface. The adsorbed protein layer can further mediate additional biological responses, such as cell attachment and activation, and can create unpredicted perturbations to device operation. Although protein adsorption on solid surfaces has been widely studied for decades, its mechanisms are still far from being fully understood.

Consequently the next step of this research is to study of the affinity of myoglobin, human and bovine serum albumin (model proteins) towards hydroxyapatite nanocrystals and how the inorganic substrate affects the structure of proteins and to compare protein affinity versus the drug surface functionalization of biomimetic HA with the one respect to unfunctionalized HA.

For a material to be bioactive, bonds must be formed between its surface and the living bone, such that it becomes covered with an apatite layer. From this initial layer, the osteoblast of living bone can proliferate and produce apatite and collagen, a process termed osteointegration. Recently, it has been shown that glasses of type Na_2O-CaO-SiO_2 are materials that favour this formation. This is because these materials interchange Na^+ and Ca^{2+} ions with protons in the surrounding fluid which gives rise to Si-OH groups that induce the nucleation of hydroxyapatite. Based on this property of silicate matrices, the possibility of coating synthetic calcium phosphates with porous silica layers, which could serve both to enhance bioactivity and tune biocomposite dissolution rate, is investigated.

The last aim is the design of biomimetic carbonate-hydroxyapatite nanocrystals in order to obtain a new remineralization method of the altered enamel surfaces, highlighting the effect of the hydroxyapatite respect the fluoride ions. In fact dental erosion is the chemical wear of the dental hard tissue without the involvement of bacteria and its clinical relevance is becoming wider and wider so that it is considered one of the main tooth pathologies able to cause patient discomfort, after periodontal diseases and caries.

KEYWORDS

Hydroxyapatite; Nanocrystals; Drug delivery; Cisplatin; Alendronate; Myoglobin; Human serum albumin; Bovine serum albumin; Silica gel; Remineralization; Dental erosion.

CHAPTER 1: INTRODUCTION

CHAPTER 2: EXPERIMENTAL TECHNIQUES

CHAPTER 3: BIOMIMETIC HYDROXYAPATITE NANOCRYSTALS AS BONE SUBSTITUTE WITH DRUGS DELIVERY FUNCTION

CHAPTER 6: SURFACE ENAMEL REMINERALIZATION: HYDROXYAPATITE CRYSTALS VS FUORIDE IONS

APPENDIX

CHAPTER 1
INTRODUCTION

1.1 BONE

Bone is a mineralized matrix, a complex composite of biopolymer and biomineral. The biopolymer consists of matrix proteins, mostly collagen (type 1) with some minor but important noncollagenous proteins (e.g., proteoglycans), minor amounts of lipids and osteogenic factors (e.g., bone morphogenetic proteins, BMPs) (Boskey, 2000; Cowles *et al.*, 1998; Marks *et al*., 1996; Reddi, 1994). Bone is formed by a series of complex events rigorously orchestrated by different types of bone cells interacting with each other and with the extracellular matrix. The bone cells include (i) osteoblasts, (ii) osteoclasts, (iii) osteocytes, and (iv) bone-lining cells. Osteoblasts are responsible for production and mineralization of the bone matrix; osteoclasts maintain the bone matrix; osteoclasts are responsible for bone resorption. Cell attachment, proliferation, and differentiation are important activities involved in bone formation. The osteoblast (bone-forming) cells attach, proliferate, and differentiate, leading to production of matrix proteins that include collagen (mostly type 1), osteopontin (OSP), bone sialoprotein (BSP), osteonectin (ONN), osteocalcin (OSC), fibronectin (FN), and BMPs before mineral deposition (Boskey, 2000; Cowles *et al.*, 1998; Marks *et al*., 1996; Reddi, 1994; Urist, 1965; Urist *et al.*, 1967; Wozney, 1992; Termine *et al.*, 1981). BMPs and matrix proteins induce bone formation in vitro and in vivo. Collagen, OSP, and ONN have been shown in vitro to nucleate apatite formation and also inhibit or modulate apatite crystal growth.

As the primary structural support of the mammalian body,bones are constantly being remodeled in response to the applied stresses. This continuous regeneration of bone likely serves to repair fatigue damage and prevent excessive aging (Manolagas, 2000). In addition to its structural functions of load bearing, internal organ protection, and muscle support, bone is also important for the tight regulation of calcium ion concentration through the ongoing resorption and formation of new mineral. There are two cell types that are responsible for the formation, removal, and maintenance of bone tissue. Osteoblasts are mononuclear cells primarily responsible for bone formation. Osteoclasts are multinuclear, macrophage-like cells that resorb bone.

Important physicochemical properties of bone include (i) interconnecting porosity, (ii) biodegradability, (iii) bioactivity, (iv) osteoconductivity, and (v) osteoinductivity. Pore size ranges from 10 to 50 μm and 100 to 300 nm in cortical bone and 200 to 600 μm in trabecular bone. The size and interconnection of bone porosity is essential for vascularization, diffusion of nutrients and

cells, and tissue ingrowths. The bone architecture and composition allows cell attachment, migration, proliferation, and differentiation, promoting bone formation, repair, and regeneration.

To better understand the complex bone architecture, several hierarchical models have been proposed. Weiner and Wagner have identified seven discrete levels of hierarchical organization in bone (Figure 1.1), which we describe here (Weiner *et al.*, 1998). In their model, bone is considered as a family of materials with the mineralized collagen fiber as the primary building block for subsequent higher order architectures.

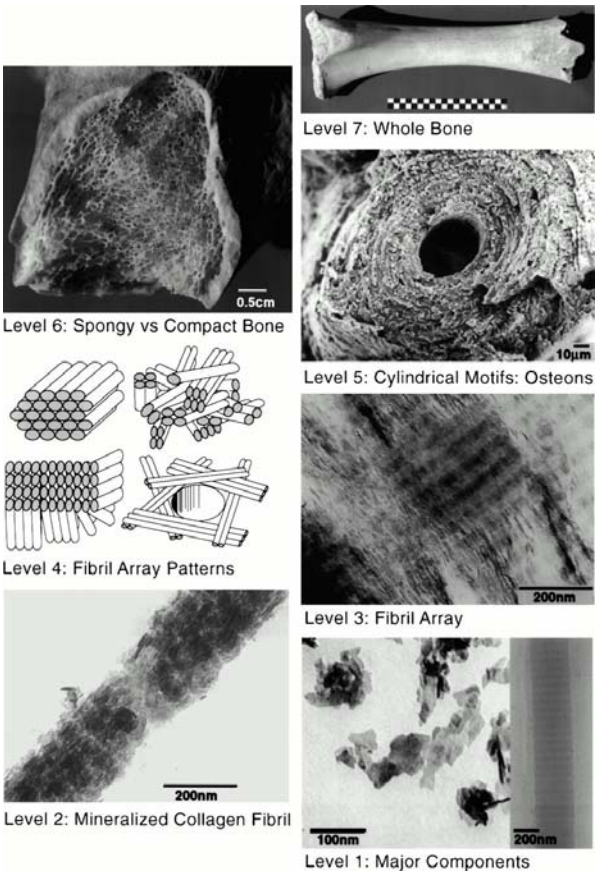

Figure 1.1 Seven hierarchical levels of organization of the bone family of materials as proposed by Weiner and Wagner.

The structure of bone varies greatly among different locations in the skeleton, but the basic nanoscale structure of bone consisting of mineralized collagen remains the same throughout (Weiner *et al.*, 1998). Mann has presented a similar structural hierarchy containing six levels (Mann, 2001).

The first level of hierarchy consists of the molecular components: water, HA, collagen, and other proteins. The crystals of HA are plate-shaped and are among the smallest known biological crystals (30-50 nm long, 20-25 nm wide, and 1.5-4 nm thick, depending on the study) (Table 1.1).

In early studies, apatite needles were observed (Fernandez-Moran *et al.*, 1957), but more recent studies suggest that platelets are the dominant morphology and that the apparent needles are most likely to be platelets viewed edge-on (Traub *et al.*, 1989).

Table 1.1 Characterization of bone crystallites using different analytical methods

analytical method	crystal dimensions
TEM	3-6 nm diameter × 20 nm long
XRD	10-35 nm long
SAXS	50 nm × 25 nm × 1.5-4 nm
SAXS and TEM	30 nm × 20 nm × 1.5-2 nm

Noncollagenous proteins (NCPs) are also present but make up 10% or less of the total protein content in the bone matrix. The specific functions of the NCPs are still not completely understood. In addition to influencing crystal nucleation and growth, NCPs also play roles in cell signaling and ion homeostasis (Feng *et al.*, 2006).

The second level is formed by the mineralization of collagen fibrils. This platelet-reinforced fibril composite is described by Weiner and Wagner as containing parallel platelike HA crystals with their *c*-axis aligned with the long axis of the fibril (Schmidt, 1936). The location of these crystals in the fibril was demonstrated in a study by Traub et al. that showed that mineralized collagen fibrils had the same banded pattern as negatively stained collagen fibrils. This indicated that mineral is concentrated in the hole zones of the fibril, as described in the next section. It was proposed that these mineral platelets were arranged in parallel like a stack of cards within the interstices of the fibril. Olszta et al. concluded from electron diffraction studies that that the mineral plates are not quite as ordered as previously assumed (Olzsta *et al.*, 2007). This imperfect arrangement of nearly parallel crystals has been supported by recent SAXS and transmission electron microscopy (TEM) data from Burger et al (Burger *et al.*, 2008).

The third level of hierarchy is composed of arrays of these mineralized collagen fibrils. These fibrils are rarely found isolated but rather almost always associated as bundles or other arrangements, often aligned along their long axis. The fourth level is the patterns of arrays that are formed. These include parallel arrays, woven arrangements, plywood like structures, and radial arrays like those found in dentin (Weiner *et al.*, 1997). Cylindrical structures called osteons make up the fifth level. Osteons are formed with significant cellular activity and remodeling; osteoclasts resorb bone and form a tunnel, and osteoblasts subsequently lay down lamellae in stacked layers until only a small channel (Haversian canal) is left behind. These channels serve as a conduit for nerves and blood

supply to the bone cells. The sixth level of bone organization is the classification of osseous tissue as either spongy (trabecular or cancelous) or compact (cortical). Cancellous bone is extremely porous (75-95% porosity), providing space for marrow and blood vessels, but has much lower compressive strength. Cortical bone is the dense outer layer (5-10% porosity) that allows the many of the support functions of bone. Therefore, the mechanical properties of cortical bone represent the benchmark for synthetic bone (Rho *et al.*, 1998). The seventh level is simply the whole bone on the macroscopic scale, incorporating all of the lower levels of hierarchy. There are 206 bones in the adult human skeleton, the structure of which depends on the location and function.

1.2 TOOTH

The mammalian body contains numerous mineralized tissues; the tissue with the most robust mechanical properties is enamel. Enamel is the hardest material formed by vertebrates and is the most highly mineralized skeletal tissue present in the body (Robinson, 1995). Mature enamel is composed of 95-97% carbonated HA by weight with less than 1% organic material. The high degree of mineralization makes enamel a fascinating model for understanding fundamental mineralization processes and processes that occur within an extracellular matrix. It is distinct from bone in terms of architecture, pathology, and the biological mechanisms mediating its formation. Understanding the biological formation of different mineralized structures could lead to innovative approaches toward engineering novel scaffolds and providing new therapeutics. Additionally, unlike other biomineralized tissues, such as bone and dentin, mature enamel is acellular and does not resorb or remodel. As a result, enamel regeneration cannot occur in vivo following failure and is therefore an attractive target for future biomimetic and therapeutic approaches.

Enamel formation, or amelogenesis, is a highly regulated process involving precise genetic control as well as protein-protein interactions, protein-mineral interactions, and interactions involving the cell membrane.

The mammalian tooth is made up of four distinct structures: enamel, dentin, pulp, and cementum (Figure 1.2) (Tamerler *et al.*, 2008).

The pulp contains nerves, blood vessels, fibroblasts, and lymphocytes, while the mineralized organs of the tooth include enamel, dentin, and cementum. Enamel makes up the uppermost 1-2 mm of the tooth crown and contains a high mineral content, giving it a high modulus but also making it susceptible to cracking. Dentin lies below the enamel and is tougher, forming the bulk of the tooth and absorbing stresses from enamel, preventing its fracture (Ten Cate, 1994). The composition of dentin is similar to that of bone. The cementum is the mineralized layer that surrounds the root of

the tooth covering the dentin layer and some of the enamel layer. The cementum allows for the anchoring of the tooth to the alveolar bone (jawbone) through the periodontal ligament. The primary function of the tooth is for mastication of food; however, some species use them for attacking prey and for defense. It also faces the lifelong challenge of maintaining robust mechanical properties in a bacteria-filled environment.

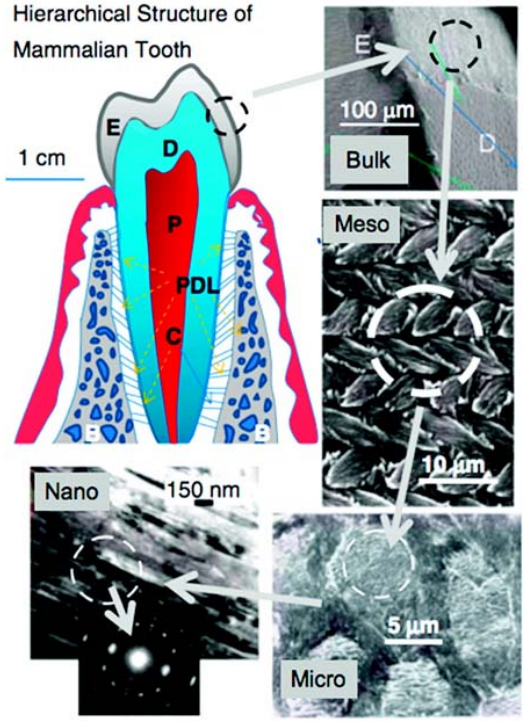

Figure 1.2 Hierarchical architecture of mammalian enamel. Enamel (E) is the outermost layer at the crown of the tooth and resides above the dentin (D). The pulp (P) contains nerves and blood vessels, while the cementum (C) is the outermost layer of mineralized tissue surrounding the root of the tooth allowing the tooth to be anchored to the jawbone through the periodontal ligament (PDL). The bulk image depicts the enamel organ, the transition across the dentino-enamel junction, and the dentin below. On the mesoscale level, prismatic enamel consisting of weaving of rods (or prisms) that range from 3 to 5 µm in diameter can be visualized. Upon further magnification, the micrometer scale shows the composition of a single rod. The nanometer scale reveals a highly organized array of individual HA crystallites (approximately 30 nm thick, 60 nm wide, and several millimeters in length), which are preferentially aligned along the c-axis.

The enamel and dentin tissues give rise to a tough, crack-tolerant, and abrasion-resistant tissue through their unique architectures and mineral compositions. Enamel is highly patterned and consists of organized interweaving bundles of crystallites (called rods or prisms). It has a higher reported toughness than that of crystalline HA, indicating that the organization of the crystallites is

essential for enamel function (White *et al.*, 2001). Because of the high mineral content and minimal organic, enamel is brittle. Interestingly, the architecture of the enamel crystallites can deflect a propagating crack preventing it from reaching the dentin-enamel junction (DEJ), which also has been shown to resist delamination of the tissues despite their differences in composition (Imbeni *et al.*, 2005). The mechanical properties of enamel, dentin, and the DEJ are not completely understood and are a significant area of research. Understanding the properties of these tissues could serve to motivate further engineering of more robust dental materials as well as to inspire fabrication of nonbiological materials.

Similar to bone, enamel possesses a complex architecture, which can be broken into several hierarchical levels from the nanoscale to the macroscale (Paine *et al.*, 2001). On the nanoscale, the protein-protein and protein-mineral interactions in the presence of supersaturated ions create a highly organized array of HA crystallites that grow preferentially along the c-axis (Wen *et al.*, 2000). The sizes of these crystallites vary depending on the stage of the mineralization. The crystallites grow primarily in length during the secretory stage and continue to grow in width and thickness during the maturation stage. The assembly of amelogenin has been shown to be crucial for the proper development of enamel crystallites. Disruption of the assembly alters formation on the nanoscale, subsequently affecting larger length scales and giving rise to a diseased or malformed enamel phenotype.

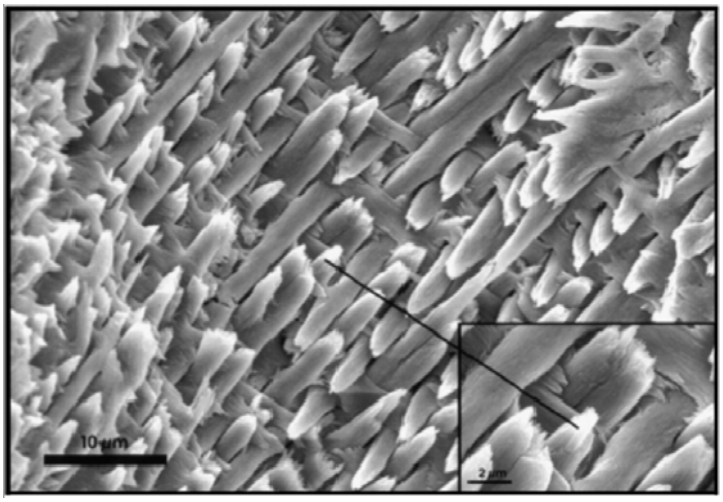

Figure 1.3 Organization of prismatic dental enamel on the mesoscale showing interweaving crystallite bundles termed as prisms or rods. This scanning electron micrograph shows an acid-etched ground section of mature mouse incisal dental enamel.

On the mesoscale level, there are three main structural components: the rod, the interrod, and the aprismatic enamel. The main component of enamel on the mesoscale includes rods, which are

bundles of aligned crystallites that are "woven" into intricate architectures that are approximately 3-5 μm in diameter, as seen in figure 1.3

The second structural component of the enamel matrix is the interrod (or interprismatic) enamel, which surrounds and packs between the rods. The difference between the rod and the interrod is the orientation of HA crystals; the rod contains aligned crystallites, whereas the mineral in the interrod is less ordered. These structures coalesce to form the tough tissue of enamel, which can withstand high forces and resist damage by crack deflection (White *et al.*, 2000). The third structure, aprismatic enamel, refers to the structures containing HA crystals that show no mesoscale or macroscale alignment.

The macroscale architecture includes specific zones of enamel that have unique characteristics, which contribute to the whole tissue. The enamel adjacent to the DEJ exhibits a gradual transition from dentin to enamel. Aprismatic regions of enamel have been proposed to be primitive areas of the tooth serving as a toughening mechanism due to their flexible nature (White *et al.*, 2000; Wang *et al.*, 1998). Several authors have identified these aprismatic areas to be located adjacent to the DEJ and at the incisal surface of both deciduous and permanent human enamel (Whittacker, 1982; Boyde, 1989; Kodaka *et al.*, 1989). The Tomes' process, a unique structure present at the secretory pole of an enamel-forming cell, is responsible for aligned mineral formation in the prismatic enamel. The absence of this process may give rise to the aprismatic zone in the tooth (Garant, 2003).

1.3 BIOGENIC CALCIUM PHOSPHATES

The bone mineral was identified as an apatite based on its similarity to the X-ray diffraction profiles of mineral apatites and their similarities in composition with each other (principally calcium and phosphate ions) (De Jong, 1926; Beevers *et al.*, 1956; McConnell, 1952). The mineral of teeth and bones was idealized as calcium hydroxyapatite (HA), $Ca_{10}(PO_4)_6(OH)_2$ (Kay *et al.*, 1964). However, biologic apatites contain minor and trace elements and are therefore not pure HA. The most important minor elements are carbonate (CO_3), magnesium (Mg), and sodium (Na). Systematic studies on synthetic carbonate-substituted apatites and biologic apatites using combined analytical methods (X-ray diffraction, infrared spectroscopy and chemical analyses) (LeGeros *et al.*, 1967; Zapanta-LeGeros, 1965; LeGeros *et al.*, 1971; LeGeros *et al.*, 1970) led to the conclusion that biologic apatites should be considered as carbonate hydroxyapatite, (LeGeros, 1981; Elliot, 1994; Rey *et al.*, 1991) CHA, approximated by the formula $(Ca,Na,Mg)_{10}(PO_4,HPO_4,CO_3)_6(OH,Cl,F)_2$ (compared to pure hydroxyapatite, HA, $Ca_{10}(PO_4)_6(OH)_2$).

Bone apatite crystals are irregularly shaped platelets of variable lengths and widths (30-45 nm) and thickness (average about 5 nm) oriented with their c axis parallel to one another and lies along the collagen fibrils (Weiner *et al.*, 1998). Biologic apatites of enamel have considerably larger crystal size (about 2000 nm) compared to that of either bone or dentin apatite, as indicated by the well-defined diffraction peaks in the XRD profile of enamel apatite (LeGeros, 1981) and much broader diffraction peaks of either bone or dentin apatite (Figure 1.4).

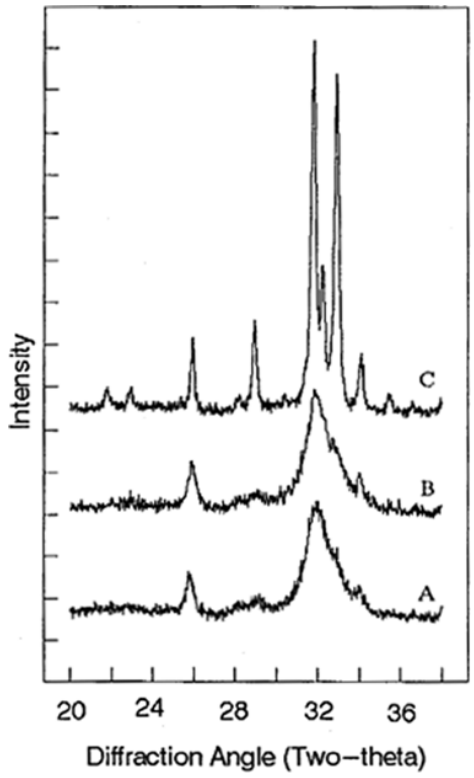

Figure 1.4 X-ray diffraction profiles of biologic apatites from (A) bone, (B) dentin, and (C) enamel. The sharper diffraction peaks in C compared to either B or A indicate that enamel apatite crystals are much larger compared to either bone or dentin apatite crystals.

The concentrations of Mg and CO_3 in enamel apatite are much lower than those in either dentin or bone apatite (LeGeros, 1991; LeGeros, 1981). The mineral phase of some fish enameloids (e.g., shark enameloid) have fluoride (F^-) ions replacing the hydroxyl (OH) groups in the apatite structure (LeGeros et al., 1983). Differences in composition affect the lattice parameters of the apatite hexagonal structure (*a* and *c* axis dimensions), crystal size, and solubility of the biological and synthetic apatites as demonstrated in the differences in crystallite size and solubility of the biologic apatites in enamel, dentin, and bone. For example, substitution of CO_3^{2-} (for PO_4^{3-}) or Mg^{2+} or Sr^{2+} (for Ca^{2+}) in the apatite structure causes a decrease in crystallite size and an increase in solubility, while incorporation of fluoride ions (F for OH^- substitution in the apatite structure) causes an

increase in crystallite size and decrease in solubility. Detailed information on the chemical composition of the most important human normal calcified tissues is given in table 1.2 (Dorozhkin *et al.*, 2002; Daculsi *et al.*, 1997; LeGeros 1991).

Table 1.2 Comparative composition and structural parameters of inorganic phases of adult-human calcified tissues[a].

Composition	Enamel	Dentin	Bone
Calcium [wt %][b]	36.5	35.1	34.8
Phosphorus (as P) [wt %][b]	17.7	16.9	15.2
Ca/P (molar ratio) [b]	1.63	1.61	1.71
Sodium [wt %][b]	0.5	0.6	0.9
Magnesium [wt %][b]	0.44	1.23	0.72
Potassium [wt %][b]	0.08	0.05	0.03
Carbonate (as CO_3^{2-}) [wt %][c]	3.5	5.6	7.4
Fluoride [wt %][b]	0.01	0.06	0.03
Chloride [wt %][b]	0.30	0.01	0.13
Pyrophosphate (as $P_2O_7^{4-}$) [wt %][c]	0.022	0.100	0.070
Total inorganic [wt %][c]	97	70	65
Total organic [wt %][c]	1.5	20	25
Water [wt %][c]	1.5	10	10
a axis [Å][d]	9.441	9.421	9.410
c axis [Å][d]	6.880	6.887	6.890
Crystallinity index, (HA=100)	70 – 75	33 - 37	33 - 37
Typical crystal sizes [nm]	100 × 50 × 50 μm	35 × 25 × 4	50 × 25 × 4
Ignition products (800 °C)	β-TCP + HA	β-TCP + HA	HA + CaO
Elasticity modulus (GPa)	80	15	0.34 - 13.8
Compressive strength (MPa)	10	100	150

[a] Because of the considerable variation found in biological samples, typical values are given in these cases. [b] Ashed samples. [c] Unashed samples. [d] Lattice parameters: ± 0.003 Å.

Other calcium phosphates also occur in biologic systems, usually in pathologic calcifications (e.g., dental calculus, urinary stones, soft-tissue calcifications) or diseased states (e.g., dental caries). Biologic nonapatitic calcium phosphates include amorphous calcium phosphate, $Ca_x(PO_4)_y \cdot zH_2O$ (ACP), dicalcium phosphate dihydrate, $CaHPO_4 \cdot 2H_2O$ (DCPD), octacalcium phosphate,

$Ca_8H_2(PO_4)_6 \cdot 5H_2O$ (OCP), Mg-substituted tricalcium phosphate, $(Ca,Mg)_3(PO4)_2$ (β-TCMP or Mg-TCP), and calcium pyrophosphate dihydrate, $Ca_2P_2O_7 \cdot 2H_2O$ (CPPD), as summarized in table 1.3

Table 1.3 Calcium Phosphates in Biologic Systems

calcium phosphates	occurrence
amorphous calcium phosphates, ACP	soft-tissue calcifications
dicalcium phosphate dihydrate, DCPD	dental calculus, dental caries
octacalcium phosphate, OCP	dental calculus, urinary stone
Mg-substituted tricalcium phosphate, β-TCMP	dental calculus, soft tissue calcifications
carbonate hydroxyapatite, CHA	dental calculus, urinary stone, mineral phases of enamel, dentin, cementum, bone, fish enameloids
carbonate fluorapatite, CFA	fish enameloids
calcium pyrophosphate dihydrate, CPPD	joints

However, while only CHA is present in normal calcified tissues (teeth and bones), several types of CaPs coexist in pathologic calcifications. For example, DCPD, OCP, β-TCMP (or Mg-TCP), and CHA coexist in human dental calculus. Formation of different types of calcium phosphates in both synthetic and biologic systems depends on the solution pH, temperature, and composition. In biologic as well as synthetic systems, calcium phosphates can transform from one form to another depending on the pH and composition of the synthetic solution or biologic microenvironment. For example, ACP, DCPD and OCP can transform to CHA in neutral or basic pH in the presence of HCO_3^- or CO_3^{2-} ions or to β-TCMP in acid, neutral, or basic pH in the presence of Mg^{2+} ions, or (F,OH)-apatites in the presence of F^- ions (LeGeros, 1991).

1.4 HYDROXYAPATITE

Crystals of HA may have either monoclinic or hexagonal unit cells. In the more stable, monoclinic form, rows of phosphate ions are located along the a axis, with calcium and hydroxide ions localized between the phosphate groups (Posner *et al.*, 1958). Calcium ions are placed in two triangles surrounding two hydroxide ions and in larger hexagons surrounding these calcium positions. The hydroxide ions are situated either above or below the calcium ion planes. The rows of hydroxide ions are directed, alternately, upward or downward. The hexagonal form of HA, generally found in biological apatites, has a structure similar to the monoclinic form, but with

columns of calcium and hydroxide groups located in parallel channels (Kay *et al.*, 1964). Ion substitution can readily occur in these channels, and this may account for the high degree of substitution found in natural apatites. In hexagonal HA, the hydroxide ions are more disordered within each row, when compared with the monoclinic form, pointing either upward or downward in the structure. This induces strains that are compensated for by substitution or ion vacancy; hexagonal HA is therefore seldom a stoichiometric phase. As expected from the hexagonal prismatic morphology, atomic force microscopy (AFM) showed that the crystal faces appearing at the atomic level are prism (*a*-face) or basal (*c*-face). A series of steps and step terraces are evident which are thought to have a dislocation origin. Their height (0.8 nm) corresponds to the minimum separation between a-planes. (Onuma *et al.*, 1995). The lattice constant of an apatite crystal in the c-axis direction is thus estimated to be 0.68 nm, and this value closely matches the lattice constant obtained by back-calculation from the CO_3 content. Aging of the precipitates can lead to the incorporation of minor quantities of carbonate. Atmospheric N_2 or CO_2 can induce the incorporation of impurity ions into the apatitic structure (Rodriguez-Lorenzo *et al.*, 2000). HA surface layers are compositionally different from the bulk compositions. Surface layer formation is a consequence of HA being a compound of variable composition: $Ca_{10}(PO_4)_6(OH)_2$ to ~$Ca_9HPO_4(PO_4)_5OH$, existing over Ca/P ratios from 1.67 for stoichiometric to ~1.5 for fully calcium calcium deficient HA. A Ca/P ratio of 1.52 was estimated from the NMR data, suggesting that the surface of nanocrystalline HA with 1 nm surface thickness has nothing in common with the bulk composition (Jäger *et al.*, 2006). One consequence of this compositional variability is that only one HA composition (Ca/P ratio) dissolves congruently (the solution and solid have the same Ca/P ratio) (Johnsson *et al.*, 1992). HA compositions having Ca/P ratios different from the congruently dissolving composition will form surface layers. Equilibration of stoichiometric HA with water will result in the formation of a surface layer having a Ca/P ratio of less than 1.67. In general, for solid HA compositions having Ca/P ratios greater than that of the congruently dissolving composition, a nonstoichiometric surface layer will form and the Ca/P ratio in solution will exceed that of the surface layer. For solid compositions having lower Ca/P ratios than the congruently dissolving composition, the opposite will be true (Brown *et al.*, 1999).

1.4.1 OTHER CALCIUM PHOSPHATES

As a variety of stoichiometric calcium phosphates is known, abbreviations have traditionally been introduced to distinguish between the different compounds. Important parameters are the molar

Ca/P ratio and the solubility. Table 1.4 presents the known calcium phosphate phases (Fernandez *et al.*, 1999; Onuma *et al.*, 1998).

Table 1.4 Properties of the biologically relevant calcium orthophosphates.[a]

Ca/P ratio	Compound	Formula	Solubility at 25 °C -log(K_{sp})	Solubility at 37 °C -log(K_{sp})	pH stability range in aqueous solution at 25°C
0.5	Monocalcium phosphate monohydrate (MCPM)	$Ca(H_2PO_4)_2·H_2O$	1.14	no data	0.0–2.0
0.5	Monocalcium phosphate anhydrate (MCPA)	$Ca(H_2PO_4)_2$	1.14	no data	[d]
1.0	Dicalcium phosphate dihydrate (DCPD, "brushite")	$CaHPO_4·2H_2O$	6.59	6.63	2.0–6.0
1.0	Dicalcium phosphate anhydrate (DCPA, "monetite")	$CaHPO_4$	6.90	7.02	[d]
1.33	Octacalcium phosphate (OCP)	$Ca_8(HPO_4)_2(PO_4)_4·5H_2O$	96.6	95.5	5.5–7.0
1.5	α-tricalcium phosphate (α-TCP)	$α\text{-}Ca_3(PO_4)_2$	25.5	25.5	[b]
1.5	β-tricalcium phosphate (β-TCP)	$β\text{-}Ca_3(PO_4)_2$	28.9	29.5	[b]
1.2–2.2	Amorphous calcium phosphate (ACP)	$Ca_x(PO_4)_y·nH_2O$	[c]	[c]	[c]
1.5–1.67	Calcium-deficient hydroxyapatite (CDHA)	$Ca_{10-x}(HPO_4)_x(PO_4)_{6-x}(OH)_{2-x}$ $(0<x<1)$	≈85.1	≈85.1	6.5–9.5
1.67	Hydroxyapatite (HA)	$Ca_{10}(PO_4)_6(OH)_2$	116.8	117.2	9.5–12
2.0	Tetracalcium phosphate (TTCP)	$Ca_4(PO_4)_2O$	38–44	37–42	[b]

[a] The solubility is given as the logarithm of the ion product of the given formulae (excluding hydrate water) with concentrations in mol L^{-1}. [b] These compounds cannot be precipitated from aqueous solutions. [c] Cannot be measured precisely. However, the following values were reported: 25.7±0.1 (pH 7.40), 29.9±0.1 (pH 6.00), 32.7±0.1 (pH 5.28). [d] Stable at temperatures above 100 °C. [e] Always metastable. The composition of a precipitate depends on the solution pH value and composition.

For the chemically pure compounds, the Ca/P ratio can be between 0.5 ± 2.0. In general, the lower this ratio, the more acidic and soluble in water the calcium phosphate is. A brief description of all calcium orthophosphates is given below.

MCPM (monocalcium phosphate monohydrate, $Ca(H_2PO_4)\cdot 2H_2O$) is the most acidic and water-soluble calcium phosphate compound. It precipitates from highly acidic solutions that are normally used in the industrial production of phosphorus-containing fertilizer ("triple superphosphate") (Becker, 1989).

At temperatures above 100°C, it transforms into MCPA (monocalcium phosphate anhydrate, $Ca(H_2PO_4)_2$). Because of its comparatively high acidity and solubility, MCPM is never found in biological calcifications. However, MCPM is used in some calcium phosphate cements in medicine (Mirtchi *et al.*, 1989; Bermudez *et al.*, 1994; Driessens *et al.*, 1994). Other applications are as antacids, acidulents, and mineral supplements for baking powders, foods, and beverages (Windholz, 1983)

MCPA is the anhydrous form of MCPM. It crystallizes under similar conditions as MCPM but at temperatures above 100 °C (e.g. from highly concentrated mother liquors in fertilizer production). Like MCPM, MCPA never appears in calcified tissues, and there is no current application in medicine; it is mainly used as a fertilizer (Windholz, 1983; Becker, 1989).

DCPD (dicalcium phosphate dihydrate, $CaHPO_4\cdot 2H_2O$; the mineral brushite) can be easily crystallized from aqueous solutions. DCPD transforms into dicalcium phosphate anhydrate at temperatures above 80 °C. DCPD is of biological importance because it is often found in pathological calcifications (dental calculi, crystalluria, chondrocalcinosis, (LeGeros, 1991) and urinary stones (Tracy *et al.*, 1984). DCPD has been proposed as an intermediate in both bone mineralization and dissolution of enamel in acids (dental caries) (LeGeros, 1991). In surgery, DCPD is used in calcium phosphate cements (Driessens *et al.*, 1994; Kurashina *et al.*, 1997; Yamamoto *et al.*, 1998) and, in dentistry, in toothpaste together with fluoride-containing compounds (e.g. NaF) for protection against caries (Crall *et al.*, 1987; Wefel *et al.*, 1987). Other applications are in fertilizers, (Becker, 1989) glass production, calcium supplements in foods, and mineral supplements in cereals (Windholz, 1983). DCPA (dicalcium phosphate anhydrate, $CaHPO_4$; the mineral monetite) is the anhydrous form of DCPD. DCPA, like DCPD, can be crystallized from aqueous solutions but at 100 °C. Unlike DCPD, DCPA occurs in neither normal nor pathological calcifications. It is used in calcium phosphate cements (Takagi *et al.*, 1998), and other applications are as polishing agents, sources of calcium and phosphate in nutritional supplements, tabletting aids, and toothpaste components (Windholz, 1983). OCP (octacalcium phosphate, $Ca_8(HPO_4)_2(PO_4)_4\cdot 5H_2O$) is often found as an intermediate phase during the precipitation of the

thermodynamically more stable calcium phosphates (e.g. HA, calcium-deficient HA (CDHA)) from aqueous solutions. OCP consists of apatitic layers (with atomic arrangements of calcium and phosphate ions similar to those of HA) separated by hydrated layers (water molecules). OCP is of great biological importance because it is one of the stable components of human dental and urinary calculi (Chow *et al.*, 2001). It plays an important role in the in vivo formation of apatitic biominerals. A "central OCP inclusion" (also known as "central dark line") is seen by transmission electron microscopy in many biological apatites and in some synthetically precipitated HA (Iijima *et al.*, 1996; Bodier-Houllé *et al.*, 1998). Although OCP has not been observed in vascular calcifications, it has been strongly suggested as the precursor phase to biological apatites found in natural and prosthetic heart valves (Tomazic *et al.*, 1994; Nancollas *et al.* 2000). β-TCP (β-tricalcium phosphate) is the "true calcium orthophosphate" of the stoichiometric composition $Ca_3(PO_4)_2$. It cannot be precipitated from solution, but may only be prepared by calcination, e.g. of CDHA, at temperatures above 800 °C [Eq. (1)]:

$$Ca_9(HPO_4)(PO_4)_5OH \rightarrow 3Ca_3(PO_4)_2 + H_2O \qquad (1)$$

At temperatures above 1125 °C, it transforms into the high temperature phase β-TCP. Being the stable phase at room temperature, β-TCP is less soluble in water than β-TCP. Pure β-TCP never occurs in biological calcifications. Only the magnesium-containing form called "whitlockite" (chemical formula: β-$(Ca,Mg)_3(PO_4)_2$) is found in dental calculi and urinary stones, (LeGeros, 1991) dental caries, salivary stones, arthritic cartilage, as well as in some soft-tissue deposits (LeGeros, 1991). In biomedicine, β-TCP is used in calcium phosphate bone cements (Mirtchi *et al.*, 1989; Ohura *et al.*, 1996). In combination with HA, β-TCP is used as a "biphasic calcium phosphate" ("BCP") (Daculsi et al., 1999; Alam et al., 2001) as a bone-substitution ceramic. Other applications include fertilizers (Becker, 1989), polishing and dental powders, porcelains, pottery, enamel, and animal food supplements (Windholz, 1983).

α-TCP (α-tricalcium phosphate, α-$Ca_3(PO_4)_2$) is a metastable phase at room temperature, prepared from β-TCP at above 1125 °C. α-TCP is more reactive in aqueous systems than β-TCP and can be hydrolyzed to a mixture of other calcium phosphates. It never occurs in biological calcifications and has a limited application in medicine in calcium phosphate cements (Constantz *et al.*, 1995; Takagi *et al.*, 1998; Bermudez *et al.*, 1994; Takagi *et al.*, 1998; Yamamoto *et al.*, 1998) α-TCP is also used as a fertilizer (Windholz, 1983). ACP (amorphous calcium phosphate) is often encountered as a transient phase during the formation of calcium phosphates in aqueous systems. Usually, ACP is the first phase that is precipitated from a supersaturated solution prepared by rapid mixing of solutions

containing of calcium cations and phosphate anions (Wuthier *et al.*, 1985). The chemical composition of ACP strongly depends on the solution pH value and the concentrations of calcium and phosphate ions in the mother liquor. For example, ACP phases with Ca/P ratios in the range of 1.18:1 (precipitated at solution pH 6.6) to 1.53:1 (precipitated at solution pH 11.7) (Elliott, 1994) and even up to 2.5:1 (LeGeros, 1991) have been described. The structure of ACP is still uncertain. IR spectra of ACP show broad, featureless phosphate absorption bands. The compounds are amorphous, according to X-ray diffraction experiments. Electron microscopy of ACP usually reveals spherical particles with typical diameters of 20 ± 200 nm. However, it is likely that ACP has an apatitic short-range structure, but with a crystal size so small that it appears amorphous in X-ray diffraction experiments (no coherent X-ray scattering). This is supported by X-ray absorption spectroscopic data (EXAFS; extended X-ray absorption fine structure) on biogenic and synthetic samples (Peters *et al.*, 2000; Taylor et al., 1998). On the other hand, it was proposed that the basic structural unit of ACP is a 9.5 Å diameter, roughly spherical cluster of ions with the composition $Ca_9(PO_4)_6$ (Elliott, 1994). These clusters were found experimentally as seed nuclei during the crystallization of HA, and a model was developed to describe the crystallization of HA as a stepwise assembly of these units (Onuma *et al.*, 1998). Biologically, ACP (often containing magnesium, carbonate, and pyrophosphate) is found in soft-tissue pathological calcifications (e.g. heart-valve calcifications of uremic patients) (LeGeros, 1991). In medicine, ACP is sometimes used in calcium phosphate cements (Kurashina *et al.*, 1997). Bioactive composites of ACP with polymers have properties suitable for use in dentistry (Skrtic *et al.*, 2000) and surgery (Schiller *et al.*, 2001; Linhart *et al.*, 2001; Tadic *et al.*, 2002).

1.6 CALCIUM PHOSPHATE PHASE STABILITY

The stability of calcium phosphate (CaP) phases in contact with aqueous solutions can be understood in terms of a typical solubility phase diagram in which solubility isotherms are expressed as plots of (log $T_{ca}T_p$) as a function of pH (Figure 1.5). Here, T_{ca} and T_p are the total molar concentrations of calcium and phosphate, respectively. Figure 1.5 has been constructed on the assumption that the solution contains equal total molar concentrations of calcium and phosphate ions at an ionic strength of 0.1 M. The position of the curves and the singular points in figure 1.5 will change if the ionic strength of the background electrolyte is varied. It can be seen that, at pH above 4.0, HAP (hydroxyapatite) is the most stable phase, followed by TCP and OCP. At pH values lower than 4.0, DCPD is more stable than HA. The variations in solubility with pH imply that a phase exposed to acidic conditions may be covered by a surface coating consisting of a more acidic

calcium phosphate phase (Johnsoon *et al.*, 1992). The apparent solubility behaviour will therefore be quite different from that of the original phase, and the measurement of solution concentrations might lead to unusually large estimated solubilities.

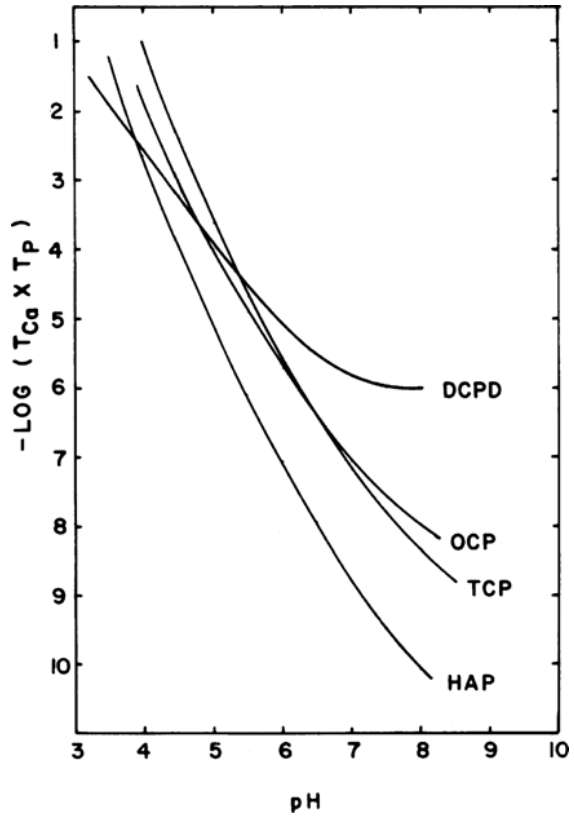

Figure 1.5 Solubility isotherms of calcium phosphate phases at 37°C and I =0.1 M.

Moreover, in determining the likelihood of the formation of preferred crystal phases in solutions supersaturated with respect to several different phases, kinetic factors are also important.

The formation of HA is much slower than that of either OCP or DCPD, and during simultaneous phase formation, a larger portion of the kinetically favoured phase may be observed, even though it has a much smaller thermodynamic driving force.

The balance between kinetic and thermodynamic factors is, therefore, very important in discussing the likelihood of precursor formation during calcium phosphate precipitation. The influence of pH on the formation of calcium phosphates is integrally linked to the properties of phosphate containing solutions (Lynn *et al.*, 2005). Due to the triprotic equilibria in these systems, variations in pH alter the relative concentrations of the four protonated forms of phosphoric acid (Figure 1.6) and thus both the chemical composition and the amount of the CaP that forms by direct precipitation. This complex equilibrium makes the control and prediction of CaP precipitation much more difficult. During the formation of CaP/bioorganic complexes, pH plays a role in determining the properties of both the inorganic and organic phases. While its influence on the inorganic phase

is largely compositional (chemical composition and mass fraction), pH can affect the solubility of bioorganic species during synthesis, a property particularly important for distinguishing between systems in which calcium phosphates and bioorganics are coprecipitated (Kikuchi *et al.*, 2001) and those in which the CaP species is merely precipitated onto an insoluble bioorganic substrate.

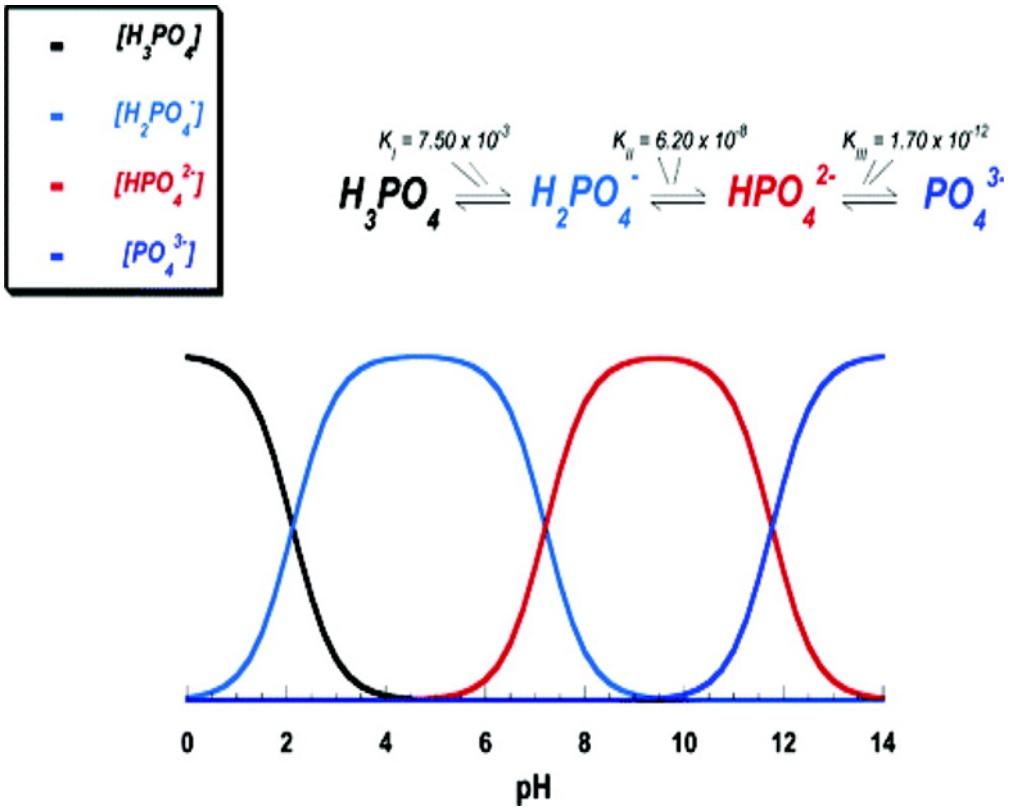

Figure 1.6 pH variation of ionic concentrations in triprotic equilibrium for phosphoric acid solutions. Different pH alters the relative concentrations of the four protonated forms of phosphoric acid and thus both the chemical composition and the amount of calcium phosphate crystals.

1.7 CALCIUM PHOSPHATES AS BIOMATERIALS AND BIOCERAMICS

Biomaterials are synthetic or natural materials used to replace parts of a living system or to function in intimate contact with living tissue (Williams, 1999). They are intended to interface with biological systems to evaluate, treat, augment or replace any tissue, organ or function of the body. Biomaterials are different from biological materials because the former are the materials that are accepted by living tissues and, therefore, might be used for tissue replacements, while the latter are the materials being produced by biological systems (wood, cotton, bones, etc.). In addition, there are biomimetic materials, which are not made by living organisms but have the composition,

structure and properties similar to those of biological materials. Bioceramics might be defined as biomaterials having the ceramic origin.

The use of calcium orthophosphates as biomaterials and bioceramics is based upon their similarity with the mineral phase of bone and teeth. Archaeological findings exhibited in museums showed that materials used to replace missing human teeth have included ox teeth, shells, coral, ivory (elephant tusk), wood, human teeth from corpses, and metals (gold or silver) (Ring, 1985). However, according to the literature, the first attempt to use calcium orthophosphates (it was TCP) as an artificial material to repair surgically created defects in rabbits was performed in 1920 (Albee *et al.*, 1920). Unfortunately, up to now, all attempts to synthesize bone replacement materials for clinical applications featuring physiological tolerance, biocompatibility and long term stability have had only relative success; it comes to show the superiority and complexity of the natural structures (Vallet-Regi *et al.*, 2004).

Generally, the body might treat artificial implants as bioinert, biotolerant, bioactive or bioresorbable materials (Ducheyne, 1987). Bioinert (e.g., zirconia, alumina, carbon and titanium) and biotolerant (e.g., polymethyl methacrylate (PMMA), titanium and Co–Cr alloy) materials will evoke a physiological response to form a fibrous capsule, thus, isolating the material from the body. Calcium orthophosphates (both non-substituted and ion-substituted) fall into the categories of bioactive and bioresorbable materials. A bioactive material will dissolve slightly, but promote the formation of a layer of biological apatite before interfacing directly with the tissue at the atomic level, that result in the formation of a direct chemical bond with bone. Such an implant will provide good stabilization for materials that are subject to mechanical loading. A bioresorbable material will dissolve and allow a newly formed tissue to grow into any surface irregularities but may not necessarily interface directly with the material (Gross *et al.*, 2002; Neo *et al.*, 1992). Bioceramics made of dense HA would be a good example of a bioactive material, while porous scaffolds made of BCP (i.e., β-TCP + HA (Alam *et al.*, 2001; Daculsi, 1998; Daculsi *et al.*, 2003), α-TCP + HA (Langstaff *et al.*, 1999; Sayer *et al.*, 2003; Reid *et al.*, 2005; Pietak *et al.*, 2005) or bone grafts made of CDHA and/or ACP (Tadic *et al.*, 2004) appear to be the examples of bioresorbable materials. Unfortunately, any calcium orthophosphate bioceramics possesses poor mechanical properties that do not allow them to be used in load-bearing areas. Due to this reason, the medical application of calcium orthophosphates is currently focused on the production of non-load-bearing implants, such as pieces for middle ear surgery, filling of bone defects in oral or orthopaedic surgery, as well as coating of dental implants and metallic prosthesis (Vallet-Regi *et al.*, 2004). The mechanical properties of calcium orthophosphate biomaterials and bioceramics were reviewed elsewhere

(Suchanek *et al.*, 1998; Doremus, 1992). In addition, there is a good review on the recent developments in processing and surface modification of HA (Norton *et al.*, 2006).

Biomaterials and bioceramics of calcium orthophosphates are available in various physical forms: particles, blocks (dense or porous), injectable compositions, self-setting cements, coatings on metal implants, composites with polymers, etc. (Legeros *et al.*, 2003). A porous surface provides mechanical fixation in addition to providing sites on the surface that allow chemical bonding between biomaterials and bone. In a porous form, HA ceramics can be colonized by bone tissue (Mastrogiacomo *et al.*, 2006). Therefore, macroporosity (pore size > 100 μm) in solid biomaterials is intentionally introduced by addition of porogens, which are either volatile or soluble substances (e.g., naphthalene, sucrose, $NaHCO_3$, gelatin, PMMA microbeads) (Gross *et al.*, 2002; Takagi *et al.*, 2001; Walsh *et al.*, 2001). Sintering particles, preferably spheres of equal size, is another way to generate porous three-dimensional (3D) bioceramics of calcium orthophosphates. A wetting solution such as polyvinyl alcohol is usually used to aid compaction, which is achieved by cold isostatic pressing the particles into cylinders at approximately 200 MPa (Ota *et al.*, 1997). As hardly any effect of macropore size (150, 260, 510 and 1220 μm) was observed on the in vivo response, there is no need to create bioceramics with very big pores. Microporosity (pore size < 10 μm) results from the sintering process, while dimensions of the pores depend on temperature and sintering time. Creation of the desired porosity is a rather complicated engineering task and the interested readers are referred to special literature (Tadic *et al.*, 2004; Tampieri *et al.*, 2001; Nakahira *et al.*, 2005).

The sintering stage appears to be of great importance to produce bioceramics with the required properties. Several processes occur during sintering of calcium orthophosphates. First, moisture, carbonates and all volatile chemicals remaining from the synthesis stage, such as ammonia, nitrates and any organic compounds, are removed as gaseous products. Second, the removal of these gases facilitates the production of dense materials during sintering. Third, these chemical changes are accompanied by a concurrent increase in crystal size and a decrease in the specific surface area. Fourth, there is the chemical decomposition of all acidic orthophosphates and their transformation into other phosphates.

Studies showed that increasing the specific surface area and pore volume of biomaterials for tissue repair might greatly accelerate the kinetic process of biological apatite deposition and therefore enhance the bone-forming bioactivity. More importantly, precise control over porosity, pore size, and internal pore architecture of biomaterials on different length scales is essential for the understanding of the structure-bioactivity relationship and the rational design of better bone-forming biomaterials (Yan *et al.*, 2004; Izquierdo-Barba *et al.*, 2005).

Calcium orthophosphates have been clinically applied in many areas of dentistry and orthopedics. Bulk material, available in dense and porous forms, is used for alveolar ridge augmentation, immediate tooth replacement and maxillofacial reconstruction (LeGeros, 1991). Further applications include increment of the hearing ossicles, spine fusion and repair of bone defects (Van Blitterswijk *et al.*, 1990). In order to permit growth of new bone into a bone defect, the defect should be filled with a suitable bioresorbable material. Otherwise, ingrowth of fibrous tissue might prevent bone formation within the defect. Today, a large number of different calcium orthophosphate bioceramics for the treatment of bone defects is available on the market. As an example, the readers are referred to a thorough physicochemical characterization of 14 calcium phosphate-based bone substitution materials in comparison to natural bone (Legeros, 2002). The commercial and trade-names of most important types of calcium orthophosphate bioceramics might be found in following references (Legeros, 2002). Chemically, calcium orthophosphate bioceramics is based on HA, β-TCP and/or BCP (i.e., a composite of HA and α- or β-TCP) (LeGeros, 1991; Alam *et al.*, 2001;; Daculsi *et al.*, 2003; Langstaff *et al.*, 1999; Reid *et al.*, 2005; Pietak *et al.*, 2005). General requirements for the ideal bone grafts are as follows: pores of some 100 lm size, a biodegradation rate comparable to the formation of bone tissue (i.e., between a few months and about 2 years) and the sufficient mechanical stability. When compared to α- and b β-TCP, HA is a more stable phase under the physiological conditions, as it has a lower solubility and a slower resorption kinetics (LeGeros, 1991). As implants made of calcined HA are present in bone defects many years after implantation, bioceramics made of β-TCP, α-TCP or BCP (Bohner, 2000; Langstaff *et al.*, 1999; Reid *et al.*, 2005; Pietak *et al.*, 2005; Yin *et al.*, 2006; Daculsi, 1998) is more preferable for medical purposes. According to both observed and measured bone formation parameters, calcium orthophosphates were ranked in order of increasing magnitude as follows: low sintering temperature BCP (rough and smooth) ≈ medium sintering temperature BCP ≈ TCP > calcined low sintering temperature HA > non-calcined low sintering temperature HA > high sintering temperature BCP (rough and smooth) > high sintering temperature HA (calcined and non-calcined) (Bohner, 2000). Figure 1.7 shows an example of the commercially available calcium orthophosphate bone grafts. Another bone healing concept was introduced with hydraulic bone cements based on calcium orthophosphates that harden inside bone defects (Gross *et al.*, 2002; Constantz *et al.*, 1995; Wilson *et al.*, 2006). Two major types of cements are possible. The first one is a dry mixture of two different calcium orthophosphates (a basic one and an acidic one) and the setting reaction occurs according to an acid-base reaction. The second type of calcium orthophosphate cements is when the initial and final calcium orthophosphates have the same Ca/P molar ratio.

Figure 1.7 Examples of calcium orthophosphate-based bone substitution materials

Typical examples are ACP with Ca/P molar ratio within 1.50–1.67 and α-TCP: they form CDHA upon contact with an aqueous solution (Bohmer, 2000). Mixing with an aqueous solution induces chemical interactions that cause the cement setting. Upon mixing, initial calcium orthophosphate(s) are dissolved and precipitated into less soluble calcium orthophosphates. During the precipitation reaction, new crystals grow and become entangled, thus providing a mechanical rigidity to the cement. Setting of these cements occurs mostly within the first 6 h, yielding an 80% conversion to the final products and a compressive strength of 40–60 MPa. The rate of hardening is influenced by a powder to liquid ratio and addition of other chemicals (Constantz *et al.*, 1995; Wilson *et al.*, 2006; Liu *et al.*, 1997; Ambard *et al.*, 2006). Despite a large number of formulations, the calcium orthophosphate cements can only have three different end products: CDHA, DCPD and ACP (Bohmer, 2000).

The first animal study on a hydraulic calcium orthophosphate cement was performed in 1991: the cement consisting of TTCP and DCPA was investigated histologically by implanting disks made of this cement within the heads of nine cats (Costantino *et al.*, 1991). These cements are biocompartible, bioactive and bioresorbable. The structure and composition of the hardened cements is close to that of bone mineral; therefore, the material of these cements can easily be used by bone remodeling cells for reconstruction of damaged parts of bones (Gross *et al.*, 2002;; Bohmer, 2000). The biomechanical evaluation of calcium orthophosphate cements for use in vertebroplasty might be found elsewhere (Hong *et al.*, 2006). Unfortunately, the cements possess a low mechanical strength; this property might be improved by reinforcement with polymers (Lin *et al.*, 2006). A good adaptation to the defect geometry is the major advantage of bone cements, when

compared to implantationof bulk ceramics and scaffolds (Constantz *et al.*, 1995; Suchanek *et al.*, 1998; Fernandez *et al.*, 1999; Bohner, 2000).

Injectable bone substitutes (IBS) made of calcium orthophosphates and an aqueous solution of a hydrophilic biodegradable polymer are also known (Gauthier *et al.*, 2001; Trojani *et al.*, 2006; Iooss *et al.*, 2001; Lerouxel *et al.*, 2006). They look like pastes of high viscosity but possessing enough fluidity to be injected into bone defects by a standard syringe with a needle. Creation of the required level of viscosity to prevent IBS from segregation and phase separation during the shelf life is the major task of the polymer in IBS, while calcium orthophosphates is the building material for bone healing. In terms of application, IBS more or less similar to the aforementioned hydraulic bone cements but, unlike the cements, IBS are available elsewhere (Gauthier *et al.*, 2001; Trojani *et al.*, 2006; Iooss *et al.*, 2001; Lerouxel *et al.*, 2006). Very recently, injectable and macroporous calcium orthophosphate cement scaffold, combining the advantages of IBS and hydraulic bone cements, has been developed (Xu *et al.*, 2006). The future development of both IBS and hydraulic bone cements might be seen in introduction of living cells into their composition (Trojani *et al.*, 2006; Dorozhkin, 2007).

To conclude this part, one should briefly mention on a large variety of bone substituting composites made of calcium orthophosphates and organic compounds (usually, polymers, preferably, biodegradable ones). This approach appeared due to the poor mechanical properties (namely: low elasticity, high brittleness, low tensile strength, low fracture toughness and poor impact resistance) of bone substitutes made of calcium orthophosphates only (Hench, 1991; Hench, 1998). In addition, it is worth reminding that all biologically formed calcified tissues (bones, teeth, antlers, shells, etc.) appear to be very complicated composites of organic and inorganic phases (Legeros, 1991; Weiner *et al.*, 1998). In such composites, the mineral component provides the strength whereas the organic component

contributes to the ductility. This combination of strength and ductility leads to an energy absorption prior to failure. There is a range of suitable calcium orthophosphates (ACP, OCP, α-TCP, β-TCP, CDHA, HA, TTCP and occasionally FA) and an even greater choice of biocompatible polymers those can be divided into two major groups: synthetic polymers (e.g., polyesters, polymethylmethacrylate, poly-e-caprolactone) and polymers of biological origin (e.g., collagen, gelatin, chitosan, alginate, modified starch, cellulose esters). Different ways were realized to bring these two components together into a potential implant, like simple mechanical mixing or co-precipitation. It is also possible to introduce porosity into such composites that is advantageous for most applications as bone substitution material. Such composites might possess the unique properties; for example, there is a recent report on shape memory properties of poly(d,l-lactide)/HA

composites (Zheng *et al.*, 2006). The topic of the composite materials made of calcium orthophosphates and organic/biological compounds was first introduced in 1981 by Prof. Bonfield et al. (Bonfield *et al.*, 1981). Nowadays, the synthesis of organic–inorganic hybrids is a strong and very promising subject of research; therefore, the readers are referred to other reviews (Gross *et al.*, 2002, Wei *et al.*, 2004; Salernitano *et al.*, 2003).

1.8 NANO-CALCIUM PHOSPHATES AS BIOMATERIAL

Calcium phosphate ceramics have been used in orthopaedics for over 30 years because of their excellent biocompatibility (Stupp *et al.*, 1997). Due to the rapid development of nanotechnology, the potential of nano-calcium phosphates has received considerable attention. Here, we discuss recent achievements of nano-calcium phosphate ceramic matrices, which are utilized for bone tissue engineering. Generally, nano-HA has been designed for use in non-loaded parts due to its unsatisfactory mechanical properties. NanOss® bone void filler from Angstrom Medica (Paul *et al.*, 2006) is considered to be the first nanotechnology medical device to receive clearance by the US Food and Drug Administration (FDA) in 2005. It is prepared by precipitating nanoparticles of calcium phosphate in an aqueous phase and the resulting white powder is compressed and heated to form a dense, transparent, and nano-crystalline material. According to the company, NanOss® duplicates the microstructure, composition and performance of human bone and possesses high osteoconductivity.

A new concept in the treatment of bone defects was introduced with bone cements based on calcium phosphates, which have many advantages including their self-setting form, besides excellent biocompatibility and bone-repair properties. (Constantz *et al.*, 1995; Brown *et al.*, 1983). Cement properties, such as setting time, degradation speed, porosity or mechanical behaviour, can be controlled by changing the components of the cement, including type or amount of calcium phosphate and additives (Ginebra *et al.*, 2004). Nano-calcium phosphate has been generally selected as the major component because of its accepted improved sinterability, enhanced densification and better bioactivity than coarser crystals (Han *et al.*, 2004). Through some improvements of cements based on nano-HA in terms of rheological, exothermal and mechanical behaviour etc., some of them are used in clinical treatments, such as Ostim®, an injectable bone matrix in paste form which received CE (Conformite Europeenne) approval in 2002; it is composed of synthetic nanoparticulate hydroxyapatite and can be used in metaphyseal fractures and cysts, acetabulum reconstruction and periprosthetic fractures during hip prosthesis exchange operations, osteotomies, filling cages in spinal column surgery, etc.102 Moreover, cements based on calcium phosphate can be used as

convenient drug carriers for antibiotics, anti-inflammatory drugs, bone morphogenetic proteins (BMP) or transforming growth factors b (TGF-b) (Ginebra *et al.*, 2006). Unlike other carriers for which drugs are usually adsorbed on the surface, the drugs can be incorporated with the cement throughout the whole material volume, by adding them into one of the two cement phases. This fact can facilitate the release of drugs for more prolonged times. This aspect gives great potential to this type of materials for controlled drug delivery in target sites of the skeletal system.

In the bulk form, many different calcium phosphate ceramics are on the market for the treatment of bone defects as a result of orthopaedic removal, bone tumour extraction, complicated fracture etc. (Rueger, 1998). In these cases, the site of the bone defect has to be filled with dense or porous bulk biomaterials, which can offer support for growth of new bone on/in it to avoid growth of fibrous tissue. The materials should be biocompatible, best of all, bioactive and biodegradable. Chemically, synthetic bulk biomaterials are usually based on calcium phosphates. With the rapid development of nanotechnology, nanostructured HA may find use in this field. For example, Cui et al. (Cui *et al.*, 2007; Zhang *et al.*, 2003) developed nano-HA/collagen (NHAC) which mimics the HA nanocrystal-type I collagen nanostructure of natural bone, which can be incorporated into bone metabolism instead of being a permanent implant. Besides, nanocomposites containing HA and chitosan, (Zhang *et al.*, 2002) HA–silver composites, (Shirkhanzadeh *et al.*, 1998) fluorapatite/collagen composites (Yoon *et al.*, 2005) and nanocrystalline yttria-stabilized zirconia reinforced HA (Guo *et al.*, 2003) have been developed for some special functions, for instance antimicrobial activity, improvement of structural stability and cellular responses, enhancement of strength and toughness. Due to process difficulties and the poor mechanical properties of bulk HA, its applications are currently confined to nonload-bearing implants and porous bodies/scaffolds. Porous 3D nanocomposites of HA and collagen/polymer mimic natural bone in composition and microstructure, and can be employed as a matrix for the tissue engineering of bone (Wei *et al.*, 2004).

However, the fracture toughness values of artificial calcium phosphate materials are not as high as those of human cortical bone. Therefore, calcium phosphate materials cannot be used at high-load sites such as femoral and tibial bones. Some biomedical metals like cobalt chromium alloys, titanium and its alloys, and stainless steel 316L etc. are widely used in clinical treatments. But biomedical metals are usually bioinert, and cannot bond to bone directly in vivo. In order to improve biological properties of biomedical metals, nanostructured HA is generally used as a coating material to accelerate bone growth and enhance bone fixation (Ja *et al.*, 1998). Different methods of HA coating commercially utilized are pulsed laser deposition and thermal plasma spraying, which can offer a strong join between the metal matrix and the HA coating (Gua *et al.*,

2003). Other approaches include dip coating, electrophoretic deposition, sol-gel method, etc., which can be used to coat complicated and porous devices along with the incorporation of biologically active substances, for example proteins or antibiotics, into the coating, but with weak bonding force. Because of its advantages over conventional coatings, a biomimetic coating has been suggested (Bigi *et al.*, 2005). The coating is composed of uniform nanocrystalline HA and is demonstrated to be capable of conducting bone formation and promoting direct osseointegration with juxtaposed bone.

1.9 DRUG DELIVERY

Over the past few decades, the rise of modern pharmaceutical technology and the amazing growth of the biotechnology industry have revolutionized the approach to drug delivery systems development (Park, 1997). For most of the industry's existence, pharmaceuticals have primarily consisted of relatively simple, fast-acting chemical compounds that are dispensed orally (as solid pills and liquids) or injected. During the past three decades, however, complex formulations that control the rate and period of drug delivery (i.e., time-release medications) and that target specific areas of the body for treatment have become increasingly common.

Addressing this complexity, coupled with the explosion of new and potential treatments resulting from discoveries of bioactive molecules and gene therapies, pharmaceutical research is facing challenges to, not only the development of new treatments, but also the mechanisms with which to administer them (Breimer, 1999; Juliano; 1990).

A controlled release drug delivery system should be able to achieve the following benefits: (i) maintenance of optimum therapeutic drug concentration in the blood with minimum fluctuation; (ii) predictable and reproducible release rates for extended duration; (iii) enhancement of activity duration for short half-life drugs; (iv) elimination of side effects, frequent dosing and wastage of drug; and (v) optimized therapy and improved patient compliance (Brayden, 2003; Hughes, 2005).

To achieve these benefits, the design of a controlled release system requires simultaneous considerations of several factors, (Koo *et al.*, 2005) such as the chemical and physical properties of the drug,16 the route of administration, (Lin *et al.*, 2006) the nature of the delivery vehicle, the mechanism of drug release, the potential for targeting,20 and biocompatibility. Due to the extensive interdependency of those factors, it is not easy to establish a sequential process for designing a controlled drug delivery system (Lecomte *et al.*, 2005).

Drug delivery technology can bring both therapeutic and commercial value to health care products (Acharya *et al.*, 2006). Large pharmaceutical companies are looking to extend the lifetimes of their

patents by forging strategic alliances with usually smaller drug delivery technology companies aimed at presenting old drugs in new proprietary forms. Most drug delivery products reach the market as a result of joint ventures between drug delivery companies and pharmaceutical companies. For this reason, drug delivery technology companies enjoy a good return on their investments in the form of increased revenues and market share and it is a very fast growing segment of the economy. (Brayden, 2003; Hughes, 2005). However, the design and development of drug delivery systems involves many different sciences that underpin the research. It is clear that significant advances will only be made through multidisciplinary teams that utilize the latest advances in the biological, chemical, physical, and engineering sciences. The underpinning sciences are also vital to the process of developing successful products. There are three key and interrelated areas of research. (i) Achieve a greater understanding of the biological fate and the targeting of drugs, particularly biopharmaceuticals, macromolecules, and macromolecular delivery systems at the molecular, membrane, and cellular level. (ii) Provide a greater understanding of the physicochemical properties of biopharmaceuticals, macromolecules, and macromolecular delivery systems and how these are modified within a biological environment affecting their activity. (iii) Promote the development of novel materials and delivery systems that will overcome these biological barriers.

Drug delivery technologies are classified according to the route through which a drug is administered into the body. In the oral route, a drug is taken by mouth into the gastrointestinal (GI) tract to be absorbed. Other important routes include intravenous injection, intramuscular injection, subcutaneous injection, pulmonary, ocular, buccal (through the internal wall of the cheeks), sublingual (under the tongue), nasal, vaginal, rectal, transdermal, and implanted (inside a body cavity). Drug delivery research focuses on how a drug is delivered into the body without much consideration of the fate and effects of the drug in the body. Those aspects are normally the domain of studies in pharmacokinetics, although obviously, these aspects are closely linked to the delivery route. Highly sophisticated drug delivery systems are being developed to exert their effects after they are administered into the body, in particular, into the systemic circulation. They usually consist of particles in the size range of nanometers that have unique combinations of capacities such as controlled release and biological site-specific targeting. This new group of delivery systems is definitely an important component of modern drug delivery technology. A myriad of novel drug delivery technologies are under development and significant advances are being made in nearly all branches of drug delivery.

One of the most interesting is the implantable drug delivery systems (IDDS). These techniques have the advantage of maintaining a steady release of drug to the specific site of action so that they are

safer and more reliable. IDDS can be classified into three major categories: biodegradable or nonbiodegradable implants, implantable pump systems, and the newest atypical class of implants (Szymura-Oleksiak *et al.*, 2001). Biodegradable and nonbiodegradable implants are available as monolithic systems or reservoir systems. The release kinetics of drugs from such systems depend on both the solubility and diffusion coefficient of the drug in the polymer, the drug load, as well as the in vivo degradation rate of the polymer in the case of the biodegradable systems (Dash *et al.*, 1998). Controlled release of drugs from an implantable pump is generally achieved utilizing the microtechnology of electronic systems and remote-controlled flow rate manipulation through the maintenance of a constant pressure difference. The third IDDS system, the atypical class, includes recently developed systems such as ceramic hydroxyapatite antibiotic systems used in the treatment of bone infections, intraocular implants for the treatment of glaucoma, and transurethral implants utilized in the treatment of impotence. The major advantages of these systems include targeted local delivery of drugs at a constant rate, less drug required to treat the disease state, minimization of possible side effects, and enhanced efficacy of treatment. Also, these forms of delivery systems are capable of protecting drugs which are unstable in vivo and that would normally require frequent dosing intervals. Due to the development of such sustained release formulations, it is now possible to administer unstable drugs once a week to once a year that in the past required frequent daily dosing.

Preliminary studies using these systems have shown superior effectiveness over conventional methods of treatment.54 However, one limitation of these newly developed drug delivery systems is the fact that their cost-to-benefit ratio is high which restricts their use over conventional dosage forms. Hopefully, in the future, new implantable systems can be developed at a lower cost, enhancing their use in standard therapeutic practice. Some of the most recently discovered implants are in the early developmental stages and more rigorous clinical testing is required prior to their use in standard practice (Dash *et al.*, 1998).

1.10 HYDROXYAPATITE AS DRUG DELIVERY MATRIX

Synthetic hydroxyapatite exhibits good properties as a biomaterial, such as biocompatibility, bioactivity, osteoconductivity, direct bonding to bone, etc., exciting the applications of HA in the fields of bone tissue engineering and orthopaedic therapies (Roveri *et al.*, 2008). There are many synthetic strategies to produce HA and substituted HA, including wet producing, hydrothermal, electrochemical and ultrasonic mobilisation methods, sol-gel and solid-state synthesis.

Apatites with different stoichiometry and morphology have been prepared and the effects of varying powder synthesis conditions on stoichiometry, crystallinity and morphology, have been analysed. The effects of varying the concentration of the reagents, the reaction temperature and time, initial pH, ageing time and the atmosphere within the reaction vessel have also been studied (Koutsopoulos, 2002). In order to optimise its specific biomedical applications, especially drug delivery function, the physical–chemical features that should be tailored in synthetic biomimetic HA are dimensions, porosity, morphology and surface properties (Roveri *et al.*, 2008).

For the last 30 years calcium phosphate ceramics have been, and still are today, very popular implant materials for diverse clinical applications. Porous HA simulating spongy bone morphology (porosity varying from a microporosity > 1 μm to a macroporosity ranging from 300 to 2000 μm) has been prepared using various technologies to control pore dimension, shape, distribution and interconnections. HA ceramics processed by high-temperature treatment (Rodriguez-Lorenzo *et al.*, 2001) present a significant reduction of bioreactivity and growth kinetics of new bone due to the lack of resorbability. New formation methods at lower temperatures have been developed, allowing one to obtain porous bioceramics with a low degree of crystallinity. Colloidal processing (Tadic *et al.*, 2004), starch consolidation, gel casting and foam out (Padilla *et al.*, 2002) have yielded excellent results, producing bioceramics with a bimodal distribution of the pore size that can be modified as a function of the sintering conditions. Different types of CaP-ceramics are available, although they can be classified as either hydroxyapatite (HA), beta-tricalcium phosphate (β-TCP), biphasic calcium phosphate (BCP), amorphous calcium phosphate (ACP), carbonated apatite (CA) or calcium deficient HA (CDHA) (Habraken *et al.*, 2007). The use of these materials for tissue engineering purposes is still being explored. Most researchers are aware that the low resorbability of sintered CaP-ceramics, and in particular the incomplete resorbability of ceramic HA, appear useful when a biomaterial has to be implanted with a defined 3D form. The use of highly porous implants induces bone formation inside the implant and increases degradation, but the complete resorption in most cases is very difficult, due to the crystalline architecture.

Porous coralline HA can be synthesised by a hydrothermal method for HA formation directly from natural sea corals (Roy *et al.*, 1974) and HA replaces aragonite whilst preserving its porous structure. The biaxial strength of coralline apatite could be improved with a unique double treatment that includes a nano-coating layer to cover meso- and nano-pores. In this two-stage process, the coral is fully converted into hydroxyapatite and then coated with a sol-gel-derived apatite. This new material can be applied to bone graft applications where high strength requirements and longevity are pertinent (Ben-Nissan, 2003).

The interconnected network of pores promotes bone in-growth, but also allows bioceramics to be utilised as drug delivery agents by inserting different bioactive molecules. Many studies have demonstrated that hydroxyapatite ceramics can be used to deliver steroids, antibiotics, proteins, hormones and anticancer drugs. Porous ceramics closely mimicking spongy bone morphology have been synthesised by the impregnation of cellulosic sponges with poorly crystalline HA water suspension (Ma, 2008). These porous ceramics have been tested as controlled drug delivery bone grafts to evaluate the fundamental parameters that control release kinetics. A theoretical approach, based on the use of the Finite Element Method, was adopted to describe the ibuprofen–lysine and hydrocortisone Na-succinate release kinetics, comparing numerical results with experimental results (Palazzo *et al.*, 2005). An alternative approach to tissue engineering, which uses cells seeded onto macropores of these HA scaffolds to promote bone growth, is represented by filling the macro- and micro-pores with gelatine, which can act as a cell nutrient and/or delivery agent of bioactive molecules. When powder bioceramics are used for bone filling applications, they are usually mixed with a polymeric carrier matrix to avoid migration out of the implant region. Both non-absorbable (poly(methyl methacrylate) (Pena *et al.*, 1997) , polyethylene (Wang *et al.*, 1996) and polysulfone) and biodegradable (poly(lactic acid) (Kikuchi *et al.*, 1998), polyglycolic acid, collagen, cellulose and starch (Bakos *et al.*, 1999; Cherng *et al.*, 1997) polymeric matrices can be used, even if the non-biodegradability drastically reduces the HA crystal bioactivity. The chemical and biological properties of the latter are strictly linked to their dimensions, the regulation of which requires a high level of biological and chemical control at the nano-scale. Thus, the recent trend in biomaterials research is focused on overcoming the limitations of calcium phosphates, or more precisely hydroxyapatite ceramics, and in improving their biological properties via exploring the unique advantages of nanotechnology (Kalita *et al.*, 2007). The trend is shifting towards nanotechnology to improve the biological responses of HA, because nano-HA is a constituent of bone, improving the biomaterial–bone interface. Nanostructured biomimetic materials offer much higher performances than their larger particle sized counterparts, due to their large surface to volume ratio and unusual chemical/electronic synergistic effects. The surface functionalisation of HA nano-crystals with bioactive molecules makes them able to transfer information to and to act selectively on the biological environment, and this represents a main challenge for innovative bone substitute materials. In this way HA nanocrystals will not only guarantee, for instance, either osteo-integration or osteo-induction enhanced properties, but they will also perform at the molecular level by stimulating specific cellular responses. Hydroxyapatite is also known for its binding capability to a wide variety of molecules. It is an attractive goal to develop new biomimetic apatite nanocrystals for potential use in bone implantation, which in addition function as a local targeted delivery system

for anticancer and antimetastatic drugs with controlled release properties. For example, the application of such a material in the chemotherapeutic treatments of osteosarcoma could result in tumour inhibition accompanied by low levels of systemic toxicity.

REFERENCES

- Acharya, G.; Park, K. *Adv. Drug Del. Rev.* **2006**, *58*, 387.
- Alam, I.; Asahina, I.; Ohmamiuda, K.; Enomoto, S. *J. Biomed. Mater. Res.* **2001**, *54*, 129.
- Alam, I.; Asahina, I.; Ohmamiuda, K.; Enomoto, S.*J. Biomed. Mater. Res.* **2001**, *54*, 129.
- Albee, F. H.; Morrison, H. F. *Ann. Surg.* **1920**, *71*, 32
- Ambard, A. J.; Mueninghoff, L. *J. Prosthodontics* **2006**, *15*,321.
- Bakos, D.; Soldan, M.; Hernandez-Fuentes, I. *Biomaterials* **1999**, 20, 191.
- Becker, P. In *Fertilizer Science and Technology Series*, Marcel Dekker, New York, 1989, pp. 6.
- Beevers, C. A.; McIntyre, D. B. *Miner. Mater*. **1956**, *27*, 254.
- Ben-Nissan B. *Curr. Opin. Solid State Mater. Sci.* **2003**, *7*, 283.
- Bermudez, O.; Boltong, M. G.; Driessens, F. C. M.; Planell, J. A. *J. Mater. Sci. Mater. Med.* **1994**, *5*, 67.
- Bigi, A.; Boanini, E.; Bracci, B.; Facchini, A.; Panzavolta, S.; Segatti, F.; Sturba, L. *Biomaterials* **2005**, *26*, 4085.
- Bodier-Houllé, P. S.; Voegel, P. J. C.; Cuisinier, F. J. G. *Acta Crystallogr. Sect. D* **1998**, *54*, 1377.
- Bohner, M. *Injury* **2000**, *31(Suppl. 4)*, D37.
- Bonfield, W.; Grynpas, M. D.; Tully, A. E.; Bowman, J.; Abram, J. *Biomaterials* **1981**, *2*, 185.
- Boskey, A. L.; Paschalis, E. In *Bone Engineering*; Davies, J. E., Ed.; em squared, Inc.: Toronto, 2000; p 44.
- Boyde, A. In *Handbook of Microscopic Anatomy*; Oksche, A. L. V., Eds.; Springer-Verlag: Berlin, 1989.
- Brayden, D. J. *Drug Discovery Today* **2003**, *8*, 976.
- Breimer, D. D. *J. Controlled Release* **1999**, *62*, 3.
- Brown, P. W.; Martin, R. I. *J. Phys. Chem. B* **1999**, *103*, 1671.
- Brown, W. E.; Chow, L. C. *J. Dent. Res.* **1983**, *62*, 672.

- Burger, C.; Zhou, H.; Wang, H.; Sics, I.; Hsiao, B. S.; Chu, B.; Graham, L.; Glimcher, M. *Biophys. J.* **2008**, *95*, 1985.
- Cherng A.; Takagi, S.; Chow, L. C. J. *Biomed. Mater. Res.* **1997**, 35, 273.
- Chow, L. C.; Eanes E. D. *Octacalcium Phosphate*, Karger: Basel, 2001; Vol. 18.
- Constantz, B. R.; Ison, I. C.; Fulmer, M. T.; Poser, R. D.; Smith, S. T.; VanWagoner, M.; Ross, J.; Goldstein, S. A.; Jupiter, J. B.; Rosenthal, D. I. *Science* **1995**, *267*, 1796.
- Costantino, P. D.; Friedman, C. D.; Jones, K.; Chow, L. C.; Pelzer, H. J.; Sisson, G. A. *Arch. Otolaryngol. Head Neck. Surg.* **1991**, *117*, 379.
- Cowles, E. A.; DeRome, M. E.; Pastizzo, G.; Brailey, L. L.; Gronowicz, G. A. *Calcif. Tissues Int.* **1998**, *62*, 74.
- Crall, J. J.; Bjerga, J.M. *J. Oral Pathol.* **1987**, *16*, 488.
- Cui, F. Z.; Li, Y.; Ge, J. *Mater. Sci. Eng., R* **2007**, *5*, 1.
- Daculsi, G. *Biomaterials* **1998**, *19*, 1473.
- Daculsi, G., Laboux, O.; Malard, O.; Weiss, P. *J. Mater. Sci. Mat. Med.* **2003**, *14*, 195.
- Daculsi, G.; Bouler, J. M.; LeGeros, R. Z. *Int. Rev. Cytol.* **1997**, *172*, 129.
- Daculsi, G.; Weiss, P.; Bouler, J. M.; Gauthier, O.; Millot, F.; Aguado, E. *Bone* **1999**, *25* (Suppl. 2), 59S.
- Dash, A. K.; Cudworth, G. C. *Pharmacol. Toxicol. Meth.* **1998**, *40*, 1.
- DeJong, W. F. *Res. Trav. Chim.* **1926**, *45*, p.445.
- Doremus, R. H. *J. Mater. Sci.* **1992**, *27*, 285
- Dorozhkin S. V. *J. Mater. Sci.* **2007**, *42*,1061.
- Dorozhkin, S. V.; Epple, M. *Angew. Chem., Int. Ed.* **2002**, *41*, 3130.
- Driessens, F. C. M.; Boltong, M. G.; Bermudez, O.; Planell, J. A.; Ginebra, M. P.; Fernandez, E. *J. Mater. Sci. Mater. Med.* **1994**, *5*, 164.
- Ducheyne, P *J. Biomed. Mater. Res.* **1987**, *21*, 219.
- Ellliott, J. C. *Structure and Chemistry of Apatites and other Calcium Orthophosphates*; Elsevier: The Netherlands, 1994.
- Feng, J. Q.; Ward, L. M.; Liu, S.; Lu, Y.; Xie, Y.; Yuan, B.; Yu, X. *Nat. Genet.* **2006**, *38*, 1311.
- Fernandez, E; Gil, F. J.; Ginebra, M. P.; Driessens, F. C. M.; Planell, J. A.; Best, S. M. *J. Mater. Sci. Mater. Med.* **1999**, *10*, 169.
- Fernandez-Moran, H.; Engstrom, A. *Biochim. Biophys. Acta* **1957**, *23*, 260.
- Garant, P. *Oral Cells and Tissues*; Quintessence Publishing Co. Inc.: Chicago, 2003.

- Gauthier, O.; Goyenvalle, E.; Bouler, J. M.; Guicheux, J.; Pilet, P.; Weiss, P.; Daculsi, G. *J. Mat. Sci. Mater. Med.* **2001**, *12*, 385.
- Ginebra, M. P.; Driessens, F. C. M.; Planell, J. A. *Biomaterials* **2004**, *25*, 3453.
- Ginebra, M. P.; Traykova, T.; Planell, J. A. *J. Controlled Release* **2006**, *113*, 102.
- Gross, K. A.; Berndt, C. C. (2002) In: Hughes J. M.; Kohn M.; Rakovan J. (eds) *Phosphates: geochemical, geobiological and materials importance.* Series: Reviews in mineralogy and geochemistry, vol 48. Mineralogical Society of America,Washington, DC, 2002
- Gua, Y. W.; Khor, K. A.; Cheang, P. *Biomaterials* **2003**, *23*, 1603.
- Guo, H.; Khor, K. A.; Boey, Y. C.; Miao, X. *Biomaterials* **2003**, *24*, 667.
- Habraken, W. J. E. M.; Wolke, J. G. C.; Jansen, J. A. *Adv. Drug Del. Rev.* **2007**, *59*, 234.
- Han, Y.; Li, Sh.; Wang, X.; Chen, X. *Mater. Res. Bull.*, **2004**, *39*, 25.
- Hench, L. L. *J. Am. Ceram. Soc.* **1991**, *74*, 1487.
- Hench, L. L. *J. Am. Ceram. Soc.* **1998**, *81*, 1705.
- Hong, S. J.; Park, Y. K.; Kim, J. H.; Lee, S. H.; Ryu, K. N.; Park, C. M.; Kim, Y. S. *J. Neurosurgery Spine* **2006**, *4*, 154.
- Hughes, G. A. *Nanomedicine* **2005**, *1*, 22.
- Hughes, G. A. *Nanomedicine* **2005**, *1*, 22.
- Iijima, M.; Nelson, D. G. A.; Pan, Y.; Kreinbrink, A. T.; Adachi, M.; Goto, T.; Moriwaki, Y. *Calcif. Tissue Int.* **1996**, *59*, 377.
- Imbeni, V.; Kruzic, J. J.; Marshall, G. W.; Marshall, S. J.; Ritchie, R. O. *Nat. Mater.* **2005**, *4*, 229.
- Iooss, P., LeRay, A. M.; Grimandi, G.; Daculsi, G.; Merle, C. *Biomaterials* **2001**, *22*, 2785.
- Izquierdo-Barba, I.; Ruiz-Gonzalez, L.; Doadrio, J. C.; Gonzalez-Calbet, J. M.; Vallet-Regì, M. *Solid. State Sci.* **2005**, *7*, 983
- Ja, C.; Klein, C. P.; Vriesde, R. C.; Rozing, P. M.; de Groot, K. *J. Biomed. Mater. Res.* **1998**, 40, 341.
- Jäger, C.; Welzel, T.; Meyer-Zaika, W.; Epple, M. *Magn. Reson. Chem.* **2006**, *44*, 573.
- Johnsson, M. S. A.; Nancollas, G. H. *Crit. Rev. Oral Biol. Med.* **1992**, *3*, 61.
- Juliano, R. L. *Controlled delivery of drugs: and overview and prospectus*; Oxford University Press: New York, 1990.
- Kalita, S. J.; Bhardwaj, A.; Bhatt, H. A. *Mater. Sci. Eng. C* **2007**, 27, 441.
- Kay, M.; Young, R. A.; Posner, A. S. *Nature* **1964**, *204*, 1050

- Kikuchi, M.; Itoh, S.; Ichinose, S.; Shinomiya, K.; Tanaka, J. *Biomaterials* **2001**, *22*, 1705.
- Kikuchi, M.; Sato, K.; Suetsugu, Y.; Tanaka, J. Bioceramics. New York: World Scientific; 1998
- Kodaka, T.; Nakajima, F.; Higashi, S. *Caries Res.* **1989**, *23*, 290.
- Koo, O.; Rubinstein, I.; Onyuksel, H. *Nanomedicine* **2005**, *1*, 77.
- Koutsopoulos S. *J. Biomed. Mater. Res.* **2002**, *62*, 600.
- Kurashina, K.; Kurita, H.; Hirano, M.; Kotani, A.; Klein, C. P.; de Groot, K. *Biomaterials* **1997**, *18*, 539.
- Langstaff, S. D.; Sayer, M.; Smith, T. J. N.; Pugh, S. M. *Biomaterials* **2001**, *22*, 135.
- Langstaff, S. D.; Sayer, M.; Smith, T. J. N; Pugh, S. M.; Hesp, S. A. M; Thompson, W. T. *Biomaterials* **1999**, *20*, 1727.
- Lecomte, F.; Siepmann, J.; Walther, M.; MacRae, R. J.; Bodmeier, R. *Pharm. Res.* **2005**, *22*, 1129.
- Legeros R. *Z. Clin. Orthop. Rel. Res.* **2002**, *395*, 81.
- LeGeros, R. *Z. Calcium Phosphates in Oral Biology and Medicine. Monographs in Oral Sciences*; Myers, H., Ed.; Karger: Basel, 1991; Vol. 15.
- LeGeros, R. *Z. Prog. Cryst. Growth Charact.* **1981**, *4*, 1.
- Legeros, R. Z.; Legeros, J. P. *Key Engin. Mater.* **2003**, *240–242*, 3.
- LeGeros, R. Z.; LeGeros, J. P.; Trautz, O. R.; Klein, E. *Dev. Appl. Spectrosc.* **1970**, *7B*, 3.
- LeGeros, R. Z.; LeGeros, J. P.; Trautz, O. R.; Shirra, W. P. *Adv. X-ray Anal.* **1971**, *14*, 57.
- LeGeros, R. Z.; Silverstone, L. M.; Daculsi, G.; Kerebel, L. M. *J. Dent. Res.* **1983**, *62*, 138.
- LeGeros, R. Z.; Trautz, O. R.; LeGeros, J. P. *Science* **1967**, *155*, 1409.
- Lerouxel, E.; Weiss, P.; Giumelli, B.; Moreau, A.; Pilet, P.; Guicheux, J.; Corre, P.; Bouler, J. M.; Daculsi, G.; Malard, O. *Biomaterials* **2006**, *27*, 4566.
- Lin, C. C.; Metters, A. T. *Adv. Drug Del. Rev.* **2006**, *58*, 1379.
- Lin, J.; Zhang, S., Chen, T.; Liu, C.; Lin, S.; Tian, X. *J. Biomed. Mater. Res. B* **2006**, *76*, 432.
- Linhart, W.; Peters, F.; Lehmann, W.; Schilling, A. F.; Schwarz, K.; Amling, M.; Rueger, J. M.; Epple, M. *J. Biomed. Mater. Res.* **2001**, *54*, 162.
- Liu, C.; Shen, W.; Gu, Y.; Hu, L. *J. Biomed. Mater. Res.* **1997**, 35, 75
- Lynn, A. K.; Bonfield, W. *Acc. Chem. Res.* **2005**, *38*, 202.
- Ma, X. P. *Adv. Drug. Del. Rev.* **2008**, *60*, 184.

- Mann, S. *Biomineralization Principles and Concepts in Bioinorganic Materials Chemistry*; Oxford University Press: Oxford, United Kingdom, 2001.
- Manolagas, S. C. *Endocr. Rev.* **2000**, *21*, 115.
- Marks, S. C.; Hermey, D. C. In *The Principles of Bone Biology*; Bilezikian, J. P., Raisz, L. G., Rodan, G. A., Eds.; Academic Press: New York, 1996; p 3.
- Mastrogiacomo, M.; Scaglione, S.; Martinetti, R.; Dolcini, L.; Beltrame, F.; Cancedda, R.; Quarto R. *Biomaterials* **2006**, *27*, 3230.
- McConnell, D. *J. Dent. Res.* **1952**, *31*, 53.
- Mirtchi, A. A.; Lemaitre, J.; Terao, N. *Biomaterials* **1989**, *10*, 475.
- Moreno, E. C.; Kresak, M.; Zahradnik, R. T. *Caries Res (Suppl. 1)* **1977**, *11*, 142.
- Nakahira, A.; Murakami, T.; Onoki, T.; Hashida, T.; Hosoi, K. *J. Am. Ceram. Soc.* **2005**, *88*, 1334.
- Nancollas, G. H.; Wu, W. *J. Crystal Growth* **2000**, *211*, 137.
- Neo, M.; Kotani, S.; Fujita, Y.; Nakamura, T.; Yamamuro, T.; Bando, Y.; Ohtsuki, C.; Kokubo, T. *J. Biomed. Mater. Res.* **1992**, *26*, 255.
- Norton, J.; Malik, K. R.; Darr, J. A.; Rehman, I. *Adv. Appl. Ceram.* **2006**, *105*, 113.
- Ohura, K.; Bohner, M.; Hardouin, P.; Lemaitre, J.; Pasquier, G.; Flautu, B. *J. Biomed. Mater. Res.* **1996**, *30*, 193.
- Olszta, M. J.; Cheng, X. G.; Jee, S. S.; Kumar, R.; Kim, Y. Y.; Kaufman, M. J.; Douglas, E. P.; Gower, L. B. *Mater. Sci. Eng., R* **2007**, *58*, 77.
- Onuma, K.; Ito, A. *Chem. Mater.* **1998**, *10*, 3346.
- Onuma, K.; Ito, A.; Tateishi, T.; Kameyama, T. *J. Cryst. Growth* **1995**, *148*, 201.
- Ota, Y.; Kasuga, T.; Abe, Y. *J. Am. Ceram. Soc.* **1997**, *80*, 225.
- Padilla S.; Roman J.; Vallet-Regi M. *J. Mater. Sci. Mater. Med.* **2002**, *13*, 1193.
- Paine, M. L.; White, S. N.; Luo, W.; Fong, H.; Sarikaya, M.; Snead, M. L. *Matrix Biol.* **2001**, *20*, 273.
- Palazzo, B.; Roveri, N.; Sidoti, M. C.; Tampieri, A.; Sandri, M.; Bertolazzi, L.; Galbusera, F.; Dubini, G.; Vena, P.; Contro, R. *Mater. Sci. Eng. C* **2005**, *25*, 207.
- Park, K. *Controlled Drug Delivery: Challenges and Strategies*; American Chemical Society: Washington, DC, 1997.
- Paul, W.; Sharma, C. P. *Am. J. Biochem. Biotechnol.* **2006**, *2*, 41.
- Pena, J.; Vallet-Regi M.; San Roman J. *J. Biomed. Mater. Res.* **1997** ; *35* : 129 -34
- Peters, F.; Schwarz, K.; Epple, M. *Thermochim. Acta* **2000**, *361*, 131.

- Pietak, A. M.; Reid, J. W.; Sayer, M. *Biomaterials* **2005**, *26*, 3819.
- Posner, A. S.; Perloff, A.; Diorio, A. F. *Acta Crystallogr.* **1958**, *11*, 308.
- Reddi, A. H. *J. Cell. Biochem.* **1994**, *56*, 192.
- Reid, J. W.; Pietak, A. M.; Sayer, M.; Dunfield, D.; Smith, T. J. N. *Biomaterials* **2005**, *26*, 2887.
- Rey, C.; Renugoplakrishan, V.; Collins, B. *Calcif. Tissue Int.* **1991**, *49*, 251.
- Rho, J. Y.; Kuhn-Spearing, L.; Zioupos, P. *Medi. Eng. Phys.* **1998**, *20*, 92.
- Ring, M. E. *Dentistry: an illustrated history.* Abradale Press, New York, 1985, pp 15–36.
- Robinson, C.; Kirkham, J.; Shore, R. Eds. *Dental Enamel Formation to Destruction*; CRC Press: Boca Raton, FL, 1995.
- Rodriguez-Lorenzo, L. M.; Vallet-Regi, M. *Chem. Mater.* **2000**, *12*, 2460.
- Rodriguez-Lorenzo, L. M.; Vallet-Regi, M.; Ferreira, J. M. F.; *Biomaterials* **2001**, *22*, 583.
- Roveri, N.; Palazzo, B.; Iafisco M. *Expert Opin. Drug Deliv.* **2008**, *5*, 861.
- Roy, D. M.; Linnehan, S. K. *Nature* **1974**, *247*, 220.
- Rueger, J. M. *Orthopade* **1998**, *27*, 72.
- Salernitano, E.; Migliaresi, C. *J. Appl. Biomater. Biomech.* **2003**, *1*, 3.
- Sayer, M.; Stratilatov, A. D.; Reid, J. W.; Calderin, L.; Stott, M. J.; Yin, X.; MacKenzie, M.; Smith, T. J. N.; Hendry, J. A.; Langstaff, S. D. *Biomaterials* **2003**, *24*, 369.
- Schiller, C.; Siedler, M.; Peters, F; Epple, M. *Ceram. Trans.* **2001**, *114*, 97.
- Schmidt, W. *J. Naturwissenschaften* **1936**, *24*, 361.
- Shirkhanzadeh, M.; Azadegan, M. *J. Mater. Sci.: Mater. Med.* **1998**, *9*, 385.
- Skrtic, D.; Antonucci, J. M.; Eanes, E. D.; Eichmiller, F. C.; Schumacher, G. E. *J. Biomed. Mater. Res.* **2000**, *53*, 381.
- Stupp, S. I.; Braun, P. V. *Science* **1997**, *277*, 1242.
- Suchanek, W.; Yoshimura, M. *J. Mater. Res.* **1998**, *13*, 94.
- Szymura-Oleksiak, J.; Slosarczyk, A.; Cios, A.; Mycek, B.; Paszkiewicz, Z.; Szklarczyk, S.; Stankiewicz, D. *Ceram. Int.* **2001**, *27*, 767.
- Tadic, D. Peters, F.; Epple, M. *Biomaterials* **2002**, *23*, 2553.
- Tadic, D.; Beckmann, F.; Schwarz, K.; Epple, M. *Biomaterials* **2004**, *25*, 3335
- Tadic, D.; Beckmann, F.; Schwarz, K.; Epple, M. *Biomaterials* **2004**, *25*, 3335.
- Takagi, S.; Chow, L. C. *J. Biomed. Mater. Res.* **2001**, *12*, 135.
- Takagi, S.; Chow, L. C.; Ishikawa, K. *Biomaterials* **1998**, *19*, 1593.
- Tamerler, C.; Sarikaya, M. *MRS Bull.* **2008**, *33*, 504.

- Tampieri, A.; Celotti, G.; Sprio, S.; Delcogliano, A.; Franzese, S. *Biomaterials* **2001**, *22*, 1365.
- Taylor, M. G.; Simkiss, K.; Simmons, J.; Wu, L. N. Y.; Wuthier, R. E. *Cell. Mol. Life Sci.* **1998**, *54*, 192.
- Ten Cate, A. R. *Oral Histology. Development, Structure, and Function*, 4th ed.; Mosby: St. Louis, MO, 1994.
- Termine, J. D.; Kleinman, H. K.; Whitson, S. W.; Conn, K. M.; McGarvey, M. L.; Martin, G. R. *Cell* **1981**, *26*, 99.
- Tomazic, B. B.; Brown, W. E.; Shoen, F. J. *J. Biomed. Mater. Res.* **1994**, *28*, 35.
- Tracy B. M.; Doremus, R. H. *J. Biomed. Mater. Res.* **1984**, *18*, 719.
- Traub, W.; Arad, T.; Weiner, S. *Proc. Natl. Acad. Sci. U.S.A.* **1989**, *86*, 9822.
- Trojani, C.; Boukhechba, F.; Scimeca, J. C.; Vandenbos, F.; Michiels, J. F.; Daculsi, G.; Boileau, P.; Weiss, P.; Carle, G. F.; Rochet, N. *Biomaterials* **2006**, *27*, 3256.
- Urist, M. R. *Science* **1965**, *150*, 93.
- Urist, M.; Silverman, B. F.; Buring, K.; Dubuc, F. L.; Rosenberg, J. *J. Clin. Orthop.* **1967**, *53*, 243.
- Vallet-Regi, M.; Gonzalez-Calbet, J. M. *Progress Solid State Chem.* **2004**, *32*, 1.
- van Blitterswijk, C. A.; Hesseling, S. C.; Grote, J. J.; Koerten, H. K.; de Groot, K. *J. Biomed. Mater. Res.* **1990**, *24*, 433.
- Walsh, D.; Tanaka, J. *J. Mater. Sci. Mater. Med.* **2001**, *12*, 339.
- Wang, M.; Kokubo, T.; Bonfield, W. *Bioceramics*. Oxford: Pergamon; 1996
- Wang, R. Z.; Weiner, S. *J. Biomech.* **1998**, *31*, 135.
- Wefel, J. S.; Harless, J. D. *J. Dent. Res.* **1987**, 66, 1640.
- Wei , J.; Li, Y. B. *Eur. Polym. J.* **2004**, *40*, 509.
- Wei, G.; Ma P. X.; *Biomaterials* **2004**, *25*, 4749.
- Weiner, S.; Addadi, L. *J. Mater. Chem.* **1997**, *7*, 689.
- Weiner, S.; Wagner, S. D. *Annu. Rev. Mater. Sci.* **1998**, *28*, 271.
- Wen, H. B.; Moradian-Oldak, J.; Fincham, A. G. *J. Dent. Res.* **2000**, *79*, 1902.
- White, S. N.; Luo, W.; Paine, M. L.; Fong, H.; Sarikaya, M.; Snead, M. L. *J. Dent. Res.* **2001**, *80*, 321.
- White, S. N.; Paine, M. L.; Luo, W.; Sarikaya, M.; Fong, H.; Yu, Z. K.; Li, Z. C.; Snead, M. L. *J. Am. Ceram. Soc.* **2000**, *83*, 238.
- Whittaker, D. K. *Arch. Oral Biol.* **1982**, *27*, 383.

- Williams, D. F. *The Williams dictionary of biomaterials.* Liverpool University Press: Liverpool, 1999.
- Wilson, C. E.; Kruyt, M. C.; de Bruijn, J. D.; van Blitterswijk, C. A.; Oner, F. C.; Verbout, A. J.; Dhert, W. J. *Biomaterials* **2006**, *27*, 302.
- Windholz M. *The Merck Index: An Encyclopedia of Chemicals, Drugs, and Biologicals*, 10th ed., Merck, Rahway, NJ, 1983.
- Wozney, J. M. *Mol. Reprod. Dev.* **1992**, *32*, 160.
- Wuthier; R. E.; Rice, G. S.; Wallace, J. E.; Weaver R. L., LeGeros, R. Z.; Eanes, E. D. *Calcif. Tissue Int.* **1985**, *37*, 401.
- Xu, H.H.; Weir, M. D.; Burguera, E. F.; Fraser, A. M. *Biomaterials* **2006**, *27*, 4279.
- Yamamoto, H.; Niwa, S.; Hori, M.; Hattori, T.; Sawai, K.; Aoki, S.; Hirano, M.; Takeuchi, H. *Biomaterials* **1998**, *19*, 1587.
- Yan, X.; Yu, C.; Zhou, X.; Tang, J.; Zhao, D. *Angew. Chem. Int. Ed. Engl.* **2004**, *43*, 5980.
- Yin, X.; Stott, M. J. *J. Chem. Phys.* **2006**, *124*, 124701.
- Yoon, B. H.; Kim, H. W.; Lee, S. H.; Bae, C. J.; Koh, Y. H.; Kong Y. M.; Kim, H. E. *Biomaterials* **2005**, *26*, 2957.
- Zapanta-LeGeros, R. *Nature* **1965**, *206*, 403.
- Zhang, W.; Liao, S. S; Cui, F. Z. *Chem. Mater.* **2003**, *15*, 3221.
- Zhang, Y.; Zhang, M. Q. *J. Biomed. Mater. Res.* **2002**, *62*, 378.
- Zheng, X.; Zhou, S.; Li, X.; Weng, J. *Biomaterials* **2006**, *27*, 4288.

CHAPTER 2
EXPERIMENTAL TECNIQUES

2.1 X-RAY DIFFRACTION (XRD)

X-ray diffraction is a non-destructive analytical technique which reveals information about the crystallographic structure, crystallite size, and preferred orientation in polycrystalline or powdered solid samples. This technique is based on observing the scattered intensity of an X-ray beam hitting a sample as a function of incident and scattered angle, polarization, and wavelength or energy.

Powder diffraction is commonly used to identify unknown substances, by comparing diffraction data against a database of Powder Diffraction Files (PDF) maintained by the International Centre for Diffraction Data (ICDD). It may also be used to characterize heterogeneous solid mixtures to determine relative abundance of crystalline compounds and, when coupled with lattice refinement techniques, such as Rietveld refinement, can provide structural information on unknown materials. Powder diffraction is also a common method for determining strains in crystalline materials.

The great advantages of the technique are: simplicity of sample preparation, rapidity of measurement and the ability to analyze mixed phases.

When X-rays hit an atom, they make the electronic cloud move as does any electromagnetic wave. The movement of these charges re-radiates waves with the same frequency (blurred slightly due to a variety of effects); this phenomenon is known as the Rayleigh scattering (or elastic scattering). The scattered waves can themselves be scattered but this secondary scattering is assumed to be negligible.

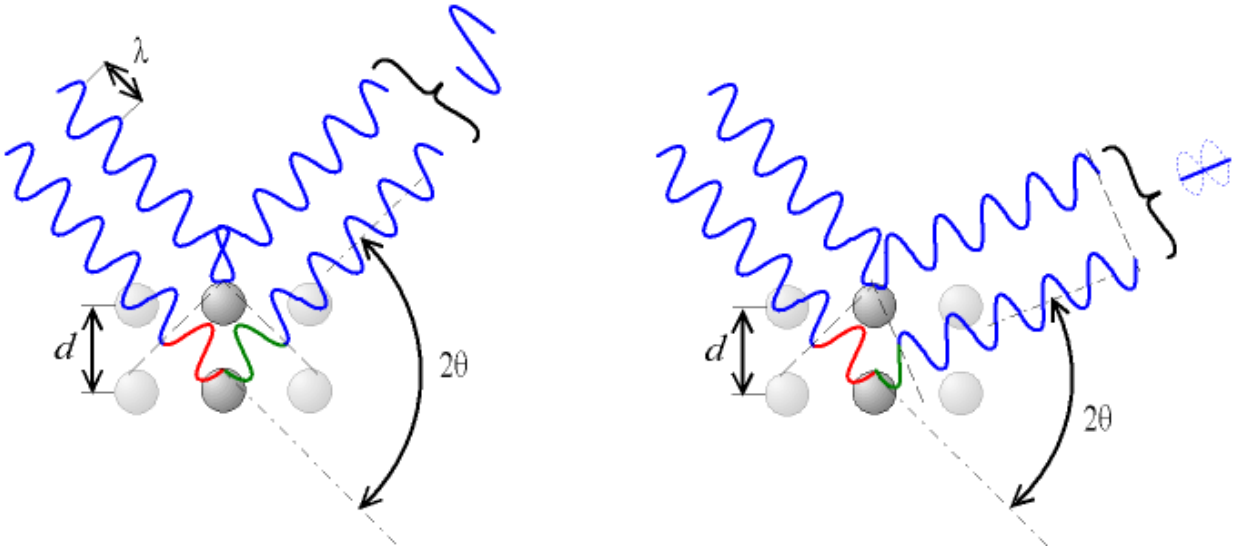

Figure 2.1 Constructive and destructive interference in Rayleigh scattering of X rays

A similar process occurs upon scattering neutron waves from the nuclei or by a coherent spin interaction with an unpaired electron. These re-emitted wave fields interfere with each other either constructively or destructively (overlapping waves either add together to produce stronger peaks or subtract from each other to some degree), producing a diffraction pattern on a detector or film (Figure 2.1).

The resulting wave interference pattern is the basis of diffraction analysis. X-ray wavelength is comparable with inter-atomic distances (~150 pm) and thus is an excellent probe for this length scale.

The interference is constructive when the phase shift is a multiple to 2π; this condition can be expressed by Bragg's law (Bragg, 1913):

$$n\lambda = 2d \sin \vartheta$$

where: n is an integer determined by the order of diffraction, λ is the wavelength of x-rays, d is the spacing between the planes in the atomic lattice, θ is the angle between the incident ray and the scattering planes

Powder diffraction data are usually presented as a diffraction pattern in which the diffracted intensity I is shown as function either of the scattering angle 2θ.

The most widespread use of powder diffraction is in the identification and characterisation of crystalline solids, each of which produces a distinctive diffraction pattern. Both the positions (corresponding to lattice spacing) and the relative intensity of the lines are indicative of a particular phase and material, providing a "fingerprint" for comparison. A multi-phase mixture will show more than one pattern superposed, allowing for determination of relative concentration.

The crystal structure of a material or the arrangement of atoms in a crystal can be described in terms of its unit cell. The unit cell is a tiny box containing the spatial arrangement of atoms. The units cells stacked in three-dimensional space describes the bulk arrangement of atoms of the crystal. The unit cell is given by its lattice parameters, the length of the cell edges and the angles between them, while the positions of the atoms inside the unit cell are described by the set of atomic positions (x_i, y_i, z_i) measured from a lattice point. The symmetry properties of the crystal are embodied in its space group. Crystal structure and symmetry play a role in determining many of its properties, such as cleavage, electronic band structure, and optical properties (Mackay *et al.*, 1963).

Although there are an infinite number of ways to specify a unit cell, for each crystal structure there is a conventional unit cell, which is chosen to display the full symmetry of the crystal. However, the conventional unit cell is not always the smallest possible choice. A primitive unit cell of a particular crystal structure is the smallest possible volume one can construct with the arrangement of atoms in the crystal such that, when stacked, completely fills the space. This primitive unit cell does not

always display all the symmetries inherent in the crystal. In a unit cell each atom has an identical environment when stacked in 3 dimensional space. In a primitive cell, each atom may not have the same environment. The crystal structure consists of the same group of atoms, the basis, positioned around each and every lattice point. This group of atoms therefore repeats indefinitely in three dimensions according to the arrangement of one of the 14 Bravais lattices (Figure 2.2).

The possible lattice centrings are:

• P: Primitive centring, lattice points on the cell corners only;

• I: Body centred, one additional lattice point at the centre of the cell;

• F: Face centred, one additional lattice point at centre of each of the faces of the cell;

• C: Centred on a single face, one additional lattice point at the centre of one of the cell faces.

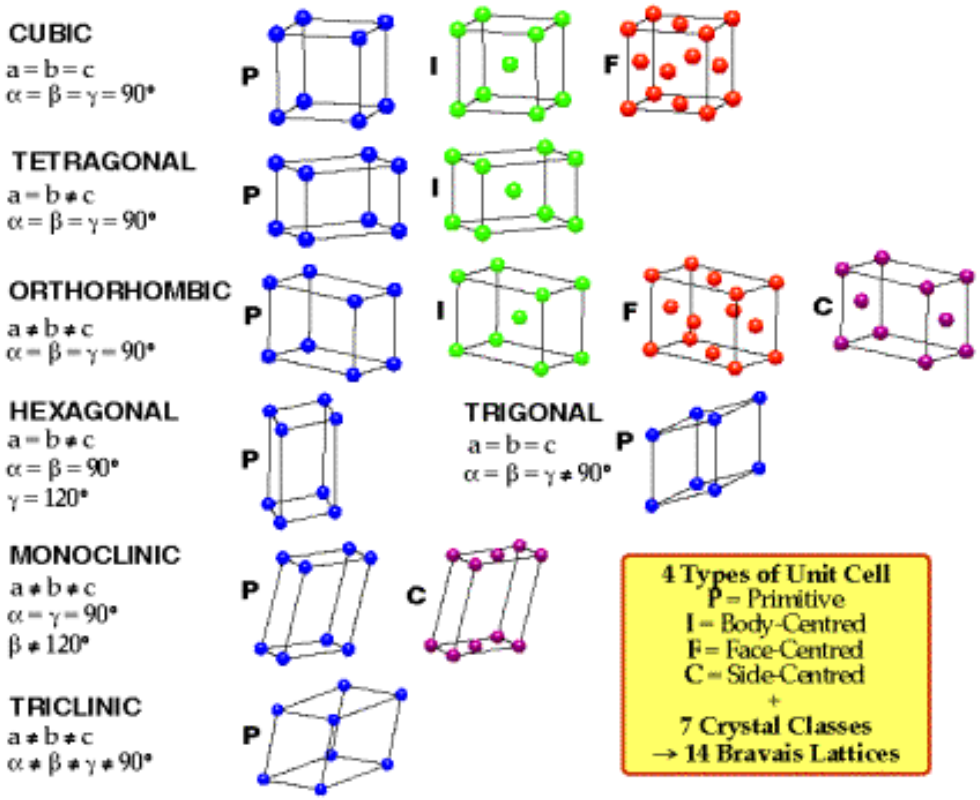

Figure 2.2 The possible 14 Bravais lattice

There are only seven possible crystal systems that atoms can pack together to produce an infinite 3D space lattice in such a way that each lattice point has an identical environment to that around every other lattice point. The simplest and most symmetric, the cubic (or isometric) system, has the symmetry of a cube. The other six systems, in order of decreasing symmetry, are hexagonal, tetragonal, rhombohedral (also known as trigonal), orthorhombic, monoclinic and triclinic. When the crystal systems are combined with the various possible lattice centrings, we arrive at the Bravais lattices. They describe the geometric arrangement of the lattice points, and thereby the translational

symmetry of the crystal. In three dimensions, there are 14 unique Bravais lattices which are distinct from one another in the translational symmetry they contain (Mackay *et al.*, 1963).

Miller indices are an useful tool to describe the lattice plans, specifying their orientation with respect to the three axis of the unit cell.

To calculate the Miller indices of a plane one has to determine the reciprocal of its intersections with the three axes in terms of fractions or multiples of the unit cells edges; these numbers are indicated in brackets, e.g. (*hkl*), which indicates an infinite number of equidistant parallel planes, so that the following expression is satisfied:

$$h\left(\frac{x}{a}\right)+k\left(\frac{y}{b}\right)+l\left(\frac{z}{c}\right)=n$$

where *n* indicates the plane position with respect to the origin. In figure 2.3 some examples of the use of Miller indices are illustrated.

In contrast to a crystalline pattern consisting of a series of sharp peaks, amorphous materials (liquids, glasses etc.) produce a broad background signal. Many polymers, organic molecules or inorganic glasses usually exhibit this kind of pattern, but often also inorganic nanostructured crystalline phases can contain also an amorphous fraction. XRD can be used to determine the degree of crystallinity by comparing the integrated intensity of the background pattern to that of the sharp peaks.

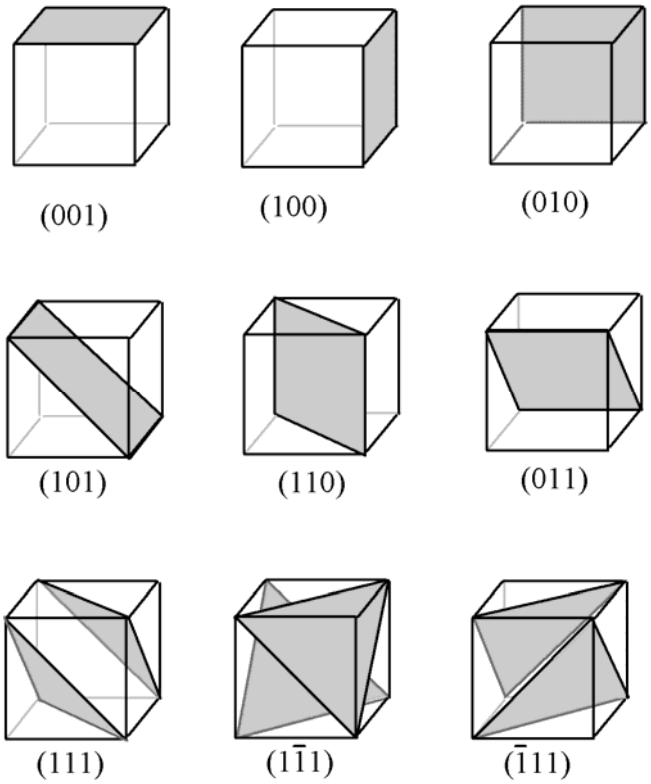

Figure 2.3 Some examples of Miller planes.

There are many factors that determine the width of a diffraction peak. These include: (i) instrumental factors, (ii) the presence of defects to the perfect lattice, (iii) differences in strain in different grains, (iv) the size of the crystallites

In powdered samples, the strain can often be neglected, so that a simple formula can be applied to obtain the average size of the diffracting coherent domains, the Scherrer formula:

$$D = \frac{K\lambda}{B\cos\vartheta}$$

Where: D is the crystallite average size, K is a form factor, usually taken as 0.9, λ is the wavelength of the incident radiation, B is the peak width corrected for the instrumental broadening and θ is the diffraction angle.

Diffractometers can be operated both in transmission and in reflection configurations. The reflection one is more common. The powder sample is filled in a small disc-like container and its surface carefully flattened. The disc is put on one axis of the diffractometer and tilted by an angle θ while a detector (scintillation counter) rotates around it on an arm at twice this angle. This configuration is known under the name Bragg-Brentano (Figure 2.4).

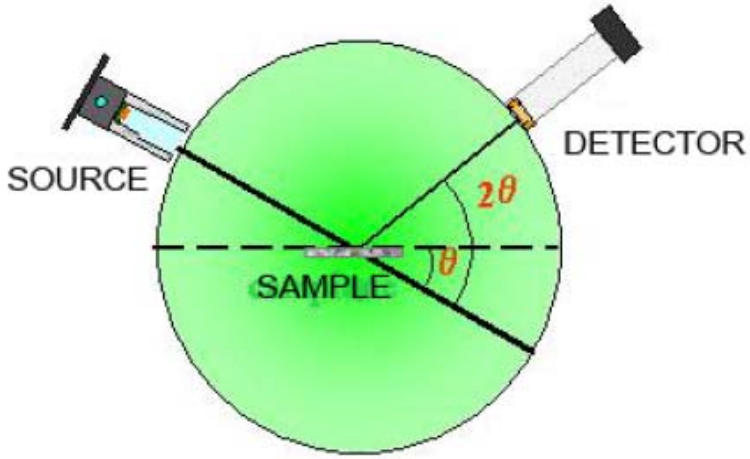

Figure 2.4 Diffractometer adopting the Bragg-Brentano geometry.

2.2 FOURIER-TRANSFORM INFRARED SPECTROSCOPY (FTIR)

Infrared spectroscopy (IR spectroscopy) is the subset of spectroscopy that deals with the infrared region of the electromagnetic spectrum (Figure 2.5).

The infrared portion of the electromagnetic spectrum is divided into three regions; the near-, mid- and far- infrared, named for their relation to the visible spectrum. The far-infrared, approximately 400-10 cm^{-1} (1000–30 μm), lying adjacent to the microwave region, has low energy and may be

used for rotational spectroscopy. The mid-infrared, approximately 4000-400 cm^{-1} (30–1.4 μm) may be used to study the fundamental vibrations and associated rotational-vibrational structure. The higher energy near-IR, approximately 14000-4000 cm^{-1} (1.4–0.8 μm) can excite overtone or harmonic vibrations.

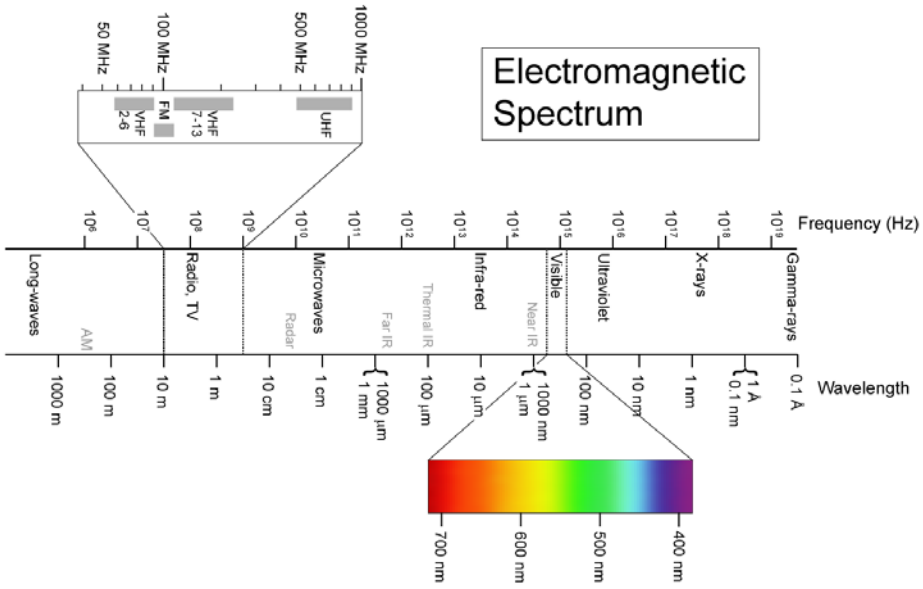

Figure 2.5 Electromagnetic spectrum

Infrared spectroscopy exploits the fact that molecules have specific frequencies at which they rotate or vibrate corresponding to discrete energy levels (Figure 2.6).

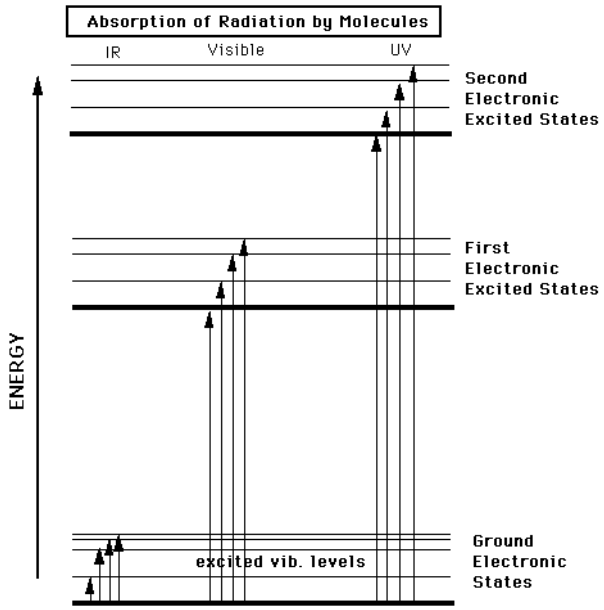

Figure 2.6 Energy Levels in Molecules

These resonant frequencies are determined by the shape of the molecular potential energy surfaces the masses of the atoms and, by the coupling of vibrational and electronic interactions in the molecule.

Thus, the resonant frequencies can be in a first approach related to the strength of the bond, and the mass of the atoms at either end of it. Thus, the frequency of the vibrations can be associated with a particular bond type and can be used for the characterization of very complex mixtures (Figure 2.7).

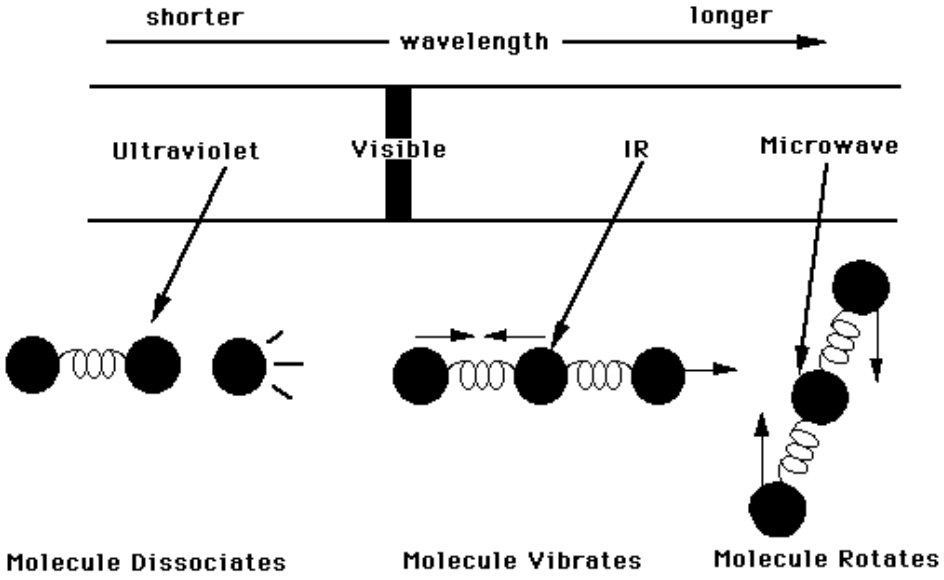

Figure 2.7 Molecular responses to radiation

The infrared spectra of a sample is collected by passing a beam of infrared light through the sample. Examination of the transmitted light reveals how much energy was absorbed at each wavelength (Figure 2.8).

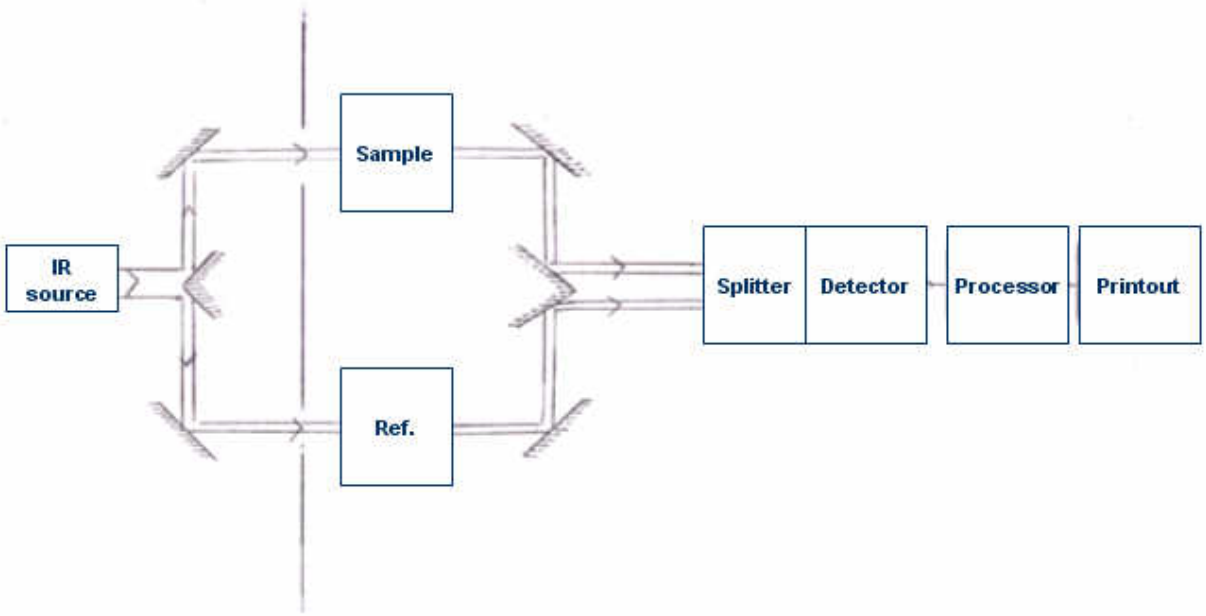

Figure 2.8 Scheme of equipment for infrared spectroscopy

This can be done with a monochromatic beam, which changes in wavelength over time, or by using a Fourier transform instrument to measure all wavelengths at once. From this, a transmittance or absorbance spectrum can be produced, showing at which IR wavelengths the sample absorbs. Analysis of these absorption characteristics reveals details about the molecular structure of the sample.

The method employed for sample preparation is to grind a quantity of the sample with potassium bromide finely (to remove scattering effects from large crystals), which is used also as a reference. This powder mixture is then crushed in a mechanical die press to form a translucent pellet through which the beam of the spectrometer can pass.

A reference is used for two reasons: to prevent fluctuations in the output of the source affecting the data and to allow the effects of the solvent to be cancelled out (the reference is usually pure solvent).

2.3 ULTRAVIOLET-VISIBLE SPECTROSCOPY (UV-VIS)

Ultraviolet-visible spectroscopy or ultraviolet-visible spectrophotometry (UV-Vis or UV/Vis) involves the spectroscopy of photons in the UV-visible region (Figure 2.5). This means it uses light in the visible and adjacent (near ultraviolet (UV) and near infrared (NIR)) ranges. The absorption in the visible ranges directly affects the colour of the chemicals involved. In this region of the electromagnetic spectrum, molecules undergo electronic transitions. This technique is complementary to fluorescence spectroscopy, in that fluorescence deals with transitions from the excited state to the ground state, while absorption measures transitions from the ground state to the excited state.

UV/Vis spectroscopy is routinely used in the quantitative determination of solutions of transition metal ions and highly conjugated organic compounds.

Solutions of transition metal ions can be coloured (i.e., absorb visible light) because d electrons within the metal atoms can be excited from one electronic state to another. The colour of metal ion solutions is strongly affected by the presence of other species, such as certain anions or ligands. Organic compounds, especially those with a high degree of conjugation, also absorb light in the UV or visible regions of the electromagnetic spectrum. The solvents for these determinations are often water for water soluble compounds, or ethanol for organic-soluble compounds. (Organic solvents may have significant UV absorption; not all solvents are suitable for use in UV spectroscopy. Ethanol absorbs very weakly at most wavelengths.) Solvent polarity and pH can effect the absorption spectrum of an organic compound. Tyrosine, for example, increases in absorption

maxima and molar extinction coefficient when pH increases from 6 to 13 or when solvent polarity decreases.

While charge transfer complexes also give rise to colours, the colours are often too intense to be used for quantitative measurement.

The Beer-Lambert law states that the absorbance of a solution is directly proportional to the solution's concentration. Thus UV/VIS spectroscopy can be used to determine the concentration of a solution. It is necessary to know how quickly the absorbance changes with concentration. This can be taken from references (tables of molar extinction coefficients), or more accurately, determined from a calibration curve.

The Beer-Lambert law states that the absorbance of a solution is directly proportional to the solution's concentration. Thus UV/VIS spectroscopy can be used to determine the concentration of a solution. It is necessary to know how quickly the absorbance changes with concentration. This can be taken from references (tables of molar extinction coefficients), or more accurately, determined from a calibration curve.

The method is most often used in a quantitative way to determine concentrations of an absorbing species in solution, using the Beer-Lambert law:

$$A = -\log_{10}\left(\frac{I}{I_0}\right) = \varepsilon \cdot c \cdot L$$

where A is the measured absorbance, I_0 is the intensity of the incident light at a given wavelength, I is the transmitted intensity, L the pathlength through the sample, and c the concentration of the absorbing species. For each species and wavelength, ε is a constant known as the molar absorptivity or extinction coefficient. This constant is a fundamental molecular property in a given solvent, at a particular temperature and pressure. The absorbance and extinction ε are sometimes defined in terms of the natural logarithm instead of the base-10 logarithm.

The instrument used in ultraviolet-visible spectroscopy is called a UV/vis spectrophotometer. It measures the intensity of light passing through a sample (I), and compares it to the intensity of light before it passes through the sample (I_0). The ratio I / I_0 is called the transmittance, and is usually expressed as a percentage (%T). The absorbance, A, is based on the transmittance:

$$A = -\log\left(\frac{\%T}{100\%}\right)$$

The basic parts of a spectrophotometer are a light source, a holder for the sample, a diffraction grating or monochromator to separate the different wavelengths of light, and a detector. The radiation source is often a Tungsten filament (300-2500 nm), a deuterium arc lamp which is continuous over the ultraviolet region (190-400 nm), and more recently light emitting diodes (LED)

and Xenon Arc Lamps for the visible wavelengths. The detector is typically a photodiode or a CCD. Photodiodes are used with monochromators, which filter the light so that only light of a single wavelength reaches the detector. Diffraction gratings are used with CCDs, which collects light of different wavelengths on different pixels.

Diagram of a single-beam UV/Vis spectrophotometer. A spectrophotometer can be either single beam or double beam. In a single beam instrument, all of the light passes through the sample cell. I_0 must be measured by removing the sample. This was the earliest design, but is still in common use in both teaching and industrial labs.

In a double-beam instrument, the light is split into two beams before it reaches the sample. One beam is used as the reference; the other beam passes through the sample. Some double-beam instruments have two detectors (photodiodes), and the sample and reference beam are measured at the same time. In other instruments, the two beams pass through a beam chopper, which blocks one beam at a time. The detector alternates between measuring the sample beam and the reference beam.

Samples for UV/Vis spectrophotometry are most often liquids, although the absorbance of gases and even of solids can also be measured. Samples are typically placed in a transparent cell, known as a cuvette. Cuvettes are typically rectangular in shape, commonly with an internal width of 1 cm. (This width becomes the path length, *L*, in the Beer-Lambert law.) Test tubes can also be used as cuvettes in some instruments. The type of sample container used must allow radiation to pass over the spectral region of interest. The most widely applicable cuvettes are made of high quality fused silica or quartz glass because these are transparent throughout the UV, visible and near infrared regions. Glass and plastic cuvettes are also common, although glass and most plastics absorb in the UV, which limits their usefulness to visible wavelengths.

2.4 INDUCTIVELY COUPLED PLASMA ATOMIC EMISSION SPECTROSCOPY (ICP-AES)

ICP-AES, also referred to as Inductively Coupled Plasma Optical Emission Spectrometry (ICP-OES), is a type of emission spectroscopy that uses a plasma (e.g. inductively coupled plasma) to produce excited atoms that emit electromagnetic radiation at a wavelength characteristic of a particular element. The intensity of the radiation is proportional to the concentration of the element, which is obtained through a previous calibration obtained with opportune standard solutions.

An inductively coupled plasma (ICP) for spectrometry is sustained in a torch that consists of three concentric tubes, usually made of quartz. The end of this torch is placed inside an induction coil supplied with a radio-frequency electric current. A flow of argon gas is introduced between the two

outermost tubes of the torch and an electrical spark is applied for a short time to introduce free electrons into the gas stream. These electrons interact with the radio-frequency magnetic field of the induction coil and are accelerated first in one direction, then the other, as the field changes at high frequency. The accelerated electrons collide with argon atoms, and sometimes a collision causes an argon atom to part with one of its electrons. The released electron is in turn accelerated by the rapidly-changing magnetic field. The process continues until the rate of release of new electrons in collisions is balanced by the rate of recombination of electrons with argon ions (atoms that have lost an electron). This produces a 'fireball' that consists mostly of argon atoms with a rather small fraction of free electrons and argon ions.

The samples to be analyzed are firstly solubilised and then introduced into the hot region through an atomizer. The temperature of the plasma is very high, of the order of 10.000 K, so that the atomization of the sample is nearly complete, improving the accuracy of the analysis. Moreover, the carrier gas is inert (usually argon), so preventing the formation of oxides.

As a droplet of atomized sample enters the central channel of the ICP, it evaporates and any solids that were dissolved in the liquid vaporize and then break down into atoms. At the temperatures prevailing in the plasma a significant proportion of the atoms of many chemical elements are ionized, each atom losing its most loosely-bound electron to form a singly charged ion.

2.5 SCANNING ELECTRON MICROSCOPY (SEM)

The scanning electron microscope (SEM) is a type of electron microscope that creates various images by focusing a high energy beam of electrons onto the surface of a sample and detecting signals from the interaction of the incident electrons with the sample's surface. The type of signals gathered in a SEM vary and can include secondary electrons, characteristic X-rays, and back scattered electrons (Figure 2.7). In a SEM, these signals come not only from the primary beam impinging upon the sample, but from other interactions within the sample near the surface.

The SEM is capable of producing high-resolution images of a sample surface in its primary use mode, secondary electron imaging. Due to the manner in which this image is created, SEM images have great depth of field yielding a characteristic three-dimensional appearance useful for understanding the surface structure of a sample. This great depth of field and the wide range of magnifications are the most familiar imaging mode for specimens in the SEM.

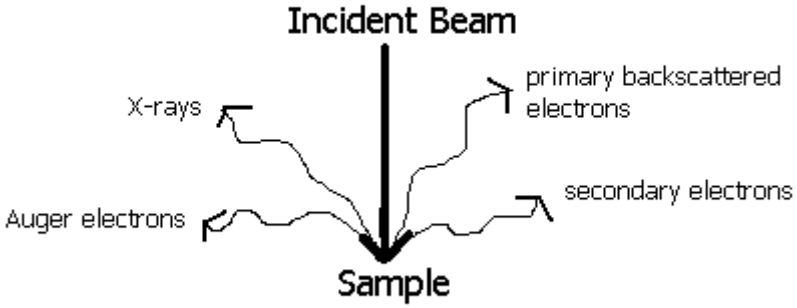

Figure 2.7 Signals produced by the interaction of the electron beam with the sample.

Characteristic x-rays are emitted when the primary beam causes the ejection of inner shell electrons from the sample and are used to tell the elemental composition of the sample. The back-scattered electrons emitted from the sample may be used alone to form an image or in conjunction with the characteristic x-rays as atomic number contrast clues to the elemental composition of the sample.
In a typical SEM, thermo-ionic electrons are emitted from a tungsten cathode and are accelerated towards an anode (Figure 2.8).

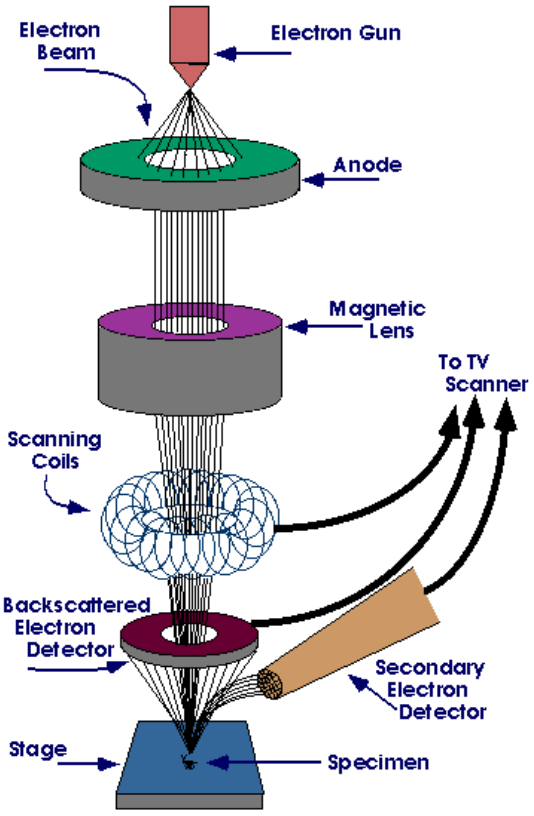

Figure 2.9 Scheme of a Scanning Electron Microscope.

Tungsten is used because it has the highest melting point and lowest vapour pressure of all metals, thereby allowing it to be heated for electron emission. The electron beam, which typically has an energy ranging from a few hundred eV to 100 keV, is focused by one or two condenser lenses into a beam with a very fine focal spot sized 0.4 nm to 5 nm. The beam passes through pairs of scanning coils or pairs of deflector plates in the electron optical column, typically in the objective lens, which deflect the beam horizontally and vertically so that it scans in a raster fashion over a rectangular area of the sample surface. When the primary electron beam interacts with the sample, the electrons lose energy by repeated scattering and absorption within a teardrop-shaped volume of the specimen known as the interaction volume, which extends from less than 100 nm to around 5 μm into the surface. The size of the interaction volume depends on the electrons' landing energy, the atomic number of the specimen and the specimen's density. The energy exchange between the electron beam and the sample results in the emission of electrons and electromagnetic radiation, which can be detected to produce an image, as described below.

The most common imaging mode monitors low energy (<50 eV) secondary electrons. Due to their low energy, these electrons originate within a few nanometers from the surface. The electrons are detected by a scintillator-photomultiplier device and the resulting signal is rendered into a two-dimensional intensity distribution that can be viewed and saved as a digital image. This process relies on a raster-scanned primary beam. The brightness of the signal depends on the number of secondary electrons reaching the detector. If the beam enters the sample perpendicular to the surface, then the activated region is uniform about the axis of the beam and a certain number of electrons "escape" from within the sample. As the angle of incidence increases, the "escape" distance of one side of the beam will decrease, and more secondary electrons will be emitted. Thus steep surfaces and edges tend to be brighter than flat surfaces, which results in images with a well-defined, three-dimensional appearance. Using this technique, resolutions less than 100 nm are possible.

The spatial resolution of the SEM depends on the size of the electron spot, which in turn depends on both the wavelength of the electrons and the magnetic electron-optical system which produces the scanning beam. The resolution is also limited by the size of the interaction volume, or the extent to which the material interacts with the electron beam.

The spot size and the interaction volume both might be large compared to the distances between atoms, so the resolution of the SEM is not high enough to image individual atoms, as is possible in the shorter wavelength (i.e. higher energy) transmission electron microscope (TEM). The SEM has compensating advantages, though, including the ability to image a comparatively large area of the

specimen; the ability to image bulk materials (not just thin films or foils); and the variety of analytical modes available for measuring the composition and nature of the specimen.

EDS (or EDX) is an analytical technique, coupled with the SEM equipment, used predominantly for the elemental analysis or chemical characterization of a specimen. Being a type of spectroscopy, it relies on the investigation of a sample through interactions between electromagnetic radiation and matter, analyzing X-rays emitted by the matter in this particular case. Its characterization capabilities are due in large part to the fundamental principle that each element of the periodic table has a unique atomic structure allowing X-rays that are characteristic of an element's atomic structure to be uniquely distinguished from each other.

To stimulate the emission of characteristic x-rays from a specimen, an high energy beam of charged particles such as electrons or protons, or a beam of x-rays, is focused into the sample to be characterized. At rest, an atom within the sample contains ground state (or unexcited) electrons situated in discrete energy levels or electron shells bound to the nucleus. The incident beam may excite an electron in an inner shell, prompting its ejection and resulting in the formation of an electron hole within the atom's electronic structure. An electron from an outer, higher-energy shell then fills the hole, and the difference in energy between the higher-energy shell and the lower energy shell is released in the form of an X-ray. The x-ray released by the electron is then detected and analyzed by the energy dispersive spectrometer. These X-rays are characteristic of the difference in energy between the two shells, and of the atomic structure of the element form which they were emitted.

A detector is used to convert X-ray energy into voltage signals; this information is sent to a pulse processor, which measures the signals and passes them onto an analyzer for data display and analysis.

2.6 TRANSMISSION ELECTRON MICROSCOPY (TEM)

Transmission electron microscopy (TEM) is a microscopy technique whereby a beam of electrons is transmitted through an ultra thin specimen, interacting with the specimen as they pass through. An image is formed from the interaction of the electrons transmitted through the specimen, which is magnified and focused onto an imaging device, such as a fluorescent screen, as is common in most TEMs, on a layer of photographic film, or to be detected by a sensor such as a CCD camera.

TEMs are capable of imaging at a significantly higher resolution than light microscopes, owing to the small de Broglie wavelength of electrons. This enables the instrument to be able to examine fine detail -- even as small as a single column of atoms, which is tens of thousands times smaller than

the smallest resolvable object in a light microscope. TEM forms a major analysis method in a range of scientific fields, in both physical and biological sciences. TEMs find application in cancer research, virology, materials science as well as pollution and semiconductor research.

At smaller magnifications TEM image contrast is due to absorption of electrons in the material, due to the thickness and composition of the material. At higher magnifications complex wave interactions modulate the intensity of the image, requiring expert analysis of observed images. Alternate modes of use allow for the TEM to observe modulations in chemical identity, crystal orientation, electronic structure and sample induced electron phase shift as well as the regular absorption based imaging.

The first TEM was built by Max Knoll and Ernst Ruska in 1931, with this group developing the first TEM with resolving power greater than that of light in 1933 and the first commercial TEM in 1939 (Ruska, 1986).

A TEM is composed of several components, which include a vacuum system in which the electrons travel, an electron emission source for generation of the electron stream, a series of electromagnetic lenses, as well as electrostatic plates. The latter two allow the operator to guide and manipulate the beam as required. Also required is a device to allow the insertion into, motion within, and removal of specimens from the beam path. Imaging devices are subsequently used to create an image from the electrons that exit the system.

In order to allow for uninterrupted passage of electrons, the TEM must be evacuated to low pressures, typically on the order of 10-4 to 10-8 kPa.[13] The need for this is twofold, firstly the allowance for the voltage difference between the cathode and the ground without generating an arc, and secondly to reduce the collision frequency of electrons with gas atoms to negligible levels -- this effect is characterised by the mean free path. As the TEM, unlike a CRT, is a system where components must be replaced, specimens inserted and particularly on older TEMs, film cartridges must be replenished, the ability to re-evacuate a TEM on a regular basis is required. As such, TEMs are equipped with extensive pumping systems and are not permanently vacuum sealed.

To evacuate a TEM, the vacuum system consists of several stages. High pressure "low vacuum" pumps such as Diaphragm pumps are utilized to perform evacuation of the TEM to a sufficiently low pressure to allow the operation of turbomolecular or diffusion pumps which can reduce the TEM's in column pressure even further. To allow for the low vacuum pump to not require continuous operation, whilst accommodating continuous operation of the turbomolecular pumps, the vacuum side of a low pressure pump may be connected to evacuated chambers which serves no other purpose but the accommodation of the turbomolecular exhaust gases. TEMs may be isolated into chambers by the use of gate valves, which allow for sections of the TEM to be subjected to

differing vacuum quality. This is often done as a preventative measure to prevent inadvertent loss of vacuum in critical locations, such as the electron gun in high resolution TEMs (Crowe *et al.*, 1969). For high voltage TEMs, even very high vacuum conditions (very low pressure) are sufficient to allow for the generation of an electrical arc, particularly at the TEM cathode. As such for higher voltage TEMs a third vacuum system may operate, with the gun isolated from the main chamber either by use of gate valves or by the use of a differential pumping aperture, which is essentially a small hole that prevents gas molecules from entering a high quality vacuum system faster than they can be pumped out. For these very low pressures either an ion pump or a getter material is used.

Poor vacuum in a TEM can cause several problems, from deposition of gas inside the TEM onto the specimen as it is being viewed through a process known as electron beam induced deposition, or in more severe cases damage to the cathode from a electrical discharge. Vacuum problems owing to specimen sublimation are limited by the use of a cold trap to adsorb sublimated gases in the vicinity of the specimen.

The specimen stage design allows for the external insertion of a TEM sample into the vacuum, ideally with minimal disruption to the vacuum inside the TEM. To allow for the transport of samples between multiple TEMs, a common standard of sample "grid" design is a 3 mm diameter brass ring, with a thickness of 100 um and an inner diameter of approximately 2.5 mm into which the sample is placed. The TEM stage and holder pair are designed to accommodate such specimens, although a wide variety of designs of stages and holder exist.

Once inserted into a TEM the sample often has to be manipulated to present the region of interest to the beam, sometimes, such as in single grain diffraction, in a specific orientation. To accommodate this, the TEM stage includes a mechanism for the translation (XYZ) and often rotation of the sample. Thus a TEM stage may provide four degrees of freedom for the motion of the specimen. Additional degrees of freedom can be provided by specialised holder designs. Of note however is that some stage designs, such as so-called "vertical insertion" stages, may simply only have X-Y translation available. The design criteria of TEM stages are complex, owing to the simultaneous requirements of mechanical and electron-optical constraints and have thus generated many unique implementations.

A TEM stage is required to have the ability to hold a specimen and direct the region of interest to the beam path. As the TEM can operate over a wide range of magnifications, the stage must simultaneously be highly resistant to mechanical drift, with drift requirements as low as a few nm/minute whilst be able to be driven at speeds of from to several mm/minute down to several um/minute. Earlier designs of TEM accomplished this with a complex set of mechanical downgearing devices, allowing the operator to finely control the motion of the stage by several

rotating rods. Modern devices may use electrical stage designs, using screw gearing in concert with stepper motors, providing the operator with a computer-based stage input, such as a joystick or trackball.

Two main designs for stages in a TEM exist, the top entry and the side-entry version. Each design must accommodate the matching holder to allow for specimen insertion without either damaging delicate TEM optics nor allowing gas into the TEM vacuum.

The top entry holder consists of a cartridge that is several cm long with a bore drilled down the cartridge axis. The specimen is loaded into the bore, possibly utilizing a small screw ring to hold the sample in place. This cartridge is inserted into an airlock with the bore perpendicular to the TEM optic axis. When sealed, the airlock is manipulated to push the cartridge such that the cartridge falls into place, where the bore hole becomes aligned with the beam axis, such that the beam travels down the cartridge bore and into the specimen. Such designs are typically unable to be tilted without blocking the beam path or interfering with the objective lens.

The second design is the side entry holder, where the specimen is placed near the tip of a long metal (brass or stainless steel) rod, with the specimen placed flat in a small bore. Along the rod are several polymer vacuum rings to allow for the formation of a vacuum seal of sufficient quality, when inserted into the stage. The stage is thus designed to accommodate the rod, placing the sample either in between or near the objective lens, dependent upon the objective design. When inserted into the stage, the side entry holder has its tip contained within the TEM vacuum, and the base is presented to atmosphere, the airlock formed by the vacuum rings (Figure 2.10).

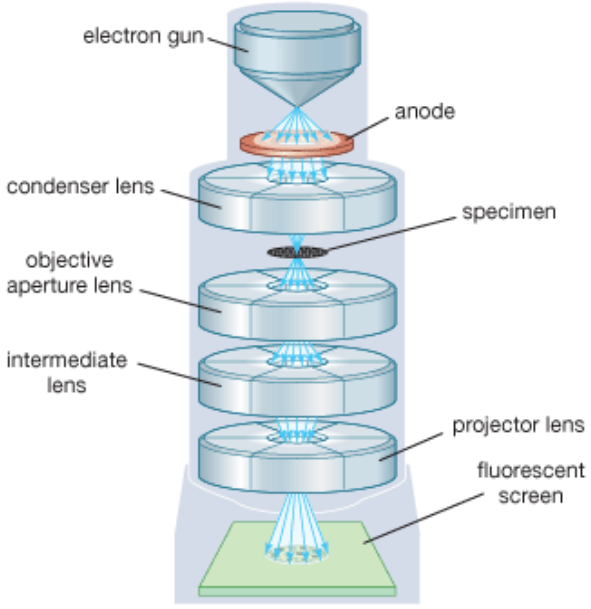

Figure 2.10 Scheme of a Transmission Electron Microscope

Insertion procedures for side entry TEM holders typically involve the rotation of the sample to trigger micro switches that initiate different pump cycles to minimize vacuum leakage into the chamber.

2.7 THERMOGRAVIMETRIC AND THERMOANALYTICAL ANALYSES (TG-DTA)

Thermogravimetric Analysis or TGA is a type of testing that is performed on samples to determine changes in weight in relation to change in temperature. Such analysis relies on a high degree of precision in three measurements: weight, temperature, and temperature change. As many weight loss curves look similar, the weight loss curve may require transformation before results may be interpreted. A derivative weight loss curve can be used to tell the point at which weight loss is most apparent.

The analyzer usually consists of a high-precision balance with a pan loaded with the sample. The sample is placed in a small electrically heated oven with a thermocouple to accurately measure the temperature. The atmosphere may be purged with an inert gas to prevent oxidation or other undesired reactions. A computer is used to control the instrument.

Analysis is carried out by raising the temperature gradually and plotting weight against temperature. After the data is obtained, curve smoothing and other operations may be done such as to find the exact points of inflection.

Differential thermal analysis (or DTA) is a thermoanalytic technique. In DTA, the material under study and an inert reference (Al_2O_3 in our case) are heated (or cooled) under identical conditions, while recording any temperature difference between sample and reference. This differential temperature is then plotted against time, or against temperature (DTA curve or thermogram). Changes in the sample, either exothermic or endothermic, can be detected relative to the inert reference. Thus, a DTA curve provides data on the transformations that have occurred, such as phase transitions, glass transitions, crystallization, melting and sublimation. The area under a DTA peak can be to the enthalpy change and it is not affected by the heat capacity of the sample.

A DTA apparatus consist of a sample holder comprising thermocouples, sample containers and a ceramic or metallic block; a furnace; a temperature programmer; and a recording system. The key feature is the existence of two thermocouples connected to a voltmeter. One thermocouple is placed in the inert reference material, while the other is placed in a sample of the material under study. As the temperature is increased, there will be a brief deflection of the voltmeter if the sample is undergoing a phase transition. This occurs because the input of heat will raise the temperature of the inert substance, but be incorporated as latent heat in the material changing phase.

2.8 SPECIFIC SURFACE AREA (BET)

Specific surface area is a material property of solids which measures the total surface area per unit of mass, solid or bulk volume, or cross-sectional area.

It is a derived scientific value that can be used to determine the type and properties of a material (e.g. soil). It is defined either by surface area divided by mass (with units of m^2/kg), or surface area divided by the volume (units of m^2/m^3 or m^{-1})

The SSA can be measured by adsorption using the BET isotherm. This has the advantage of measuring the surface of fine structures and deep texture on the particles.

BET theory is a well-known rule for the physical adsorption of gas molecules on a solid surface, that is basis for an important analysis technique for the measurement of the specific surface area of a material. In 1938, Stephen Brunauer, Paul Hugh Emmett, and Edward Teller published an article about the BET theory in a journal for the first time; "BET" consists of the first initials of their family names (Brunauer *et al.*, 1938).

The concept of the theory is an extension of the Langmuir theory, which is a theory for monolayer molecular adsorption, to multilayer adsorption with the following hypotheses: (i) gas molecules physically adsorb on a solid in layers infinitely; (ii) there is no interaction between each adsorption layer; and (iii) the Langmuir theory can be applied to each layer. The resulting BET equation is expressed by (1):

$$\frac{1}{v\left[\left(\frac{P_0}{P}\right)-1\right]} = \frac{c-1}{v_m c}\left(\frac{P}{P_0}\right) + \frac{1}{v_m c} \qquad (1)$$

where P and P_0 are the equilibrium and the saturation pressure of adsorbates at the temperature of adsorption, v is the adsorbed gas quantity (for example, in volume units), and v_m is the monolayer adsorbed gas quantity. c is the BET constant, which is expressed by (2):

$$c = \exp\left(\frac{E_1 - E_L}{RT}\right) \qquad (2)$$

where E_1 is the heat of adsorption for the first layer, and E_L is that for the second and higher layers and is equal to the heat of liquefaction.

Equation (1) is an adsorption isotherm and can be plotted as a straight line with $1/v[(P_0/P)-1]$ on the y-axis and $\varphi = P/P_0$ on the x-axis according to experimental results. This plot is called a BET plot. The linear relationship of this equation is maintained only in the range of $0.05 < P/P_0 < 0.35$. The value of the slope A and the y-intercept I of the line are used to calculate the monolayer adsorbed gas quantity v_m and the BET constant c. The following equations can be used:

$$v_m = \frac{1}{A+I} \qquad (3)$$

$$c = 1 + \frac{A}{I} \qquad (4)$$

The BET method is widely used in surface science for the calculation of surface areas of solids by physical adsorption of gas molecules. A total surface area S_{total} and a specific surface area S are evaluated by the following equations:

$$S_{BET,total} = \frac{v_m N s}{V} \quad (5)$$

$$S_{BET} = \frac{S_{TOTAL}}{a} \qquad (6)$$

where N is Avogadro's number, s is the adsorption cross section, V is the molar volume of adsorbent gas and a is the molar weight of adsorbed species.

2.9 X-RAY PHOTOELECTRON SPECTROSCOPY (XPS)

X-ray photoelectron spectroscopy (XPS) is a quantitative spectroscopic technique that measures the elemental composition, empirical formula, chemical state and electronic state of the elements that exist within a material. XPS spectra are obtained by irradiating a material with a beam of aluminium or magnesium X-rays while simultaneously measuring the kinetic energy (KE) and number of electrons that escape from the top 1 to 10 nm of the material being analyzed. XPS requires ultra-high vacuum (UHV) conditions.

XPS is a surface chemical analysis technique that can be used to analyze the surface chemistry of a material in its "as received" state, or after some treatment such as: fracturing, cutting or scraping in air or UHV to expose the bulk chemistry, ion beam etching to clean off some of the surface contamination, exposure to heat to study the changes due to heating, exposure to reactive gases or solutions, exposure to ion beam implant, exposure to ultraviolet light, for example.

XPS is also known as ESCA, an abbreviation for Electron Spectroscopy for Chemical Analysis.

XPS detects all elements with an atomic number (Z) of 3 (lithium) and above. This limitation means that it cannot detect hydrogen (Z=1) or helium (Z=2).

Detection limits for most of the elements are in the parts per thousand range. Detections limits of parts per million (ppm) are possible, but require special conditions: concentration at top surface or very long collection time (overnight).

A typical XPS spectrum is a plot of the number of electrons detected (Y-axis, ordinate) versus the binding energy of the electrons detected (X-axis, abscissa). Each element produces a characteristic

set of XPS peaks at characteristic binding energy values that directly identify each element that exist in or on the surface of the material being analyzed. These characteristic peaks correspond to the electron configuration of the electrons within the atoms, e.g., 1s, 2s, 2p, 3s, etc. The number of detected electrons in each of the characteristic peaks is directly related to the amount of element within the area (volume) irradiated. To generate atomic percentage values, each raw XPS signal must be corrected by dividing its signal intensity (number of electrons detected) by a "relative sensitivity factor" (RSF) and normalized over all of the elements detected.

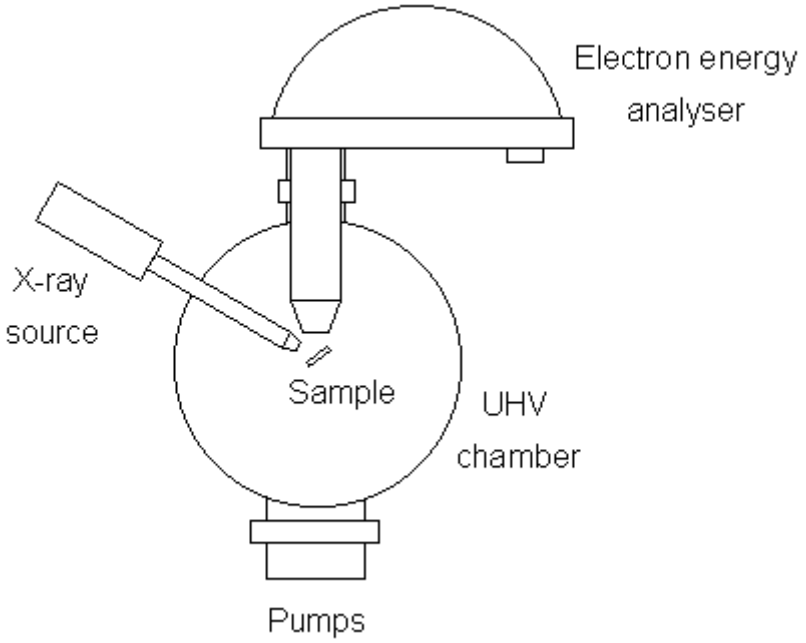

Figure 2. Scheme of XPS apparatus

To count the number of electrons at each KE value, with the minimum of error, XPS must be performed under ultra-high vacuum (UHV) conditions because electron counting detectors in XPS instruments are typically one meter away from the material irradiated with X-rays

It is important to note that XPS detects only those electrons that have actually escaped into the vacuum of the instrument. The photo-emitted electrons that have escaped into the vacuum of the instrument are those that originated from within the top 10 to 12 nm of the material. All of the deeper photo-emitted electrons, which were generated as the X-rays penetrated 1–5 micrometers of the material, are either recaptured or trapped in various excited states within the material. For most applications, it is, in effect, a non-destructive technique that measures the surface chemistry of any material.

XPS is used to measure: (i) elemental composition of the surface (1–10 nm usually), (ii) empirical formula of pure materials, (iii) elements that contaminate a surface, (v) chemical or electronic state

of each element in the surface, (vi) uniformity of elemental composition across the top surface (aka, line profiling or mapping) and (vii)uniformity of elemental composition as a function of ion beam etching (aka, depth profiling) (Wagner *et al.*, 1979).

XPS can be performed using either a commercially built XPS system, a privately built XPS system or a Synchrotron-based light source combined with a custom designed electron analyzer. Commercial XPS instruments in the year 2005 used either a highly focused 20 to 200 micrometer beam of monochromatic aluminium K-alpha X-rays or a broad 10-30 mm beam of non-monochromatic (polychromatic) magnesium X-rays. A few, special design XPS instruments can analyze volatile liquids or gases, materials at low or high temperatures or materials at roughly 1 torr vacuum, but there are relatively few of these types of XPS systems.

The photoemission spectroscopy is based on the photoelectric effect. In this process a photon with a well defined energy *h*, hits the sample and is absorbed. If the photon energy is high enough, the excited electron escapes from the surface and their kinetic energy is roughly given by. Because the energy of a particular X-ray wavelength equals a known quantity, we can determine the electron binding energy (BE) of each of the emitted electrons by using an equation that is based on the work of Ernest Rutherford (1914):

$$E_{binding} = E_{photon} - E_{kinetic} - \phi$$

where E_{binding} is the energy of the electron emitted from one electron configuration within the atom, E_{photon} is the energy of the X-ray photons being used, E_{kinetic} is the kinetic energy of the emitted electron as measured by the instrument and Φ is the work function of the spectrometer (not the material). The kinetic energy of the photoelectrons depends strongly on the excited atoms and therefore gives elemental information. Moreover the energy position and the peak lineshape identify the chemical state of the surface atoms and, analysing their small variations, it is possible to determine the compound. In conclusion the XPS technique allows us to determine the different atomic species (elemental analysis), the atomic concentration and the chemical state of the sample.

REFERENCES

- Bragg, W.L. *Proceedings of the Cambridge Philosophical Society*, **1913**, *17*, 43.
- Brunauer, S. P.; Emmet, P. H.; Teller, E. *J. Am. Chem. Soc.* **1938**, *60*,309.
- Crewe, A.V.; Isaacson, M.; Johnson, D. *Rev. Sci. Inst.* **1969**, *40*, 241.
- Lindau, I.; Pianetta, P.; Doniach S.; Spicer W. E. *Nature*, **1974**, *250*, 214.
- Mackay A. L.; Pawley G. S. *Acta. Cryst.* **1963**, *16*, 11.
- Ruska, E. *Nobel Prize Lecture*, 1986.

- Wagner, C. D.; Riggs, W. M.; Davis, L. E.; Moulder, J. F.; Mullenberg, G. E. Handbook of X-ray Photoelectron Spectroscopy, Eden Prairie, MN, USA ,1979.

CHAPTER 3
BIOMIMETIC HYDROXYAPATITE NANOCRYSTALS AS BONE SUBSTITUTE WITH DRUGS DELIVERY FUNCTION

3.1 STATUS OF THE ART

Calcium phosphates are physiological constituents of bones and are used to produce biomaterials for bone repair (Yuan *et al.*, 2004). However, bioinert calcium phosphates, which have no influence on the surrounding living tissue (Aoki *et al.*, 1979; Rodriguez-Lorenzo *et al.*, 2001), are increasingly being substituted by bioactive calcium phosphates that can interact with the surrounding bone tissue and promote faster formation of new bone. The chemical and biological properties of the latter are strictly linked to their nanoscale dimensions, which require a nanoscience approach. Moreover, as the mineral phase of bone is constituted of carbonated hydroxyapatite (HA) crystals with a length of about 100 nm, width of 20–30 nm, and thickness of 3–6 nm, biomimetic calcium phosphates need to be synthesized with similar nanoscale dimensions, as well as with properties such as low crystallinity, nonstoichiometric composition, crystalline disorder, and the presence of carbonate ions in the crystal lattice. Indeed, the excellent biological properties of HA, such as nontoxicity, lack of inflammatory and immunitary responses, and high bio-resorbability can be significantly increased by lowering the crystallinity of synthetic HA (Ferraz *et al.*, 2004). Furthermore, the surface functionalization of HA nanocrystals with bioactive molecules makes them able to transfer information to and act selectively on the biological environment, and this represents a main challenge for innovative bone substitute materials. In this context, the synthesis of apatite nanocrystals loaded with antitumor drugs that can be released by a controlled kinetic process represents an attractive goal. For example, the application of such a material to the chemotherapeutic treatments of osteosarcoma could result in tumour inhibition accompanied by low levels of systemic toxicity (Lebugle *et al.*, 2002; Miura *et al.*, 1995; Tahara *et al.*, 2001; Uchida *et al.*, 1992).

For many years, cis-diamminedichloridoplatinum(II) (cisplatin; CDDP) has been widely utilized as an anticancer drug despite its nephrotoxicity and other side effects observed for high-dose treatment; indeed, it is one of the most active antitumor agents in the treatment of osteosarcoma (Rosemberg, 1979; Kelman *et al.*, 1979; Zwelling *et al.*, 1979; Segal *et al.*, 1985; De Wall *et al.*, 1990). The adsorption and release of cisplatin by slurries of synthetic HA crystals in aqueous media has been investigated as a function of ionic composition and the data indicated that chloride ions reverse the hydrolysis and that acid dissociation of the aquated species favours binding to calcium phosphate (Barroug *et al.*, 2002). Moreover, investigations carried out using either poorly or well

crystallized carbonated HA have shown that cisplatin adsorption increases with decreasing HA crystallinity and that the less crystalline the material, the slower the drug release (Barroug *et al.*, 2004). This result is particularly interesting because the poorly crystalline apatite examined exhibits a surface area, morphology, crystallite size and Ca/P molar ratio close to those observed for bone apatite crystals.

Calcium deficient apatites have also been investigated as platforms for the specific delivery to bone of geminal bisphosphonates (BPs), which are a class of drugs developed for use in various diseases of bone, tooth, and calcium metabolism (Josse *et al.*, 2004; Roussiere *et al.*, 2005). BPs are characterized by two phosphonate groups attached to a single carbon atom and have strong affinity for Ca^{2+} ions of bone apatite. This property is the basis for their use as inhibitors of ectopic calcification and of bone resorption (Figure 3.1).

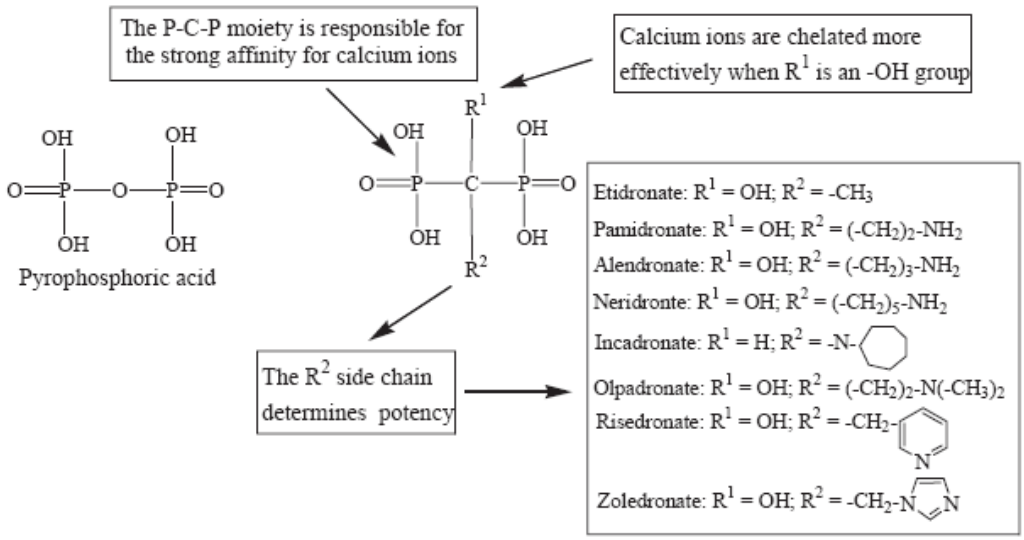

Figure 3.1 Bisphoshonates used in therapy

In general, the physicochemical effects of BPs include binding to crystals of calcium phosphate and inhibition of their growth, aggregation, and dissolution. Some BPs, such as alendronate, have already been approved for clinical use in Paget's disease, hypercalcemia of malignancy, and osteoporosis (Russel *et al.*, 1999; Ezra *et al.,* 2000; Lin, 1999).

Significantly, the basic P–C–P structure of BPs can be widely modified by changing the substituents at the central carbon atom. These changes are likely to influence the behaviour of BPs in the biochemical processes. However, studies of the solid/liquid interfacial properties of HA/BPs conjugates have shown that differences among the bisphosphonates may also influence their mechanisms for binding and inhibiting crystal growth and dissolution. Thus differences among potent bisphosphonates, such as the apparently more prolonged duration of action of alendronate

and zoledronate compared with the more readily reversible effects of etidronate and risedronate, can be explained in part by their ability to absorb onto bone minerals (Nancollas *et al.*, 2006).

Although the mechanisms for binding of cisplatin and alendronate onto different HA surfaces has been separately investigated (Barroug *et al.*, 2002; Barroug *et al.*, 2004; Nancollas *et al.*, 2006), a comparative study of their interaction onto apatitic nanocrystals synthesised with variable surface areas and crystal dimensions within the range of biomimetic parameters, has not been undertaken even though a detailed solid/surface characterization of these systems would provide important knowledge for designing new and more effective treatment systems. Moreover, platinum(II) compounds with aminophosphonic acids have also been proposed as a means for targeting a cytotoxic moiety to the bone surface (Wingen *et al.*, 1985; Bloemnik *et al.*, 1994). These compounds exhibit antimetastatic activity and reduce bone tumor volume, and are less nephrotoxic than cisplatin (Klenner *et al.*, 1990; Klenner *et al.*, 1993). To our knowledge, experimental investigations concerning Pt^{II}-aminophosphonic acid interactions with HA nanocrystals have not yet been undertaken.

3.2 AIM OF THE WORK

The aim of the present study is to develop new biomimetic apatite nanocrystals for potential use in bone implantation, which in addition function as a local targeted delivery system for anticancer and antimetastatic drugs with controlled release properties. As already pointed out (Barroug *et al.*, 1998; Guicheux *et al.*, 1997; Palazzo *et al.*, 2005), the adsorption and release of bioactive molecules are strongly affected not only by the chemical properties of the drug molecule but also by the chemical and structural characteristics of the HA substrates. Thus, the adsorption and release of cisplatin (Figure 3.2a), alendronate (Figure 3.2b), and di(ethylenediamineplatinum) medronate (DPM) (Figure 3.2c) using two biomimetic synthetic hydroxyapatite nanocrystal materials with either plate-shaped (HAps) or needle-shaped (HAns) morphologies and with different physicochemical surface properties, have been investigated.

Cisplatin and DPM are comparable in water solubility (1–2 $mgmL^{-1}$ and 0.9 $mgmL^{-1}$ at room temperature, respectively), while alendronate is much more soluble (10 $mgmL^{-1}$ at room temperature). The pK_a values for the alendronate phosphate groups are: pK_{a1} = 1.35; pK_{a2} = 2.87; pK_{a3} = 7.03; pK_{a4} = 11.3, whereas no pKa values are reported for the platinum complexes because metal ion coordination results in loss of phosphonate basicity (Yotsuyanagi *et al.*, 2002).

These bioactive molecules were chosen in order to compare the behavior of metal based drugs (CDDP and DPM) with that of a classical organic drug (alendronate), and evaluate the effect of the

overall charge of the drug molecule on influencing the drug affinity for apatite nanocrystals with variable structural and chemical properties (Palazzo *et al.*, 2007).

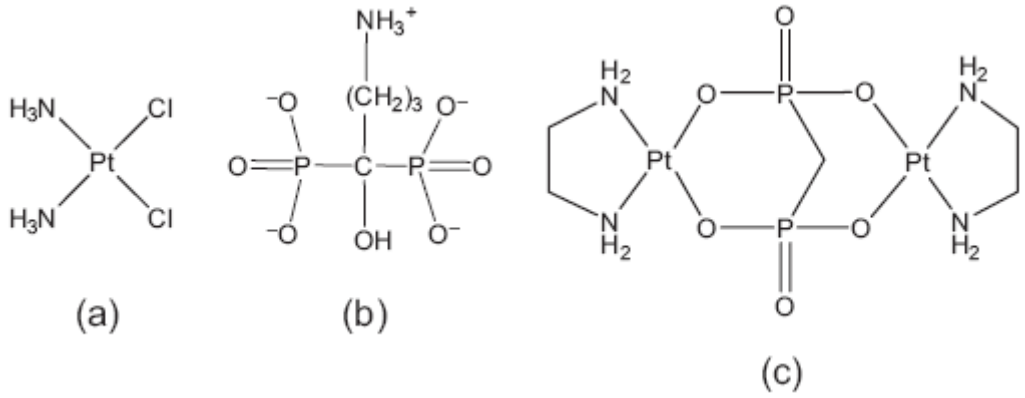

Figure 3.2 Molecular structure of a) cis-diamminedichloridoplatinum(II) (cisplatin, CDDP), b) alendronate (the overall negative charge is neutralized by different cations), and c) di(ethylenediamineplatinum)medronate (DPM).

3.3 Synthesis and characterization of the HA nanocrystals used as drug carriers

HA nanocrystals with nearly stoichiometric bulk Ca/P ratio (1.67, inductively coupled plasma (ICP) analysis) were synthesized according to two different procedures to produce plate or needle-shaped bonelike apatite phases with different physical properties (Table 3.1).

Needle-shaped HA nanocrystals (HAns) were synthesized according to a previous method with some modifications (Guaber *et al.*, 2006; Landi *et al.*, 2000). Nanocrystals were precipitated from an aqueous suspension of $Ca(OH)_2$ (ca. 0.17 $moldm^{-3}$) by slow addition of H_3PO_4 (0.15 M in water). The reaction mixture was stirred at 37 °C for 24 h, then stirring was suspended and the mixture was left standing for 2 h to allow deposition of the inorganic phase. This was isolated by filtration of the mother liquor, repeatedly washed with water and freeze-dried. The fraction of needle-shaped nanocrystals having a granular dimension ranging between 100–150 lm was selected for the investigation. Plate-shaped HA nanocrystals (HAps) were synthesized according to a previous method with some modifications (Liou *et al.*, 2004). The nanocrystals were precipitated from an aqueous solution of $(NH_4)_3PO_4$ by slow addition of an aqueous solution of $Ca(CH_3COO)_2$ (8.5 mM) keeping the pH at a constant value of 10 by addition of a $(NH_4)OH$ solution. The reaction mixture was stirred at 37 °C for 72 h and then the deposited inorganic phase was isolated by

filtration of the solution, repeatedly washed with water, and freeze-dried. The fraction of plate-shaped crystals having granular dimensions ranging from 100 to 150 μm was selected for the study. Transmission electron microscopy (TEM) investigations were carried out using a Philips CM 100 instrument. The powdered samples were ultrasonically dispersed in ultrapure water and then a few droplets of the slurry deposited on holey-carbon foils supported on conventional copper microgrids. Powder X-ray diffraction (XRD) patterns were collected using a Philips PW 1710 powder diffractometer equipped with a secondary graphite monochromator using CuKa radiation generated at 40 kV and 40 mA. The instrument was configured with a 1° divergence and 0.2 mm receiving slits. The samples were prepared using the front loading of standard aluminium sample holders which were 1 mm deep, 20 mm high, and 15 mm wide. The 2θ range was from 5° to 60° with a step size (°2θ) of 0.05 and a counting time of 3 s. Crystal domain size along the c direction was calculated applying Scherrer's formula:

$$L_{(002)} = \frac{0.94\lambda}{\left[\cos\theta\left(\sqrt{\Delta_r{}^2 - \Delta_0^2}\right)\right]} \quad (1)$$

where *h* is the diffraction angle for plane (002), Δ_r and Δ_0 the widths in radians of reflection (002) at half height for the synthesized and the reference HA materials, respectively, and k = 1.5405 Å. The degree of HA crystallinity was evaluated according to the formula:

$$Cristallinity = \left(\frac{X}{Y}\right)100 \quad (2)$$

where *X*= net area of diffracted peaks, and *Y*= net area of diffracted peaks + background area (Erkmen, 1999).

Specific surface area measurements were undertaken using a Carlo Erba Sorpty 1750 instrument by measuring N_2 adsorption at 77 K and adopting the well-known Brunauer–Emmett–Teller (BET) procedure (Brunauer *et al.*, 1938). Calcium, and phosphorous contents were measured using inductively coupled plasma (ICP) optical emission spectrometry (OES) using a Perkin-Elmer Optima 4200 DV. The samples were initially dissolved in ultrapure nitric acid 1% to obtain elemental concentrations of between 1 and 8 ppm. X-ray photoemission spectroscopy (XPS) analyses were performed in an M-Probe Instrument (SSI) equipped with a monochromatic AlKa source (1486.6 eV) with a spot size of 200 × 750 μm and pass energy of 25 eV, providing a resolution for 0.74 eV. With a monochromatic source, an electron flood gun was used to compensate the build up of positive charge on the insulator samples during the analyses. 10 eV electrons were selected to perform measurements on these samples. The accuracy of the reported binding energies (BE) was estimated

to be -0.2 eV. The quantitative data were also accurately checked and reproduced several times (at least ten times for each sample) and the percentage error was estimated to be –1%

The surface Ca/P ratios determined by X-ray photoemission spectroscopy (XPS) analyses were significantly lower, indicating calcium deficiency as a result of surface disorder. In addition, although the bulk Ca/P ratios were similar, the surface Ca/P ratio was lower for the HAns nanocrystals compared with the HAps particles, suggesting that the former were more surface deficient in calcium ions.

Table 3.1 Physicochemical characteristics of the two different types of HA nanocrystals used as drug carriers. Values are mean ± SD.

	HAns	HAps
Degree of crystallinity [%]	52 ± 8	30 ± 4
Domain size along the c direction [Å]	350 ± 15	230 ± 10
Bulk Ca/P molar ratio	1.65 ± 0.1	1.62 ± 0.1
Surface Ca/P atomic ratio	1.30 ± 0.05	1.45 ± 0.05
Specific surface area [m^2 g^{-1}]	100 ± 5	120 ± 6

Transmission electron microscopy (TEM) revealed the presence of clusters of plate-like (length 25–5 nm) or needle-like (length 100–20 nm) nanoparticles for the HAps and HAns samples, respectively (Figure 3.3 A and B). The specific surface area of the HAps nanocrystals was slightly larger than that determined for the HAns particles (Table 3.1).

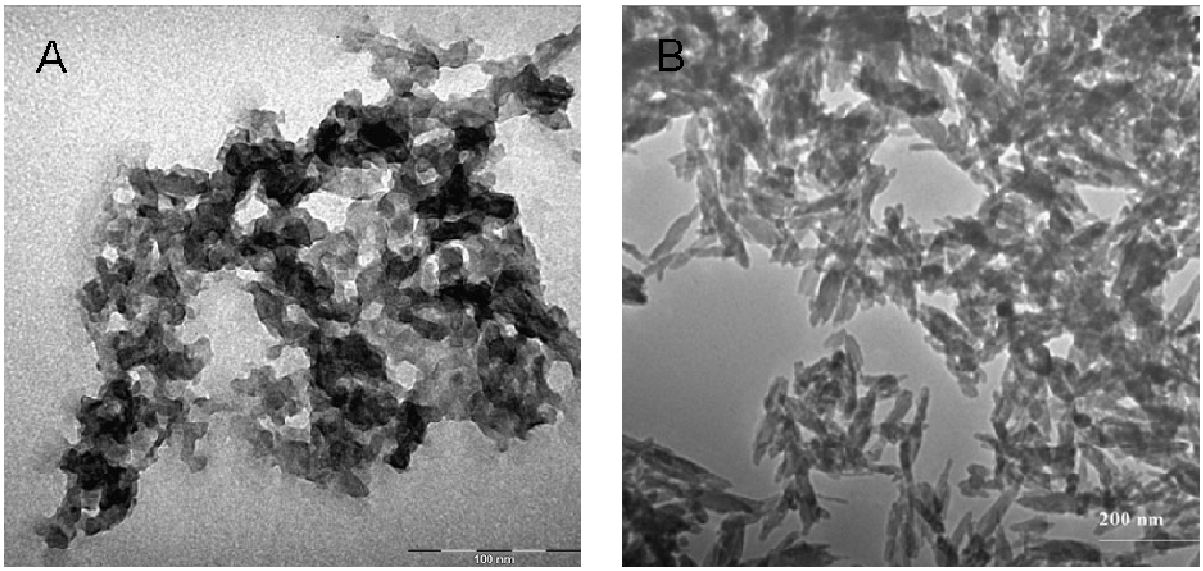

Figure 3.3 TEM images of synthetic HA nanocrystals with A) plate-shaped morphology (HAps) (scale bar = 100 nm), and B) needle-shaped morphology (HAns) (scale bar = 200 nm).

Powder X-ray diffraction (XRD) patterns of HAps and HAns (Figure 3.4a and b, respectively) showed characteristic diffraction maxima of a synthesized hydroxyapatite single phase (JCPDS 9-432). The broadening of the diffraction maxima indicated a relatively low degree of crystallinity, which was quantified according to previous methods (Table 3.1). The crystal domain sizes along the c direction were calculated by Scherrer's formula using the 2θ = 26° (002) diffraction peak, and were 350 and 230 Å for HAns and HAps, respectively. The HAps diffraction pattern was very similar to that recorded for deproteinated bone apatite (Figure 3.4), and this was quantitatively confirmed by the similarity of the two crystal domain sizes (230 and 213 Å, respectively).

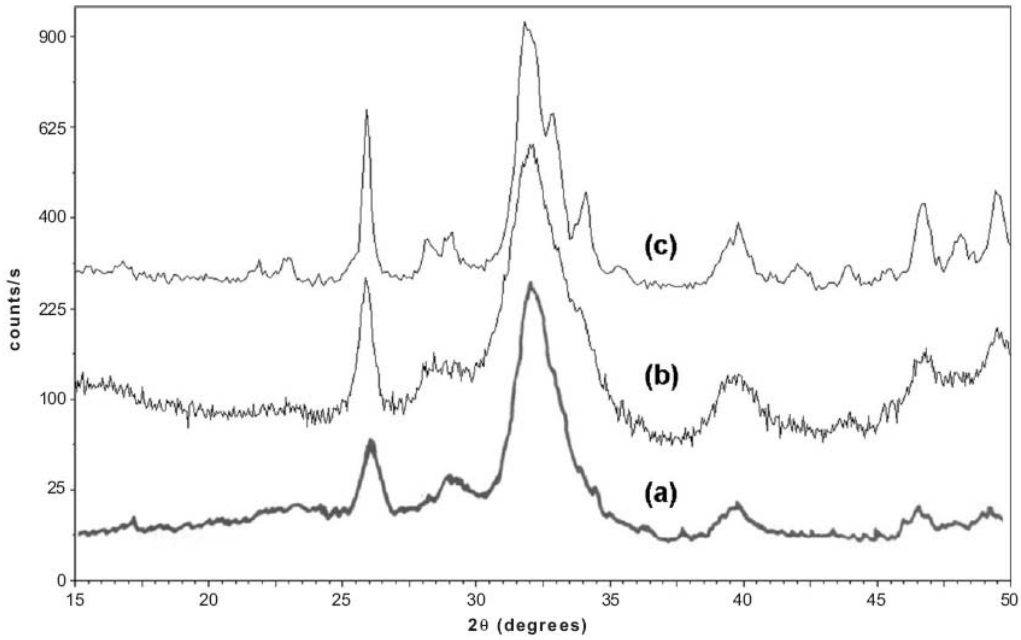

Figure 3.4 XRD patterns of a) bone HA, b) HAps, and c) HAns.

3.3 ADSORPTION OF DRUG MOLECULES BY HA NANOCRYSTALS

The above differences in morphological and surface properties of the HAps and HAns nanocrystals were investigated with respect to the adsorption and release of various drug molecules.

An aliquot (1.5 mL) of cisplatin, di(ethylenediamineplatinum) (DPM) or alendronate dissolved in ultrapure water (10^{-3} M, 0.4 $mgmL^{-1}$ cisplatin, 0.8 $mgmL^{-1}$ DPM, 0.4 $mgmL^{-1}$ alendronate; cisplatin and DPM solutions required sonication for 15 and 30 min, respectively) was added to 10 mg of HA nanocrystals in a conical polyethylene Eppendorf tube having a capacity of 2 mL. After 15 s of treatment in a vortex apparatus, the HA suspension was maintained in a bascule bath at 37 °C. Adsorption profiles for the platinum complexes and alendronate were determined by measuring the concentration of drug remaining in the supernatant solution with time. At scheduled times,

aliquots (100 μL) of the supernatant that was well separated from the solid phase by 3 min centrifugation at 11 000 rpm on a Micro Centrifugette 4214 were removed for drug quantification and replaced with fresh water. The concentrations of cisplatin and DPM were determined by spectrophotometric and platinum ICP-OES analysis; alendronate concentrations were determined by colorimetric method. Solution concentrations of cisplatin and DPM were determined by UV-vis spectrophotometric analysis. The UV-Vis spectra were recorded between 190 and 300 nm using a Varian Cary 5 UV-Vis-nearIR spectrophotometer, and the absorbance was measured at 205 and 230 nm against reagent blanks for cisplatin and DPM, respectively. Alendronate concentrations were measured by a colorimetric method based on the reaction of the primary amino group with ninhydrin in methanolic medium in the presence of 0.05 $molL^{-1}$ sodium bicarbonate. The colored product was measured at 568 nm against the reagent blank (Taha *et al.*, 2003). Phosphorous contents were determined spectrophotometrically as molybdovanadophosphoric acid using 1 cm quartz cell (Quinlan *et al.*, 1955).

The adsorption profiles of cisplatin (CDDP), alendronate, and di(ethylenediamineplatinum)medronate (DPM) in the presence of HAps or HAns nanocrystals are shown in figure 3.5.

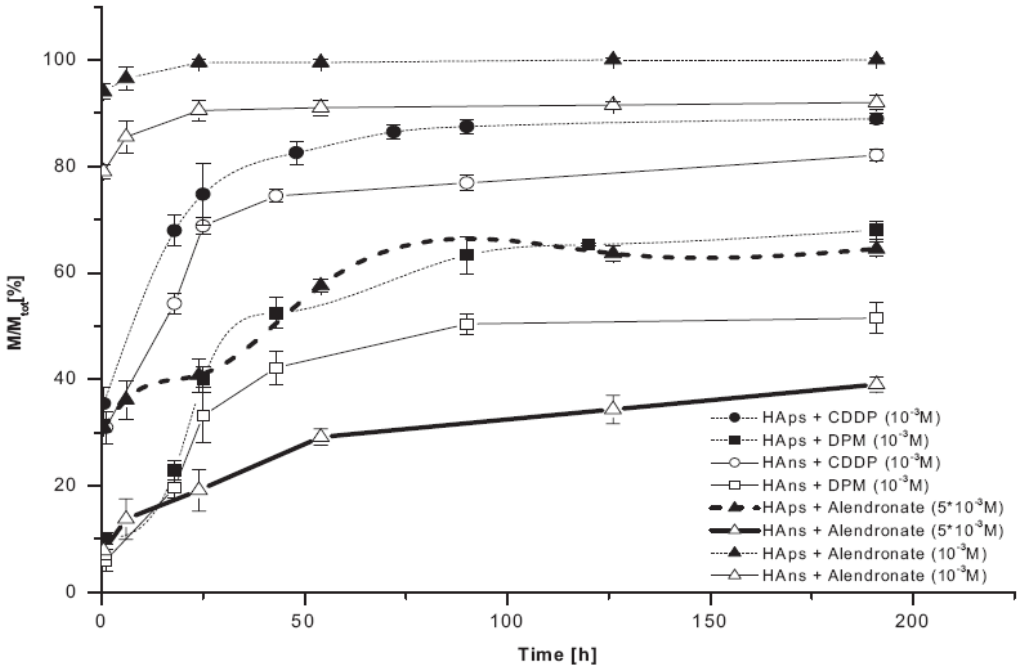

Figure 3.5 Adsorbed mass percentages from 10^{-3} M solutions of cisplatin (CDDP, circles), DPM (squares), or alendronate (triangles), and from a 4.6×10^{-3} M solution of alendronate (thick lines) as a function of time for plate-shaped (full symbols) and needle-shaped (empty symbols) HA nanocrystals. Cisplatin and DPM concentrations were determined by ICP-OES analyses, alendronate concentrations by UV-vis spectroscopy.

The plots show that the maximum uptake of cisplatin or DPM was reached after about 190 h for both types of HA nanocrystals, whilst the uptake of alendronate was significantly faster reaching a maximum value after about 24 h. In each case, slightly higher drug affinities were observed in the presence of HAps nanocrystals compared with HAns particles. Typically, the percentage of drug adsorbed onto the HAps nanoparticles with respect to the initial drug concentration was 100, 89, and 68% for alendronate, cisplatin, and DPM, respectively, which corresponded to a HA loading level of 5.6, 5.8, and 7.6 wt% of adsorbed drug (100 $=W_{\text{drug-loaded HA}}$).

In contrast, the drug percentage adsorbed onto HAns was 92%, 82%, and 52%, for alendronate, cisplatin, and DPM, respectively (corresponding to HA loading levels of 5.2%, 5.4%, and 6.3%). The higher level of alendronate affinity for HAps rather than HAns nanoparticles was more pronounced in concentrated alendronate solutions (4.6×10^{-3} M), where the percentage of drug adsorbed onto HAps and HAns was 64% and 39% (corresponding to 12.6% and 7.9% loading levels), respectively.

Although for both HAps and HAns nanocrystals, the bulk Ca/P ratios were very similar for both the drug-loaded and the unloaded materials (ICP analysis), the surface Ca/P ratios determined by XPS analyses were decreased for the HA–drug conjugates compared to the unloaded HA nanocrystals, consistent with adsorption of the drug molecules specifically onto the nanocrystal surfaces. The decrease in Ca/P ratio between a 5.6% alendronate-loaded HAps conjugate and an unloaded HAps sample was 0.34% (1.11 and 1.45, respectively), which were greater than the corresponding value of 0.19% observed for 5.2% alendronate-loaded HAns and unloaded HAns (1.11 and 1.30, respectively). A similar trend was observed for the DPM-loaded HA samples, which showed Ca/P ratios of 1.15 and 1.45 for DPM-loaded HAps (7.6%) and unloaded HAps, compared with corresponding ratios of 1.26 and 1.30 for DPM-loaded (6.3%) HAns and unloaded HAns. Significantly, no appreciable release of phosphate from the HA nanocrystals surfaces was observed during cisplatin or DPM adsorption. In contrast, 2–0.5 phosphate moles were released for every mole of alendronate adsorbed onto the HA nanoparticles, suggesting that this process occurred by ligand exchange of two surface phosphate anions with two phosphonate groups of the adsorbed drug molecule.

Binding of the phosphonate groups of alendronate onto the HA nanoparticles was investigated by analysis of the spectral features of the O *1s* and P *2p* XPS peaks (Figure 3.6). An intense band at 530.68 eV was observed for the alendronate-loaded HAns conjugate (Figure 3.6c), which was considered as a convolution of the alendronate band at 530.37 eV (Figure 3.6b), the HAns band at 531.36 eV (Figure 3.5a), and significantly, a band at 531.68 eV originating from alendronate molecules adsorbed onto the HA surface. The P region of the alendronate-loaded HA XPS spectra

(data not shown) indicated that the binding energy observed at 133.0 eV was due to the presence of both the HAns phosphate (133.5 eV) and alendronate phosphonate (132.3 eV).
XPS analyses were also undertaken on cisplatin-loaded HA samples. The Pt/N ratios were 0.50–0.05 and 0.60–0.05 for cisplatin-loaded HAns and HAps, respectively.

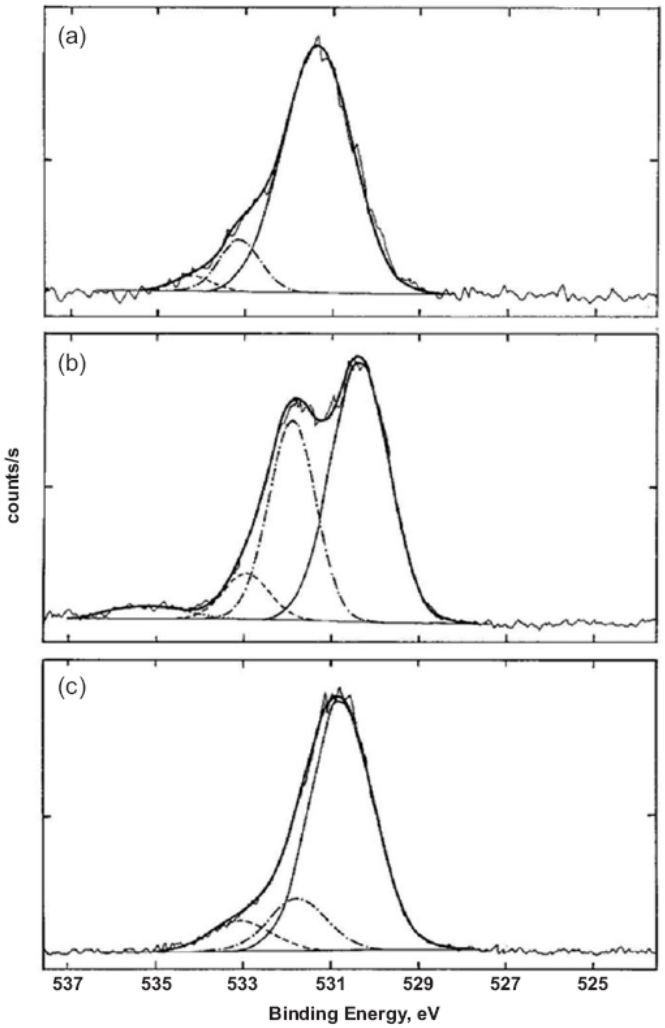

Figure 3.6 Oxygen *1s* spectral region obtained for a) HAns, b) unbound alendronate and c) alendronate-loaded HAns. Dotted lines were used for curve fitting and full lines for experimental peaks.

These data were close to the stoichiometric values for cisplatin, revealing that the platinum complex does not undergo Pt–N bond degradation during adsorption onto the HA nanocrystals. On the other hand, no chlorine was detected by XPS analyses, clearly indicating that cisplatin undergoes hydrolysis before deposition onto the HA surface.[14,15] The oxygen region of the spectrum showed three peaks at 531.0, 533.1 and 534.1 eV, and as cisplatin alone has no oxygen signature (spectrum not shown), the decrease of the first oxygen-peak binding energy from a value of 531.36

eV in the unmodified HAns, was attributed to strong interactions between cisplatin and the HA surface. The same behaviour was observed for the P peak at 133.0 eV, which was 0.5 eV lower than that observed for pure HA. Similar XPS results were obtained for DPM-loaded HA conjugates. The Pt/N ratios were 0.40–0.050 and 0.60–0.05 for DPM-loaded HAns and HAps materials, respectively. These values were close to those for free DPM indicating that, like cisplatin, no Pt–N bond degradation occurred during surface adsorption. However, the P *2p* binding energy for the DPM loaded HA nanocrystals was 132.8 eV, which was lower than those observed for pure HA and cisplatin-loaded HA, indicating that the interaction between HA and DPM was stronger than that observed for cisplatin.

Adsorption phenomena depend on the physicochemical properties of the drugs and of the HA nanoparticles used. Adsorption is favoured for alendronate and cisplatin, and less so for DPM. For cisplatin, XPS analysis reveals the absence of chlorine, indicating hydrolysis, probably to a positively charged aqua species prior to surface adsorption, in agreement with previous studies (Barroug *et al.*, 2002). DPM can also undergo partial hydrolysis in solution but this takes place without complete displacement of the medronate group, so that overall the molecule remains neutral. Thus difference in charge of the hydrolyzed cisplatin and DPM complexes could account for the observed adsorption curves, particularly as the HA surface has a net-negative charge. The high adsorption of alendronate, however, despite its negative charge, suggests a different adsorption mechanism, and as two moles of phosphate are released per mole of adsorbed alendronate, the results suggest that adsorption of the bisphosphonate proceeds via ligand exchange. Indeed, it seems feasible that the ligand exchange mechanism of alendronate adsorption might also be facilitated by electrostatic interactions between the cationic aminopropyl side chain and negatively charged HA surface, which is consistent with recent studies by Nancollas et al. (Nancollas *et al.*, 2006).

For the three bioactive molecules investigated, the adsorption phenomena are also expected to be affected by the physicochemical properties and morphological characteristics of the two types of synthetic HA nanocrystals used as adsorbent substrates. One such parameter affecting the drug binding is HA surface area, and in order to aid evaluation of the influence of degree of HA crystallinity and surface composition, normalization of the adsorption profiles with respect to surface area is shown in figure 3.7.

The normalized adsorption curves for HAps and HAns are almost coincident for DPM adsorption (t values give a confidence interval of 90 %), indicating that apart from the surface area, other physicochemical properties of the different HAs do not strongly affect the adsorption of this molecule at low concentrations. In contrast, normalized cisplatin and alendronate adsorption curves are close but not coincident for the two HAs, showing a slightly greater amount of adsorbed drug in

the case of HAns as compared to HAps. As HAns has a lower surface Ca/P ratio than HAps, the surface charge is more negative, and this will favour adsorption of positively charged hydrolysis products of cisplatin and easier exchange of phosphate anions with alendronate phosphate groups.

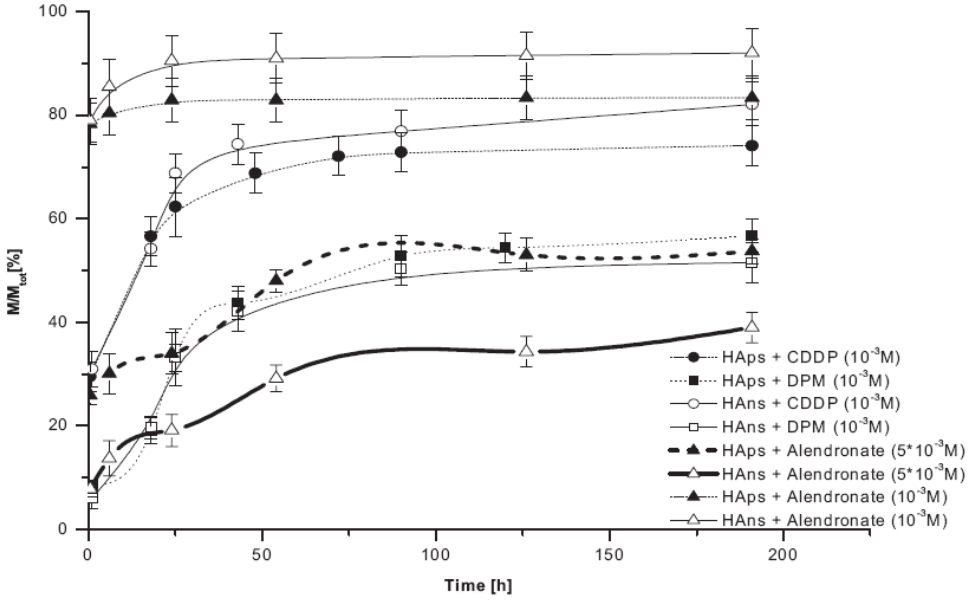

Figure 3.7 Adsorbed mass percentages normalized with respect to HA surface areas for 10^{-3} M solutions of cisplatin (CDDM, circles), DPM (squares), and alendronate (triangles), and for 4.6×10^{-3} M solutions of alendronate (marked triangles) as a function of time for plate-shaped (full symbols) and needle-shaped (empty symbols) HA nanoparticles.

The difference in surface Ca/P ratios also appears to influence the adsorption of alendronate from more concentrated solutions (4.6×10^{-3} M) as the normalized profile for HAns falls below that for HAps under these conditions. This could be as a result of the higher surface Ca/P ratio of the latter that favours adsorption of alendronate, which has high affinity for calcium. Thus, in more concentrated solutions, where HA binding sites are probably saturated, alendronate adsorption appears to be modulated by the surface Ca/P ratios, with increased adsorption on calcium-rich surfaces. In contrast, positively charged cisplatin adsorption is greater on phosphate-richer surface, and adsorption of neutral DPM molecules is not appreciably affected by differences in Ca/P ratios of the HA surfaces.

3.4 DRUG RELEASE PROFILES

The release kinetics of alendronate, cisplatin, and DPM from HAps and HAns as a function of contact time in aqueous solution are plotted in Figure 3.8. UV-Vis spectroscopic analysis indicated

that the aqueous species released from cisplatin- or DPM-loaded HA nanoparticles had an adsorption peak maximum at 226 nm, which was not present in the blank solution (HEPES buffer). This band differed from the adsorption bands characteristic of the two platinum complexes, but nevertheless was ascribed to the release of the same platinum complex as confirmed by ICP-optical emission spectroscopy (OES) determinations (see materials and methods). The amount of drug released from cisplatin- or alendronate-loaded HAns was, 45 and 21% of the amount adsorbed, respectively, which were slightly lower than the corresponding values determined for cisplatinand alendronate-loaded HAps samples (55 and 33 %, respectively). In the case of DPM-loaded HA nanoparticles, the release was faster and nearly quantitative, reaching equilibrium concentrations of 85 and 100% for HAns and HAps, respectively.

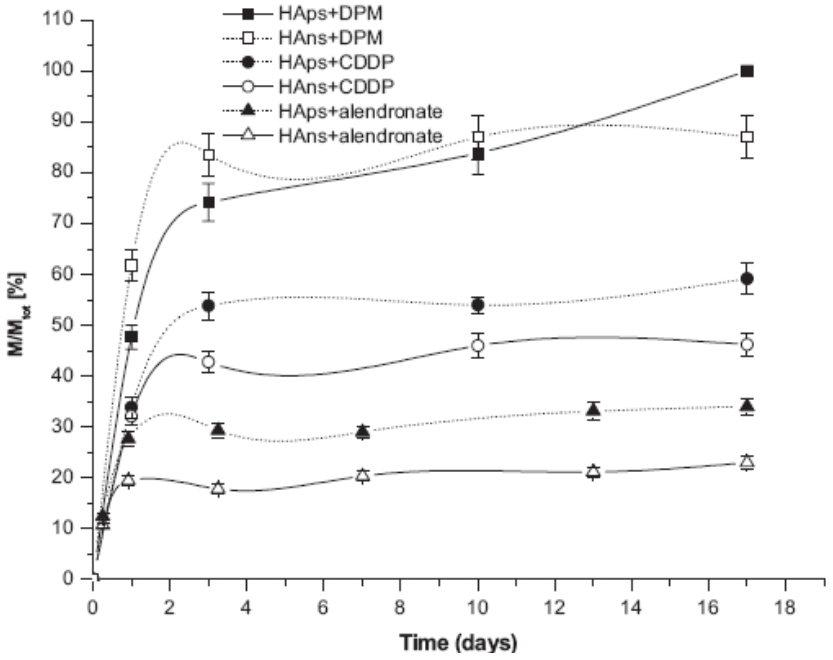

Figure 3.8 Released mass percentages of cisplatin (CDDP, circles), DPM (squares), and alendronate (triangles) as a function of time for plateshaped (full symbols) and needle-shaped (empty symbols) HA nanoparticles.

The release profiles of the drug molecules from the HA nanoparticles surfaces follow a different trend (DPM> cisplatin > alendronate) when compared with the adsorption process. UV analysis shows that the released species is the same for cisplatin and for DPM-loaded HAs, indicating that release of platinum from the latter probably occurs through complete breakage of the platinum–medronate bond. Therefore, the desorption process can be expected to be quite fast for DPM; slower for cisplatin, as the positively charged hydrolyzed cisplatin is linked quite strongly by electrostatic interactions to the negatively charged HA surface; and very slow for alendronate

because of strong electrostatic interactions between the bisphosphonate groups and surface Ca^{2+} ions. We applied the diffusion-based model described by Higuchi (Higuchi, 1963) to our release profiles (data not shown) but were unable to fit the experimental data, suggesting a nondiffusive mechanism for the systems under investigation. Normalized plots of the release profiles are almost coincident for cisplatin and alendronate (Figure 3.9), indicating that desorption of these charged drugs is not affected by the nanocrystal surface composition (Ca/P ratio) but only by surface area.
In contrast, surface-normalized DPM-desorption curves reveal an increase in the amount of desorbed drug in the case of HAns as compared to HAps nanoparticles. If we assume that the release of this molecule occurs through complete cleavage of the Pt-phosphonate bond, we expect that this process will depend on a physicochemical property such as differences in the surface stoichiometry (Ca/P ratio) of the HA nanoparticles surfaces.

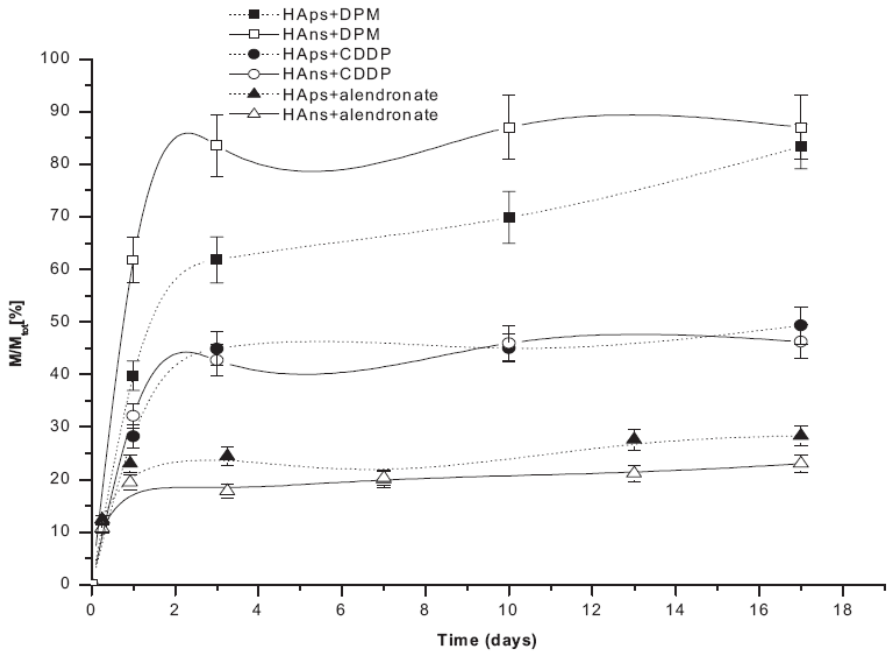

Figure 3.9 Released mass percentages normalized with respect to the HA surface areas of cisplatin (CDDP, circles), DPM (squares), and alendronate (triangles) as a function of time for plate-shaped (full symbols) and needle-shaped (empty symbols) HA nanoparticles.

3.5 CONCLUSIONS

The in vitro adsorption and desorption of cisplatin, DPM, and alendronate towards needle-shaped or plate-shaped HA nanocrystals have been investigated. The HA surface area and surface charge (Ca/P ratio), as well as the charge on the adsorbed molecules and their mode of interaction with the HA surface, influence the adsorption and release kinetics of the three drugs investigated.

Electrostatic binding of a cationic species of hydrolyzed cisplatin species to the negatively charged HA surface is greatly favoured over the adsorption of uncharged DPM. On the other hand, binding of negatively charged alendronate to the HA nanoparticles surface is not curtailed because ligand exchange between the bisphosphonates group and two surface phosphate anions promotes strong adsorption. The above processes are modulated to some extent by the surface composition; for example, HAps nanoparticles having a higher Ca/P ratio favour adsorption of negatively charged alendronate compared with the HAns nanocrystals. This effect, however, is evident only at high concentrations, where the HA binding sites are probably saturated. On the other hand, HAns nanoparticles having a lower Ca/P ratio slightly favour adsorption of positively charged species of hydrolyzed cisplatin. With regard to the release kinetics, neutral DPM is released in preference to positively charged aquated cisplatin and negatively charged alendronate. It is possible that short range electrostatic interactions between aquated cisplatin and surface phosphates, and complexation between anionic alendronate and surface Ca^{2+} ions, disfavour release of these drugs. Moreover, it appears that release of DPM takes place through complete cleavage of the platinum–medronate bond. Finally, whilst desorption of charged species (aquated cisplatin or anionic alendronate) is not dependent on the type of HA nanoparticle used, the release of neutral DPM molecules is greater when adsorbed to HAns rather than for HAps nanocrystals. The above results demonstrated that HA nanocrystals and antitumor drugs can be selected in such a way that the bioactivity of the drug–HA conjugate could be tailored for specific therapeutic applications.

REFERENCES

- Aoki, H.; Kato, K.; Ogiso, M.; Tabata, T. *Biomater., Med. Devices, Artif. Organs* **1979**, *7*, 291.
- Barroug, A.; Glimcher, M. J. *J. Orthop. Res.* **2002**, *20*, 274.
- Barroug, A.; Kuhn, L. T.; Gerstenfeld, L. C.; Glimcher, M. J. *J. Orthop. Res.* **2004**, *22*, 703.
- Barroug, A.; Lernous, E.; Lemaitre, J.; Rouxhet, P. G. *J. Colloid. Interf. Sci.* **1998**, *208*, 147.
- Bloemink, M. J.; Keppler, B. K.; Zahn, H.; Dorenbos, J. P.; Heetebrij, R. J.; Reedijk, J. *Inorg. Chem.* **1994**, *33*, 1127.
- Brunauer, S. P.; Emmet, P. H.; Teller, E. *J. Am. Chem. Soc.* **1938**, *60*, 309.
- De Wall, W. A. J.; Maessen, F. J. M. J.; Kraak, J. C. *J. Pharm. Biomed Anal.* **1990**, 1, 1.
- Erkmen, Z. E. *J. Biomed. Mater. Res.* **1999**, *48*, 861.
- Ezra, A. Golomb, G. *Adv. Drug Delivery Rev.* **2000**, *42*, 175.
- Ferraz, M. P.; Monteiro, F. J.; Manuel, C. M. *J. Appl. Biomater. Biomech.* **2004**, *2*, 74.

- Guaber, S. P. A.; Gazzaniga, G.; Roveri, N.; Rimondini, L.; Palazzo, B.; Iafisco, M.; Gualandi, P. EU Patent 005 146, 2006.
- Guicheux, J.; Grimandi, G.; Trecant, M.; Faivre, A.; Takahashi, S.; Daculsi, G. *J. Biomed. Mater. Res.* **1997**, *34*, 165.
- Highuchi, T. *J. Pharm. Sci.* **1963**, *52*, 1145.
- Josse, S.; Faucheux, C.; Soueidan, A.; Grimandi, G.; Massiot, D.; Alonso, B.; Janvier, P.; Laib, S.; Pilet, P.; Gauthier, O.; Daculsi, G.; Guicheux, J.; Bujoli, B.; Bouler, J. M. *Biomaterials* **2004**, *26*, 2073.
- Kelman, A. D.; Peresie, H. J. *Cancer Treat. Rep.* **1979**, *63*, 1445.
- Klenner, T.; Valenzuela-Paz, P.; Amelung, F.; Muench, H.; Zahn, H.; Keppler, B. K.; Blum, H. *Met. Complexes Cancer Chemother.* **1993**, *95*.
- Klenner, T.; Valenzuela-Paz, P.; Keppler, B. K.; Angres, G.; Scherf, H. R.; Wingen, F.; Amelung, F.; Schmahl, D. *Cancer Treatment Rev.* **1990**, *17*, 253.
- Klenner, T.; Wingen, F.; Keppler, B. K.; Krempien, B.; Schmahl, D. *J. Cancer Res. Clin. Onc.* **1990**, *116*, 341.
- Landi, E.; Tampieri, A.; Celotti, G.; Sprio, S.; *J. Eur. Ceram. Soc.* **2000**, *20*, 2377.
- Lebugle, A.; Rodrigues, A.; Bonnevialle, P.; Voigt, J. J.; Canal, P.; Rodriguez, F. *Biomaterials* **2002**, *23*, 3517.
- Lin, J.*Bone* **1996**, *18*, 75.
- Liou, S. C. , Chen, S. Y. , Lee, H. Y.; Bo, J. S. *Biomaterials* **2004**, *25*, 189.
- Miura, S.; Mii, Y.; Miyauchi, Y.; Ohgushi, H.; Morishita, T.; Hohnoki, K.; Aoki, M.; Tamai, S.; Konishi, Y. *Jpn. J. Clin. Oncol.* **1995**, *25*, 61.
- Nancollas, G. H.; Tang, R.; Phipps, R. J.; Henneman, Z.; Gulde, S.; Wu, W.; Mangood, A.; Russell, R. G. G.; Ebetino, F. H. *Bone* **2006**, *38*, 617.
- Palazzo, B.; Iafisco, M.; Laforgia, M.; Margiotta, N.; Natile, G.; Bianchi, C. L.; Walsh, D.; Mann, S.; Roveri, N. *Adv. Funct. Mater.* **2007**, *17*, 2180.
- Palazzo, B.; Roveri, N.; Sidoti, M. C.; Tampieri, A.; Sandri, M.; Bertolazzi, L.; Galbusera, F.; Dubini, G.; Vena, P.; Contro, R. *Mater. Sci. Eng. C* **2005**, *25*, 207.
- Quinlan, K. P.; De Sesa, M. A. *Anal. Chem.* **1955**, *27*, 61.
- Rodriguez-Lorenzo, L. M.; Vallet-Regi, M.; Ferreira, J. M. F.; *Biomaterials* **2001**, *22*, 1847.
- Rosenberg, B. *Cancer Treat. Rep.* **1979**, *63*, 1433.
- Roussiere, H.; Montavon, G.; Laib, S.; Janvier, P.; Alonso, B.; Fayon, F.; Petit, M.; Massiot, D.; Bouler, J. M.; Bujoli, B. *J. Mater. Chem.* **2005**, *15*, 3869.

- Russell, R. G. G.; Rogers, M. J. *Bone* **1999**, *25*, 97.
- Segal, E.; Le Pecq, J. B. *Cancer Res.* **1985**, *45*, 492.
- Taha, E. A.; Youssef, N. F. *Chem. Pharm. Bull.* **2003**, *51*, 1444.
- Tahara, Y.; Ishii, Y. *J. Orthop. Sci.* **2001**, *6*, 556.
- Uchida, A.; Shinto, Y.; Araki, N.; Ono, K. *J. Orthop. Res.* **1992**, *10*, 440.
- Wingen, F. Schmahl, D.*Drug Res.* **1985**, *35*, 1565.
- Yotsuyanagi, T.; Usami, M.; Noda, Y.; Nagata, M. *Int. J. Pharm.* **2002**, *246*, 95.
- Yuan, H.;. De Groot, K In *Learning From Nature: How To Design New Implantable Biomaterials*, NATO Science Series, Kluwer, Dordrecht, The Netherlands 2004.
- Zwelling, L. A.; Kohn, K. W. *Cancer Treat. Rep.* **1979**, *63*, 1439.

CHAPTER 4
INTERACTION OF HYDROXYAPATITE NANOCRYSTALS WITH PROTEINS

4.1 STATUS OF THE ART

The interaction of proteins with solid inorganic surfaces is not only a fundamental phenomenon but is also the key to several important and novel applications. In the biomaterials field, protein-surface adhesion is the first event in the integration of an implanted device or material with biological tissues. In nanotechnology, protein-surface interactions are pivotal for the assembly of interfacial protein constructs, such as sensors, activators, and other functional components at the biological/electronic junction. The detailed mechanistic understanding of the protein-surface interaction and the ability to tailor protein surface interaction in nanosized materials would be of value to bionanoassembly technologies. The study of protein-solid surface interaction, which involves both protein binding and unfolding, may also increase our general knowledge of protein biophysics (Gray, 2004).

The exposure of biomaterials to plasma proteins, blood, or biological fluids normally leads to the adsorption of blood proteins onto the biomaterials surface. The adsorbed protein layer can further mediate additional biological responses, such as cell attachment and activation, and can create unpredicted perturbations to device operation (Bajpai, 2005). Although protein adsorption on solid surfaces has been widely studied for decades, its mechanisms are still far from being fully understood. This is because the adsorption of protein on solid surface is a complicated process consisting of many events, such as conformational changes in protein molecules and the coadsorption of ions. In particular, the protein conformational change, which results in entropic gain, is thought to be an important driving forces for the protein surface adsorption (Kondo *et al.*, 1996). However, the most important forces involved in the molecular adsorption can be expected to be electrostatic, which are associated with exposed charged groups on the protein surface.

In the biomaterial field, calcium phosphates, which are the inorganic components of bone, are widely used as bone grafts. Here, a knowledge of the underlying principles of protein interaction with calcium phosphates is required not only in evaluating their potential application but also in their ability to act as carriers for enzymes.

The effective immobilization of enzymes on solid substrates without changing the original conformation and bioactivity has attracted increasing interest among researchers along with rapid advances of biotechnology and biodevices (Lu *et al.*, 2006; Bellezza *et al.*, 2006; Bellezza *et al.*, 2004). Spectroscopists have investigated heme proteins by means of resonance Raman technique, in which the Raman effect is enhanced by the coupling of vibrational and electronic transitions. This

technique uses visible and UV excitation sources that enhance vibration of the porphyrin ring and allow studying the stereochemistry and electronic properties of heme (Kitagawa *et al.*, 1978; Spiro *et al.*, 1979).

Myoglobin is probably the most investigated protein in the construction of enzymes that catalyze desired and often nonnatural reactions, achieving predictable substrate specificity, and is one of the objectives of applied biotechnology (Roncone *et al.*, 2005).

Myoglobin (Mb) can be considered to be a model protein because of its well-known structure and properties, commercial availability, and relatively small size. Myoglobin is a globular heme protein with a molecular mass of 17 800 Da, an isoelectric point (pI) of 7.4, and approximate dimensions of $2.5 \times 3.5 \times 4.5$ nm^3. It is found in cardiac and red skeletal muscle tissues, where it acts as an oxygen storage and transporting protein. It contains a single polypeptide chain of 153 amino acid residues and an iron porphyrin IX complex as the prosthetic group (Roat-Malone, 2002).

It is well known that hydroxyapatite shows high affinity for proteins (Iafisco *et al.*, 2008) and much attention has been focused on hydroxyapatite and substituted hydroxyapatite nanocrystals as sorbents for removing pathogenic proteins from blood, for blood purification therapy (Takemoto *et al.*, 2004; Fujii *et al.*, 2006) and as carrier for protein delivery (Paul *et al.*, 1999; Liu *et al.*, 2005).

Human serum albumin (HSA) is the most abundant protein in blood plasma and serves as a transport protein for many endogenous and exogenous compounds (Peters, 1996). Albumins from different mammalian species show many similarities in their physico-chemical properties (Peters, 1985; Carter *et al.*, 1994). There are 332 (57%) invariant residues in the sequences of mammalian albumins. 76% of sequence identities have been noted between bovine (BSA) and human albumin. These two albumins are indistinguishable in term of some physical criteria and appear quite similar in term of surface hydrophobicity and partitioning behaviour in some aqueous two-phase system (Tubio *et al.*, 2004). On the other hand, serious differences in electrophoretic behaviour (Miller *et al.*, 1993), thermal and chemical stability (Kosa *et al.*, 1998), binding and photochemical properties (Kosa *et al.*, 1998; Tayyab *et al.*, 2003) exist between different mammalian albumins.

Hydroxyapatite is also known for its binding capability to a wide variety of molecules (HA is nowadays widely applied for separation of various proteins in a high performance liquid chromatograph system) (Kandori *et al.*, 2000; Akawa *et al.*, 1999). Moreover, most therapeutic agents intended for bone diseases have a particular affinity to bone hydroxyapatite under physiological conditions (Xu *et al.*, 2007). A class of molecules known as bisphosphonates (BPs) exhibit a strong affinity to bone mineral under physiological conditions. This because BPs are characterized by two phosphonate groups attached to a single carbon atom and have strong affinity for the Ca^{2+} ions of bone apatite. This property is the basis for their use as inhibitors of ectopic

calcification and of bone resorption. In fact, calcium deficient synthetic apatites has been investigated as devices for the controlled delivery of geminal bisphosphonates (Palazzo *et al.*, 2007). Chemical surface binding of bisphosphonates to hydroxyapatite could represent an effective means to impart it finetuned bioactivity (Wright *et al.*, 2006). Hydroxyapatite, which is insoluble and nonreactive with many biochemical compounds, could be an elective material for supporting immobilized proteins, which can interact properly with the charged groups on the HA surface.

4.2 AIM OF THE WORK

The aim of this work is organized in two point The first aim is to compare myoglobin affinity versus the BPs surface functionalization of biomimetic HA in respect to unfunctionalized hydroxyapatite. Moreover, using by UV-vis and SERS (surface-enhanced raman spectroscopy) spectroscopic techniques, it has been pointed out that the apatitic nanostructured biomimetic substrate affects the conformation of the protein. The Mb analysis recognizing and assembling on drug-loaded apatite crystals not only allows a better understanding of the protein adhesion mechanism but could also aid in the development of surface coatings to improve the biocompatibility of bone-implantable biomaterials and for hard-tissue engineering and regeneration technologies.

The second aim of this is to point out surface recognition of human and bovine serum albumin by two different carbonate-hydroxyapatites. The synthetic nanocrystals have different dimensions, surface areas, crystallinity and surface properties. In particular, by using FT-IR and spectroscopic technique it has been highlighted that the apatitic biomimetic substrate affects the protein conformations.

This study could improve the understanding of enzyme immobilization in the field of biomaterials science, in particular, to fine tune a bone-specific drug/protein delivery device, and to test HA as a new support for heterogeneous catalysis.

4.3 INTERACTION OF MYOGLOBIN WITH HYDROXYAPATITE

HA nanocrystals with a nearly stoichiometric Ca/P ratio (1.67) were synthesized in order to produce a plate-shaped bonelike apatite phase. The powder fraction of nanocrystals having granular dimensions ranging from 100 to 150 μm was selected for this study. The surface Ca/P ratio determined by X-ray photoemission spectroscopy (XPS) analysis was significantly lower (1.45) as a result of surface disorder (Jager *et al.*, 2006). Specific surface area measurement was undertaken by

using a Carlo Erba Sorpty 1750 instrument by measuring N_2 adsorption at 77 K and adopting the well-known BET procedure (Brunauer *et al.*, 1938). The specific surface area of HA was 120 ± 6 m^2/g. Details of its synthesis, as well as the other physicochemical properties, are reported elsewhere (Palazzo *et al.*, 2007).

Samples of adsorbed Mb were prepared by mixing 10 mg of HA with 1.5 mL of protein dissolved in Hepes buffer (0.01 M Hepes, 0.5 M NaCl) at pH 7.4 at different concentrations (ranging from 0.2 to 2 mg/mL) in a 2 mL conical polyethylene Eppendorf tube. The mixture was maintained in a bascule bath at 37 °C for 24 h. The solid, for the Raman spectroscopic investigation, was recovered by centrifuging at 12675g for 3 min and then freeze drying at -60 °C under vacuum (3 mbar) for 12 h. The supernatant solution was assayed for protein content by UV spectroscopy (λ = 409 nm, ε = 188000 M^{-1} cm^{-1}). The amount of adsorbed protein was calculated from the difference between the concentrations of the initial solution and the supernatant. The UV-Vis spectra of Mb solutions were recorded between 200 and 800 nm using a Varian Cary 5 UV-vis-NIR spectrophotometer (Varian, Palo Alto, CA) against a blank buffer solution. The measurements were performed using a 1 cm quartz cell.

The adsorption data were fitted to the Langmuir (1) and Freundlich (2) equations23,24

$$Q_e = \frac{Q_{\max} C_e}{\left(\frac{1}{\alpha_L}\right) + C_e} \quad (1)$$

$$Q_e = K_F C_e^{1/n} \quad (2)$$

where C_e is the concentration of Mb in solution at equilibrium (mg/mL), Q_e is the amount of Mb adsorbed onto the support (mg/g of support), Q_{max} is the maximum adsorption capacity of the support (mg/g of support), α_L is the Langmuir constant (mL/mg), K_F is the Freundlich adsorption coefficient ((mg/g of support)/$(mg/mL)^{-1/n}$), and 1/n is the heterogeneity factor (a-dimensional).

The results of myoglobin adsorption onto HA are reported as an isotherm in figure 4.1, where the adsorbed amount, Γ_{Mb} (mg/m^2), is plotted against the protein concentration after adsorption, $C_{myoglobin}$ (mg/mL). The plot is characterized by an initial slope indicating high protein affinity for the HA surface. The adsorption saturation yields a plateau value corresponding to the maximum amount of Mb surface immobilization of about 0.7 mg/m2. This finding is in agreement with the data reported by Kandori et al. (Kandori *et al.*, 2000). They observed a Mb adsorption limit on different carbonate-hydroxyapatite particles in the range of 0.65-0.82 mg/m2. The increase in Mb concentration in the buffer solution increases the surface coverage, until completion takes place using a Mb starting concentration higher than 2 mg/mL onto 10 mg of HA. The solubility limit of myoglobin under these experimental conditions avoids the investigation of more concentrated

solutions. When the plateau value is reached in the adsorption isotherm, probably a monolayer of Mb molecules has been deposited.

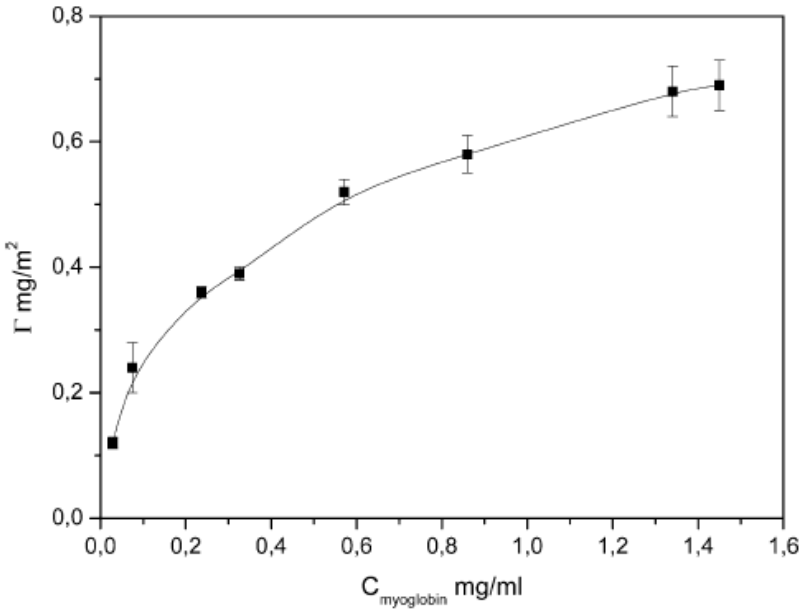

Figure 4.1 Adsorption isotherm of myoglobin on biomimetic hydroxyapatite nanocrystals at pH 7.4

Both the Langmuir and the Freundlich models have been utilized to describe the Mb adsorption isotherm. The values of the Langmuir and Freundlich constants calculated by linear fitting for Mb immobilization onto the HA surface are compared in table 4.1, revealing that both models can well describe the Mb monolayer on HA.

Table 4.1 Adsorption parameters of myoglobin onto biomimetic hydroxyapatite nanocrystals calculated according to Langmuir and Freudlinch models

	Langmuir			Freudlinch		
	Q_{MAX} (mg/g of support)	a_L (mL/mg)	r^2	K_F (mg/g of support)/(mg/mL)$^{-1/n}$)	1/n	r^2
Mb/HA	610	8.06	0.994	75	0.42	0.989

Probably the two models represent a simplification of the real adsorption systems, which would be a combination of both. In fact, the Langmuir isotherm assumes an energetically homogeneous support surface with identical adsorption sites throughout. Therefore, these sites are expected to hold equal numbers of Mb molecules, and a monolayer is formed. Moreover, the Langmuir formula implies highly favourable and irreversible adsorption. The calculated Q_{max} value (maximum adsorption capacity of the support) of 76 mg/g is higher than that (35 mg/g) reported by Bellezza et al.

(Bellezza *et al.*, 2006) for Mb immobilization on zirconium benzenephosphonate. The affinity of nano-hydroxyapatite for biomolecules is strictly related to its high surface area. These two materials have different surface areas (120 vs 8 m^2/g), but considering the uptake of myoglobin per mass unit, the hydroxyapatite is more loaded than zirconium benzenephosphonate. This fact is remarkable regarding the utilization of biomimetic hydroxyapatite nanocrystals as an innovative support for the immobilization of proteins with catalytic activity. However, according to the Freundlich isotherm, the adsorbent surface is considered to be energetically heterogeneous with nonidentical adsorption sites. When the term *1/n* (heterogeneity factor) is close to 1.0, the surface is characterized by a high degree of homogeneity. The calculated value of 0.42 shows a high level of surface heterogeneity, in agreement with the typical surface of the biomimetic hydroxyapatite nanocrystals at low crystallinity having a nonstoichiometric surface Ca/P molar ratio.

Myoglobin molecules are electrostatically neutral at pH 7.4. Previous studies have demonstrated that no remarkable relationship with the bulk Ca/P molar ratio of the particles was detected for neutral myoglobin adsorption (Kandori *et al.*, 2005). The Mb adsorption data on biomimetic hydroxyapatite nanocrystals was well fit to a Langmuir isotherm, a behaviour similar to that presented by other proteins and amino acids. In table 4.2 the values of *N* and *K* of the Langmuir isotherm reported for several proteins have been showed.

Table 4.2 Values of *N* and *K* Langmuir isotherm parameters calculated for the adsorption of several biomolecules on different hydroxyapatites

Sorbent	Adsorbate	N (mol/m^2)	K (M^{-1})	Reference
HA	BSA	$(23.4 - 42.1) \times 10^{-8}$	$(0.3 - 160) \times 10^5$	Ouizat *et al.*, 1999
HA	BSA	$(8.7 - 26.1) \times 10^{-9}$	$(0.1 - 1160) \times 10^5$	Hughes *et al.*, 1995
HA	Myoglobin	4.41×10^{-8}	0.7×10^5	This thesis
HA	Statherin	80×10^{-8}	211×10^5	Moreno *et al.*, 1984
HA	Poly-L-Asp	9×10^{-8}	15.7×10^5	Moreno *et al.*, 1984
HA	PRP1	20×10^{-8}	260×10^5	Moreno *et al.*, 1984
HA	Succinylated LSZ	$(1.2 - 8.2) \times 10^{-8}$	$(0.1 - 10) \times 10^5$	Barroug *et al.*, 1997
HA	rhBMP-2	$(3.8 - 11.5) \times 10^{-8}$	$(2.4 - 230) \times 10^5$	Boix *et al.*, 2005
HA	Amelogenin	6.09×10^{-7}	1.97×10^5	Bouropoulos *et al.*, 2003
CHAps	BSA	1.03×10^{-8}	1.2×10^5	This thesis
CHAns	BSA	4.77×10^{-9}	2.6×10^5	This thesis
CHAps	HSA	6.54×10^{-9}	1.1×10^5	This thesis
CHAns	HSA	7.18×10^{-9}	0.5×10^5	This thesis

Parameters *K* and *N*, calculated by linear fitting, represent the adsorption constant (affinity constant) and the number of binding sites, respectively. N is dimensionally expressed as the adsorbed amount of protein per surface unit. It is observed that the affinity constants *K* for myoglobin onto HA fall within the range of *K* values reported for the adsorption of bovine serum albumin (BSA) and succinylated lysozyme (LSZ) onto HA, under similar experimental conditions. However, they are lower than those of bone morphogenetic protein (rhBMP-2), poly-L-Asp, statherin, and PRP1, a salivary proline-rich phosphoprotein adsorbed onto HA under similar experimental conditions. The K value obtained in this work is consistent with the biological function of proteins considering that myoglobin and albumin are serum proteins whereas poly-L-Asp, statherin, PRP1, and rhBMP 2 are involved in biomineralization processes. Several kinds of adsorbed-adsorbent interactions can take place during protein adsorption on an inorganic surface, for instance, covalent or electrostatic chemical bonds, hydrogen and van der Waals bonds, and hydrophobic and hydrophilic interactions. The relative predominance of one of them over the others is closely related to the protein structure and the chemical-physical characteristic of the inorganic surface. For HA, it seems reasonable that hydrophobic interactions can be discarded and that electrostatic interactions between Mb and the HA surface could take place.

The test of Scatchard (Sharma *et al.*, 2001) has been performed in order to observe the presence or absence of cooperative effects in Mb protein adsorption.

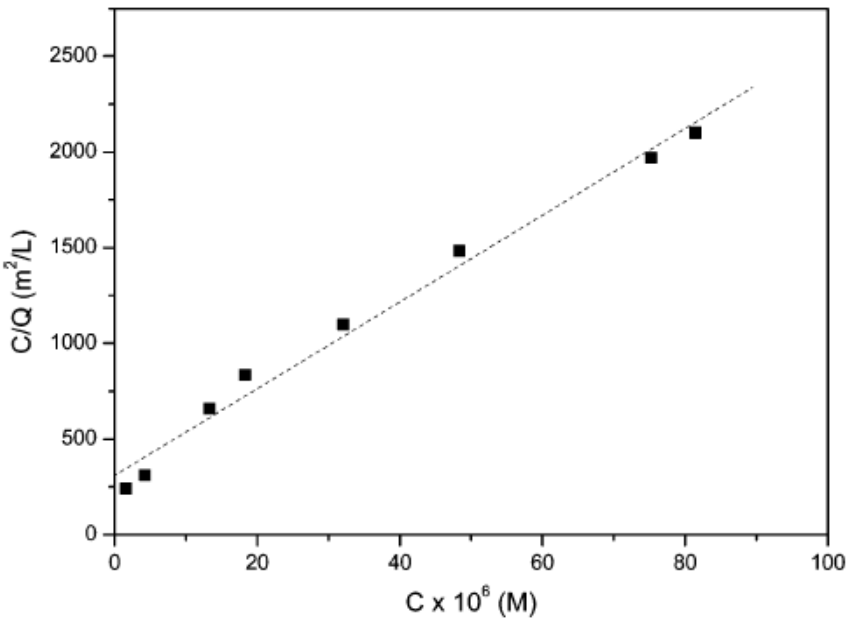

Figure 4.2 Plot of the Scatchard test, *C/Q* vs *C*, for Mb adsorption onto biomimetic hydroxyapatite nanocrystals.

The plot of *C/Q* versus *C* (where *Q* and *C* indicate the adsorbed amount of protein per adsorbent surface unit and the protein concentration at equilibrium, respectively) indicates no appreciable cooperative effects. The plot of the Scatchard test carried out for Mb adsorption on HA suggests the presence of independent noninteracting sites conforming to the Langmuir model. The correlation coefficient for the data in figure 4.2 is 0.993.

4.4 CONFORMATIONAL MODIFICATION OF MYOGLOBIN ON HYDROXYAPATITE NANOCRYSTALS

The adsorption kinetic profile of a 2 mg/mL myoglobin solution on HA is reported in figure 4.3.

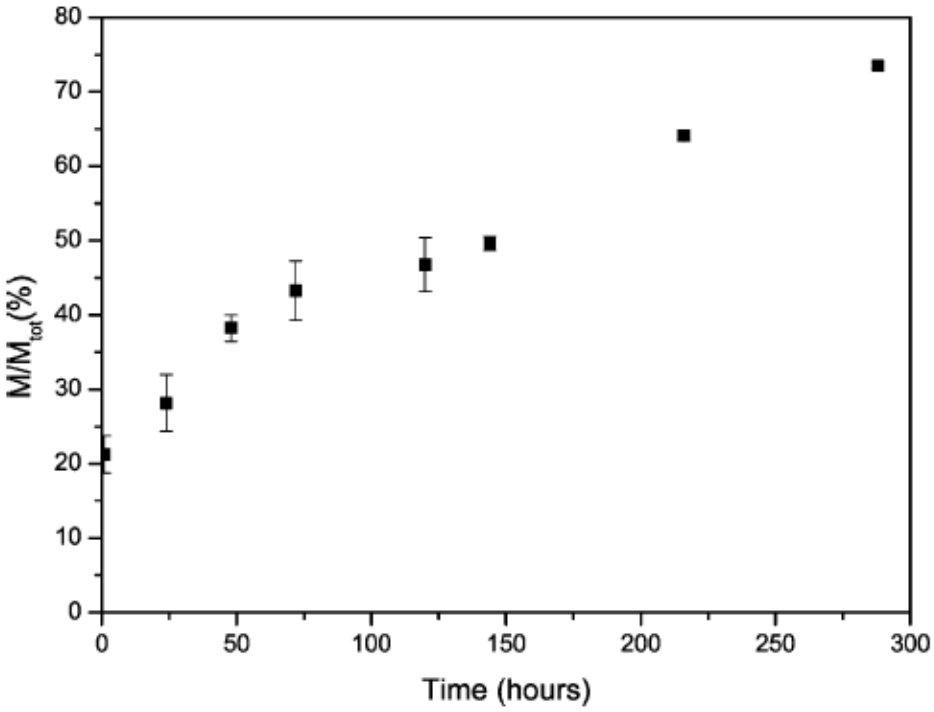

Figure 4.3 Adsorption kinetic profile of a 2 mg/mL myoglobin solution onto biomimetic hydroxyapatite nanocrystals: M/M_{tot} (%) (mass percentages of myoglobin adsorbed onto nHA with respect to the initial amount of protein) vs time.

The plot shows an almost linear profile, and the percentage of myoglobin mass adsorbed onto the HA with respect to the initial amount of protein (M/M_{tot} (%)) was 75% after 300 h. This value corresponds to an HA loading level of 13%, indicating the Mb weight with respect to the composite (Mb-nHA) weight (100) $W_{Mb\text{-}nHA}$). At the scheduled time, the Mb supernatant solution, upon adsorption onto HA, was analyzed by UV-Vis spectroscopy in order to appreciate protein conformational changes. The spectrum of the Mb solution after 28 h of interaction with nHA

(Figure 4.4, solid line) is superimposable with that of the native Mb solution. In fact, it shows a sharp Soret band at 409 nm, Q bands at 504 and 535 nm, and charge-transfer band 1 (CT1 band) at 632 nm and is characteristic of a six-coordinate high-spin (6-cHS) heme with a histidine residue (His-93) and a water molecule bound at the fifth and the sixth coordination positions of the iron atom, respectively (Feng *et al.*, 2001).

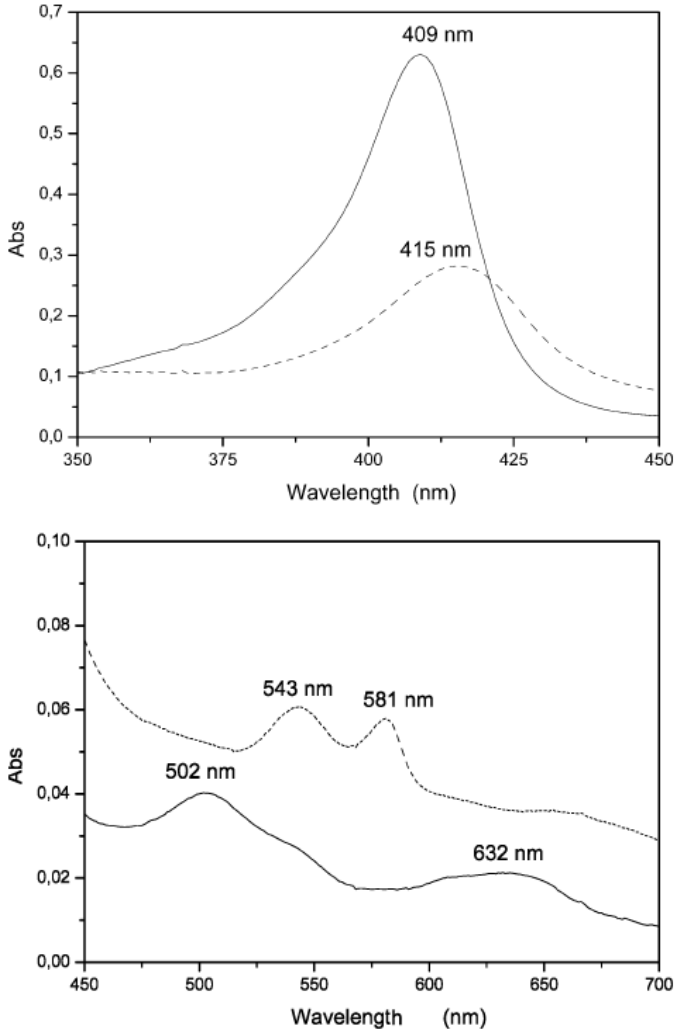

Figure 4.4 UV-Vis spectra of Mb solutions after 28 h (-) and 72 (---) following the interaction with biomimetic hydroxyapatite nanocrystals.

With increasing interaction time, the Mb spectrum shows appreciable changes compared to the native protein. After 72 h of interaction, the HA surface induces the formation of a new species at the expense of the 6-cHS heme, as is evident from the intensity decrease and red shift of the Soret band and the concomitant appearance of Q bands at 581 and 543 nm (Figure 4, dashed line). This spectrum, characteristic of a six-coordinate low-spin (6-cLS) heme, is very similar to that of ferric cytochrome b5, which has histidine residues as the fifth and sixth axial ligands (Tofani *et al.*, 2004).

The escape of water from the sixth position may result in a conformational change at the heme distal pocket: the histidine residue at the E7 helical position (His-64) moves toward the central iron and coordinates to it through the nitrogen donor. The simultaneous biomolecule adsorption and release on the HA surface is a dynamic process. The protein conformational modifications appear to be relevant at times longer than 72 h because after this time of interaction with the HA surface the concentration of native myoglobin in solution decreases and the concentration of altered molecules increases. The conformational changes seem to be irreversibile until myoglobin is coupled in solution with HA. However, the protein comes back to its native conformational state when the solution is separated from HA.

These findings lead us to assume that the Mb conformational changes are dynamic. The time needed to reach this refold in the native status ranges from 2 to 10 h, which is higher than the operation time requested to perform UV-Vis analysis. This ensured us of observing a "frozen" conformation.

In the solid state, the protein conformational modifications have been analyzed by Raman spectra. Surface-enhanced Raman spectroscopy (SERS) spectra were collected between 400 and 1750 cm^{-1} using a Jasco NRS-2000C instrument with a macro-objective of 20 × magnification. All spectra were recorded under backscattering conditions with 4 cm^{-1} spectral resolution using the 514.5 nm excitation line (Innova Coherent 70) with a power of ca. 10 mW. The detector was a 160 K frozen digital CCD (Spec-10: 100B, Roper Scientific Inc.). Native myoglobin powder (used as a control) was analyzed after a treatment of 24 h in Hepes buffer at 37 °C in a bascule bath and freeze drying. The solid samples were dissolved in a silver-hydroxylamine colloid prepared using the Leopold and Lendl method (Leopold *et al.*, 2003) at a concentration of about 10^{-5} M.

The myoglobin and HA-myoglobin conjugate powder SERS (hydroxylamine-silver colloid) spectra by which the chemical and electromagnetic effects due to the interaction of the heme group with a silver colloid allow a 1014-fold magnification of the vibrational bands, making it possible to reach the limit of single-molecule detection (Bizzarri *et al.*, 2002) are reported in figure 4.5. Raman bands in the region of1300-1700 cm^{-1} are sensitive to the dimensions of the porphyrin core: the main factors that influence the dimensions are the coordination, spin, and oxidation state of heme iron. The vibration of the C-N group at 1360-1370 cm^{-1} is sensitive to the oxidation state of the heme iron: ferric heme shifts this band to higher wavenumbers. In the 1500-1630 cm^{-1} region, vibrations of C-C of the porphyrin ring can be found, with the band near 1565 cm^{-1} being sensitive to the spin state of the heme iron and the band at 1620 cm^{-1} (stretching of vinylic CdC) being sensitive to both the spin and the oxidation state (Feng *et al.*, 2001). The relative intensity of these bands increases if the content of low-spin iron increases. After interaction with HA, the 1596 cm^{-1} band increases in

intensity, showing a higher content of low-spin iron. Another marker band of low-spin heme is at 1507 cm^{-1} (Droghetti *et al.*, 2005) and can be observed after the interaction with HA. The presence of the bands at 1596 and 1568 cm^{-1} in the myoglobin sample indicates that the powder is a mixture of two spin states.

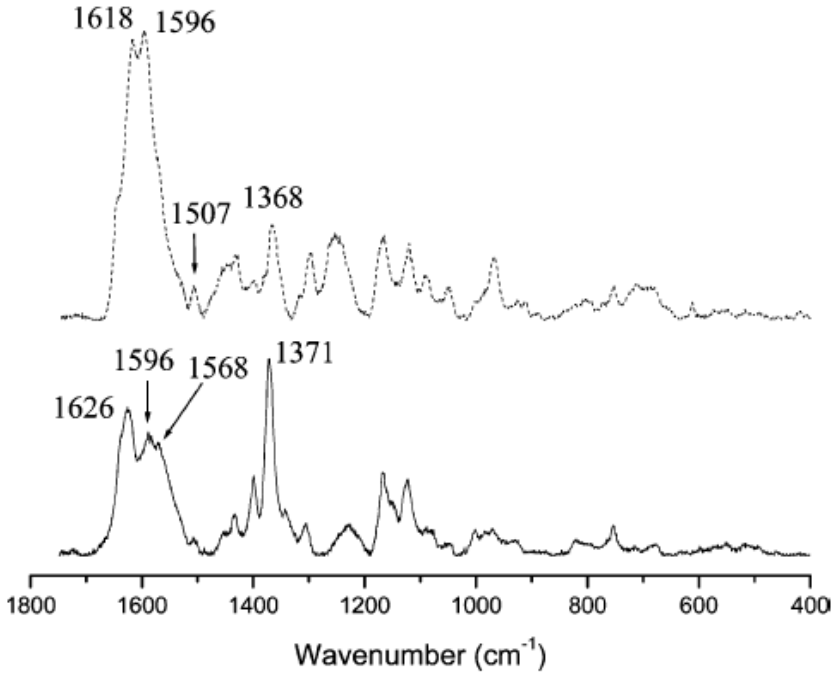

Figure 4.5 SERS (hydroxylamine-silver colloid) spectra of solid Mb (-) and solid Mb-HA (---).

It is reasonable that the modification of spin in a small native myoglobin sample is due to the freezedrying process. Instead, all myoglobin molecules adsorbed onto the HA show a low-spin state. Another important consideration is that the interaction with HA does not affect the oxidation state of iron in the heme moiety. The spin state of myoglobin is relevant in relation to the catalytic activity of the protein because only the five-coordinate high-spin form of the heme iron can activate exogenous species such as hydrogen peroxide by coordination to the free sixth octahedral position. Besides the protein form containing six-coordinate low-spin heme, a lack of activity by the immobilized myoglobin can arise from limited accessibility of the substrates to the active site of the protein bound on the solid surface.

The assumption that during the interaction with nanocrystals the heme and the residues near it are principally exposed to modification is supported by the examination of the surface electrostatic potential of myoglobin at pH 7.4 (Figure 4.6). The electrostatic interaction is one of the important factors that determine the extent of conformational changes. The exposed surface close to the heme

moiety is largely positive; furthermore, it is the zone in which a large number of charges are present.

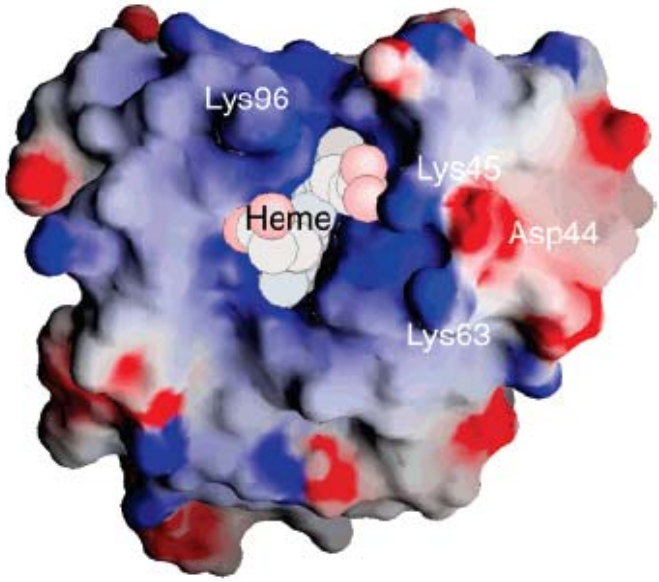

Figure 4.6 GRASP(graphical representation and analysis of structural properties) representation of the distribution of the electrostatic surface potential (Nicholls *et al.*, 1991) of the myoglobin (PDB ID 1YMB). The heme group atoms are represented as spheres. The positions of relevant residues are indicated. The values of surface potentials are expressed as a spectrum ranging from +10kT/e (deep blue) through 0kT/e (white) to -10kT/e (deep red). At a temperature of 298.15 K, kT/e) 25.7 mV.

This region could be the effective part of the molecule that interacts with HA, and because of its positive charge, it has a high affinity for the negative phosphates of the calcium-deficient surface. Therefore, the adsorption of myoglobin onto HA might follow a preferable orientation with respect to the random side-on or end-on adsorption mechanism onto titania and zirconia particles(Kondo *et al.*, 1996).

Transmission electron microscopy (TEM) investigations were carried out using a Philips CM 100 instrument (80 kV). The powdered samples of unfunctionalized HA were sonically dispersed in water, whereas the sonic dispersion has not been used with the functionalized samples. A few droplets of the slurry have been deposited on holey-carbon foils supported on conventional copper microgrids.

The TEM images of biomimetic hydroxyapatite nanocrystals interacting with Mb (Figure 4.7 a,b) show that the nanocrystals are more monodisperse than are the unfunctionalized ones (Palazzo *et al.*, 2007) (Figure 4.7c,d) as a result of the electrostatic repulsion between their covered charged

surfaces. The protein molecules adsorbed onto the HA surface are able to disaggregate the nanoparticles and, consequently, to increase the reactivity toward the biological environment.

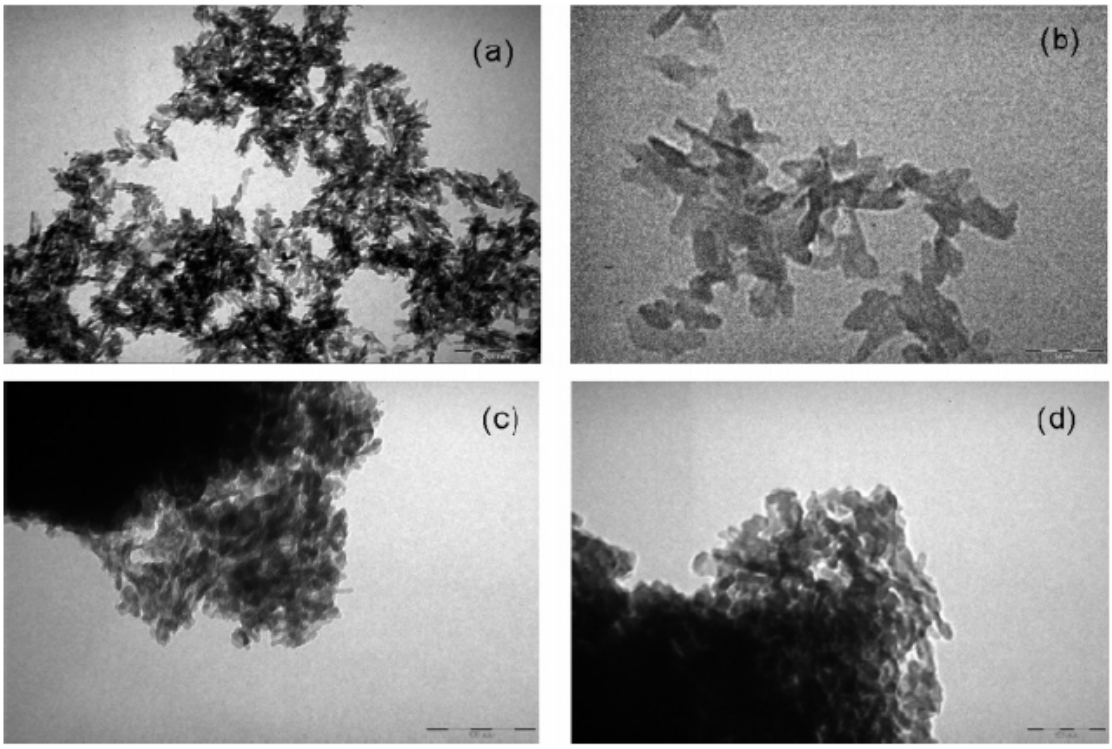

Figure 4.7 TEM images of synthetic biomimetic hydroxyapatite nanocrystals after interaction with Mb (a, b) and of synthetic biomimetic hydroxyapatite nanocrystals not interacting with the protein (c, d). Scale bars are 200 (a), 50 (b), 100 (c), and 50 (d) nm.

4.5 INTERACTION OF SERUM ALBUMINS WITH HYDROXYAPATITE

Carbonate-hydroxyapatite (CHA) nanocrystals with a nearly stoichiometric Ca/P ratio (1.67) were synthesized in order to produce plate-shaped and needle-shaped bonelike apatite phases. The powder fraction of nanocrystals having granular dimensions ranging from 100 to 150 μm was selected for this study. The surface Ca/P ratio determined by X-ray photoemission spectroscopy (XPS) analysis for CHAps and CHAns was significantly lower than the stoichiometric one (1.45 and 1.30 respectively) as a result of surface disorder. Specific surface area measurement was undertaken by using a Carlo Erba Sorpty 1750 instrument measuring N_2 adsorption at 77 K and adopting the well-known BET procedure. The specific surface area of CHAps and CHAns was 120 and 100 m^2/g, respectively. The carbonate content of the nanocrystals was quantified in about 2% wt for both CHA crystals by thermogravimetric investigations on dried samples using a Thermal Analysis SDT Q 600. Heating was performed in nitrogen flow (100 ml/min) using an alumina

sample holder at a rate of 5 °C/min up to 1200 °C. The weight of the samples was around 10 mg. Details of their synthesis, as well as the other physicochemical properties, are reported elsewhere (Palazzo *et al.*, 2007).

Samples of adsorbed human (HSA) and bovine (BSA) serum albumin were prepared by mixing 40 mg of CHA with 10 mL of protein dissolved in phosphate buffer (0.010 M Na_2HPO_4, 0.140 M NaCl, 0.003 M KCl) at pH 7.4 at different concentrations (ranging from 0.5 to 4 mg/mL) in a 10 mL polyethylene tube. The mixture was rotated end-over-end at 37 °C for 16 h. The solid, for the FT-IR spectroscopic investigation, was recovered by centrifuging at 12 675*g* for 3 min and then freeze drying at -60 °C under vacuum (3 mbar) for 12 h. The supernatant solution was assayed for protein content by UV spectroscopy (λ = 278 nm, ε_{BSA} = 42,000 M^{-1} cm^{-1}, ε_{HSA} = 35,000 M^{-1} cm^{-1}). The amount of adsorbed protein was calculated as difference between the concentrations of the initial solution and that of the supernatant. The UV-Vis spectra of albumin solutions were recorded between 200 and 800 nm using a Cary 300 BIO UV-Vis spectrophotometer (Varian, Palo Alto, CA) against a blank buffer solution. The measurements were performed using 1 cm quartz cell.

The results of serum albumins adsorption onto CHA are reported as isotherms in figure 4.8, where the adsorbed amount, $\Gamma_{albumin}$ (mg/m^2), is plotted against the protein concentration after adsorption, $C_{albumin}$ (mg/mL). The plots are characterized by an initial slope indicating high to medium protein affinity for the CHA surface.

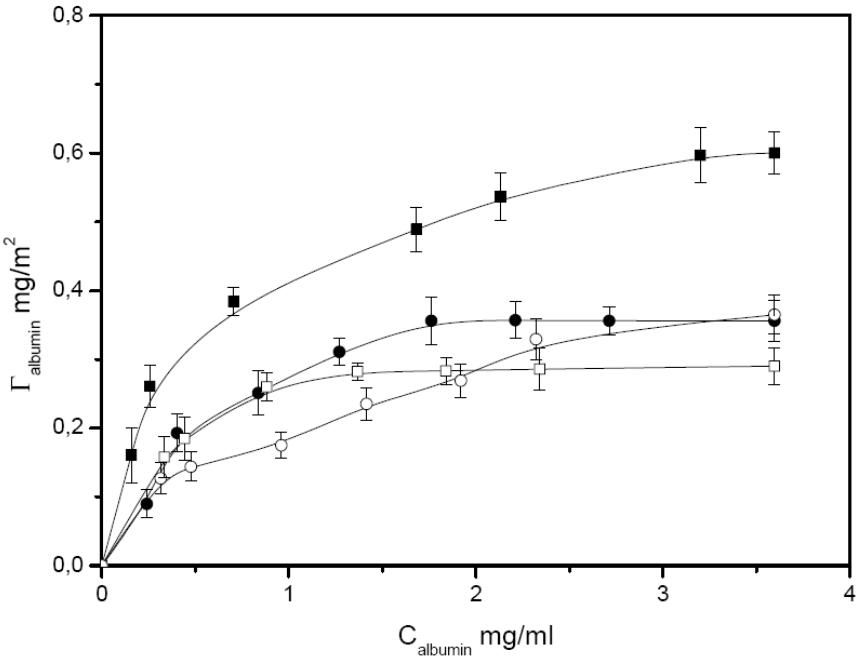

Figure 4.8 Adsorption isotherms of BSA onto CHAps (■); BSA onto CHAns (□); HSA onto CHAps (●) and HSA onto CHAns (○) at pH 7.4.

The adsorption saturation yields a plateau value corresponding to the maximum amount of serum albumins surface uptake. The adsorption saturation values are 0.60 mg/m^2 and 0.30 mg/m^2 of BSA on CHAps and CHAns, respectively. This findings are in good agreement with the data reported by Yin et al. (Yin *et al.*, 2002) and Kandori et al. (Kandori *et al.*, 2000), which observed a BSA adsorption limit on hydroxyapatite nanoparticles (around 20 nm) in the range of 0.60 mg/m^2. On the contrary, the adsorption saturation values are 0.35 mg/m^2 of HSA on both CHAps and CHAns. In this case, our results are not easily comparable with previous data because of the different materials and methods used (Mura-Galelli *et al.*, 1991). The increase in serum albumin concentration in buffer solution increases the surface coverage, until completion takes place using a serum albumin starting concentration higher than 4 mg/ml onto 40 mg of CHA. When the plateau value is reached in the adsorption isotherm, a monolayer of albumin molecules has been deposited.

Both the Langmuir and the Freundlich models have been utilized to describe the serum albumins adsorption isotherms (see equations 1 and 2). The values of the Langmuir and Freundlich constants calculated by linear fitting for albumins immobilization onto the CHA nanocrystals surface are compared in table 4.3, revealing that both models can well describe the albumin monolayer on CHA matrix.

Table 4.3 Adsorption parameters of BSA and HSA onto CHAps and CHAps nanocrystals calculated according to Langmuir and Freundlich models.

	Langmuir			Freundlich		
	Q_{max} mg/g of sorbent	a_L mL/mg	r^2	K_F mg/g of sorbent/ $(mg/mL)^{-1/n}$	1/n	r^2
BSA/CHAps	244	2.22	0.982	65	0.37	0.925
BSA/CHAns	95	2.87	0.905	23	0.24	0.836
HSA/CHAps	143	2.02	0.960	45	0.31	0.868
HSA/CHAns	56	1.55	0.910	20	0.44	0.957

Probably the two models represent a simplification of the real adsorption systems, which might be a combination of both. In fact, the Langmuir isotherm assumes an energetically homogeneous support surface with identical adsorption sites throughout. Therefore, these sites are expected to hold equal numbers of albumin molecules, thus forming a monolayer. Moreover, the Langmuir formula implies highly favourable and irreversible adsorption. The calculated Q_{max} values (maximum

adsorption capacity of the sorbent) are higher for CHAps than for CHAns, in agreement with a greater specific surface area.

On the other hand, according to the Freundlich isotherm, the sorbent surface is considered to be energetically heterogeneous, with non-identical adsorption sites. When the term 1/n (heterogeneity factor) is close to 1.0, the surface is characterized by a high degree of homogeneity. The calculated values in the range from 0.24 to of 0.44 show a high level of surface heterogeneity, in agreement with the typical surface of the biomimetic hydroxyapatite nanocrystals having low crystallinity and a non-stoichiometric Ca/P molar ratio.

The serum albumin adsorption data on hydroxyapatite nanocrystals fit well into a Langmuir isotherm, a behaviour similar to that exhibited by other proteins and amino acids. Table 4.2 shows the values of *N* and *K* of the Langmuir isotherm reported for serum albumins. Parameters *K* and *N*, calculated by linear fitting, represent the adsorption constant (affinity constant) and the number of binding sites, respectively. *N* is dimensionally expressed as the adsorbed amount of protein per surface unit. It is observed that the affinity constants *K* for serum albumins onto CHA nanocrystals is in agreement with the other data previously reported and falls within the range of K values reported for the adsorption of myoglobin and succinylated lysozyme (LSZ) under similar experimental conditions. However, they are lower than those of bone morphogenetic protein (rhBMP-2), poly-L-Asp, statherin, amelogenin and PRP1, a salivary proline-rich phosphoprotein adsorbed onto hydroxyapatite under similar experimental conditions. The K value obtained in this work is consistent with their different biological functions, considering that albumin and myoglobin are serum proteins whereas poly-L-Asp, statherin, PRP1, and rhBMP-2 are involved in biomineralization processes.

Several kinds of adsorbed-sorbent interactions can take place during protein coating on an inorganic surface, for instance, covalent or electrostatic chemical bonds, hydrogen and Van der Waals bonds, and hydrophobic and hydrophilic interactions. The relative predominance of one of them is closely related to the protein structure and the physico-chemical features of the inorganic surface. For CHA, it seems reasonable that hydrophobic interactions can be ruled out and electrostatic interactions between serum albumins and CHA surface might take place prevalently.

The Scatchard test (Sharma *et al.*, 2001) has been performed in order to observe the presence of cooperative effects in serum albumin proteins adsorption. The plots of *C/Q* versus *C* (where *Q* and *C* indicate the adsorbed amount of protein per sorbent surface unit and the protein concentration at equilibrium, respectively) indicate no appreciable cooperative effects. The plots of the Scatchard test carried out for serum albumins adsorption on CHA nanocrystals (Figure 4.9) suggest the presence of independent non-interacting sites, conforming to the Langmuir model. The correlation

coefficient for the data in figure 4.9 are 0.998, 0.998, 0.970 and 0.989 for the adsorption of BSA onto CHAps and CHAns; and HSA onto CHAps and CHAns, respectively.

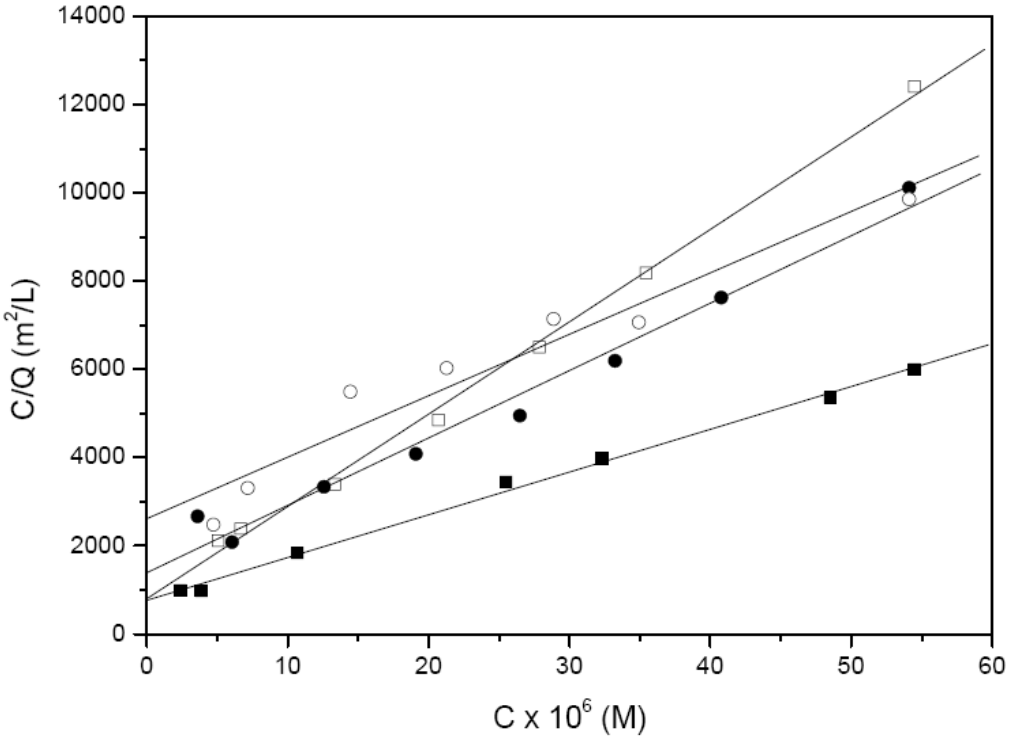

Figure 4.9 Plots of the Scatchard test, *C/Q* vs *C*, for the adsorption of BSA onto CHAps (■); BSA onto CHAns (□); HSA onto CHAps (●) and HSA onto CHAns (○).

4.6 CONFORMATIONAL MODIFICATION OF SERUM ALBUMINS ON HYDROXYAPATITE NANOCRYSTALS

Quantitative analysis of the secondary structure of BSA and HSA adsorbed on the inorganic phase surface have been investigated by FT-IR spectroscopy. FT-IR measurements were carried out on both the protein samples and the solid adducts of CHA and BSA or HSA, respectively, lyophilized from the buffer solution. The infrared spectra were measured from 4000 to 400 cm^{-1} with 2 cm^{-1} resolution using a Bruker IFS 66v/S spectrometer. The sample compartment atmosphere had a total pressure of 2 mbar of air dried to an atmospheric dew point of −40 ◦C ($pH_2O \approx 13$ Pa) by means of a Balston 76-01 Membrane Air Dryer. Other settings include an 8 mm aperture, 16 scans, velocity 10 kHz, DLATGS detector, and a 3-term Blackman–Harris apodization function. KBr pellets were obtained under vacuum, using 2 mg of the powdered samples carefully mixed with 200 mg of infrared grade KBr. Fourier self-deconvolution and second derivative resolution enhancement were applied to narrow the widths of infrared bands and increase the separation of the overlapping

components. The resolution enhancement resulting from self-deconvolution and the second derivative is such that the number and position of the component bands to be fitted can be determined.

The curve-fitting was carried out employing BRUKER OPUS peak software (version 4.0). The number of bands was entered into the program along with their respective positions and half-heights. The program iterates the curve-fitting process to achieve the best Gaussian-shaped curves that fit the protein spectrum. The best fit is determined by the root mean square (rms) of differences between the original protein spectrum and the sum of all individual resolved bands. The assignment of component bands in amide I has been done for BSA (Falini *et al.*, 2006; Sabatino *et al.*, 2007) and HSA (Brummer, 1996) according to the literature data. The percentages of each secondary structure were calculated from the integrated areas of the component bands. Native albumin powder (used as control) was analyzed after a treatment of 16 hours in phosphate buffer at 37 °C in a bascule bath and freeze-drying.

Samples suspensions have been centrifuged in order to isolate the solid phase formed by the inorganic nanocrystals coated by the adsorbed protein. After freeze-drying, FT-IR spectroscopic investigations have been carried out on all the samples in the amide I (1700-1600 cm^{-1}) region. Fourier self-deconvolution and secondary derivative were applied to estimate number, position and width of the component bands (Figure 4.10, in which original and curve–fitted spectra are reported for the initial protein concentration of 1 mg/ml).

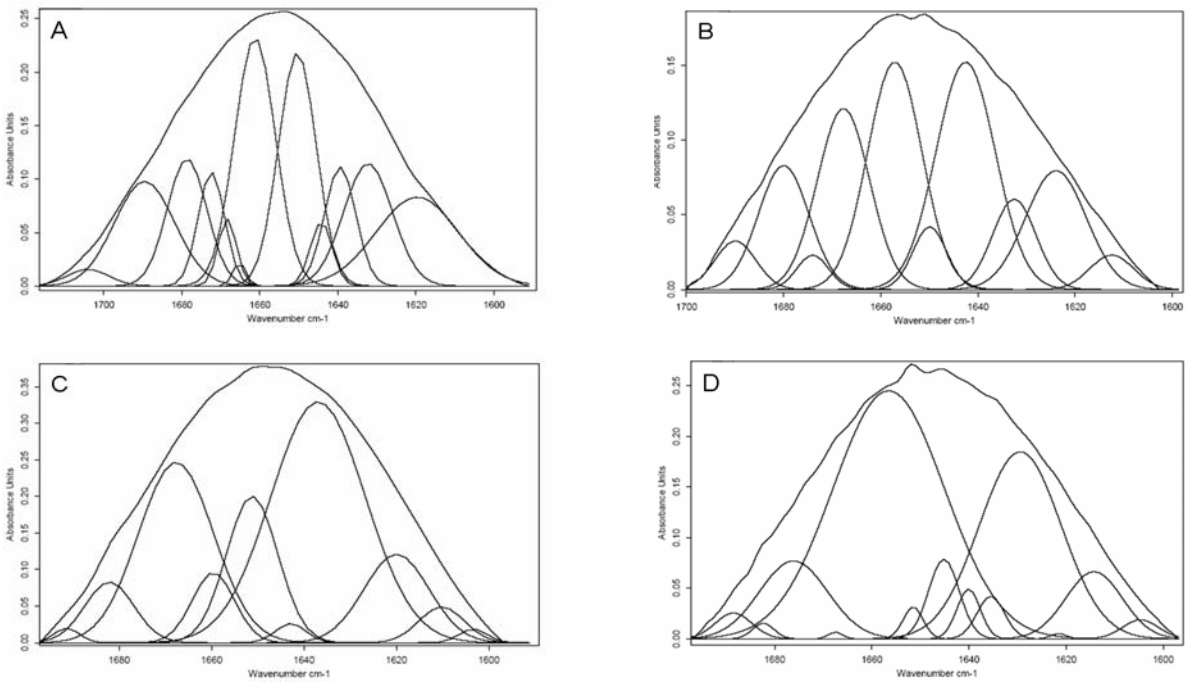

Figure 4.10 Curve-fitted amide I regions for CHAps-BSA (A), CHAps-HSA (B), CHAns-BSA (C) and CHAns-HAS (D)

From the second derivative of the bands the actual half-width can be estimated, based on which a curve-fitting process was iterated to achieve the best fitted curves. The component bands were assigned on the basis of the literature data. From the integrated areas of the component bands, the percentages of each secondary structure for BSA and HSA as such and adsorbed on CHAps and CHAns, respectively, were assigned. Table 4.4 reports secondary structure percentages for the freeze-dried native proteins, for comparison, and for the protein-coated pellets of CHAps and CHAns at different surface coverage (Γ).

Table 4.4 Secondary structure elements (%) from deconvolution of FT-IR spectra of the BSA and HSA lyophilized powder and HSA and BSA coated CHAns and CHAps nanocrystals

	$\Gamma_{albumin}$ (mg/m^2)	α-Helix (%)	β-Sheet (%)	β-Turn (%)	Random coil (%)
BSA		31 ± 2	23 ± 2	24 ± 3	22 ± 1
	0.116	18 ± 1	38 ± 3	35 ± 2	9 ± 1
CHAps-BSA	0.263	12 ± 1	27 ± 1	45 ± 3	16 ± 2
	0.478	11 ± 1	21 ± 2	59 ± 4	9 ± 1
	0.185	16 ± 2	46 ± 3	27 ± 2	11 ± 1
CHAns-BSA	0.255	18 ± 1	39 ± 2	29 ± 2	14 ± 2
	0.260	10 ± 2	32 ± 2	40 ± 4	18 ± 2
HSA		28 ± 3	27 ± 3	38 ± 2	7 ± 1
	0.193	24 ± 2	27 ± 4	35 ± 3	14 ± 1
CHAps-HSA	0.323	19 ± 2	24 ± 2	32 ± 3	25 ± 2
	0.327	10 ± 1	26 ± 3	43 ± 2	21 ± 2
	0.144	17 ± 2	46 ± 5	20 ±1	17 ± 2
CHAns-HSA	0.175	18 ± 3	35 ± 3	33 ± 2	14 ± 1
	0.325	9 ± 1	27 ± 2	39 ± 2	25 ± 3

From the data shown in table 4.4, it can be generally appreciated that the protein adhesion on an inorganic surface, driven by electrostatic interactions, brings to a significant reduction in helicity for both proteins on the two susbtrates. The BSA coated CHA nanocrystals show also an appreciable increase in β-turns. Since β-turns are the most flexible structure composed of hydrophilic aminoacids, they are the most efficient means to interact with a surface.

The modifications on the aperiodic structures (random coil) show different trends for the two proteins. The random coil amount decreases for BSA-coated nanocrystals as a function of the coating extent, while it increases for HSA-coated CHA nanocrystals with respect to the native structure. The diverse modifications appear more clearly on the protein coated CHAps nanocrystals, while CHAns appear to be less prone to physisorption (see figure 4.8) probably because of the different affinity of HSA and BSA towards the two sorbents. In addition, BSA and HSA behave differently on adsorption to the same substrate. Actually, the difference in the

percentage of random coil between BSA- and HSA-coated CHAps nanocrystals is in agreement with a lower degree of interaction of HSA with the substrate and, consequently, with a lesser modification in the periodic structure.

However, it must be underlined, that the changes in secondary structures, in terms of helix and turns, are generally more evident for the higher surface coverage in CHAps nanocrystals. For CHAns the trend is not so strictly respected, suggesting a less homogeneous behaviour from the surface.

4.7 INTERACTION OF MYOGLOBIN WITH HYDROXYAPATITE-ALENDRONATE NANOCONJUGATE

An aliquot (1.5 mL) of alendronate solution (1 mg/mL) was added to 10 mg of HA (see section 4.3) in a 2 mL conical polyethylene Eppendorf tube. After 15 s of treatment in a vortex apparatus, the HA suspension was maintained in a bascule bath at 37 °C. The adsorption profile for alendronate was determined by measuring the concentration of drug remaining in the supernatant solution as function of time. At scheduled times, aliquots (100 μL) of the supernatant that was well separated from the solid phase by 3 min of centrifugation at 10 000 rpm (12675g) on a micro Centrifugette 4214 were removed for drug quantification and replaced with fresh water. The concentration of alendronate was determined by UV-vis spectroscopy analysis. The quantity of the drug was measured by a colorimetric method based on the reaction of the primary amino group with ninhydrin in a methanolic medium in the presence of 0.05 M sodium bicarbonate. The coloured product was measured at 568 nm against the reagent blank (Taha *et al.*, 2003) ($\varepsilon = 29 M^{-1} cm^{-1}$).

The adsorption profiles of alendronate using aqueous solutions containing an initial drug concentration of 1 mg/mL (3×10^{-3} M) in the presence of HA are shown in figure 4.11. The plot showed that the maximum uptake of alendronate was significantly fast reaching a maximum value after about 24 h. The percentage of drug mass adsorbed onto the HA nanoparticles with respect to the initial drug mass was about 90%. This value corresponds to an HA loading level of 8.3%, as the alendronate weight with respect to the composite (alendronate-HA) weight ($100 = W_{alendronate\text{-}HA}$). The high adsorption of alendronate, however, despite its negative charge, suggests that the interaction with the HA surface takes place by ligand exchange in which the two phosphonate groups of the drug molecule replace two surface phosphate groups (Palazzo *et al.*, 2007). Interaction between the alendronate solution (1 mg/mL) and biomimetic hydroxyapatite nanocrystals was performed for 48 h, when the maximum uptake of alendronate was reached

(Figure 4.11) and the surface of the support was partially covered by a layer of bisphosphonate molecules.

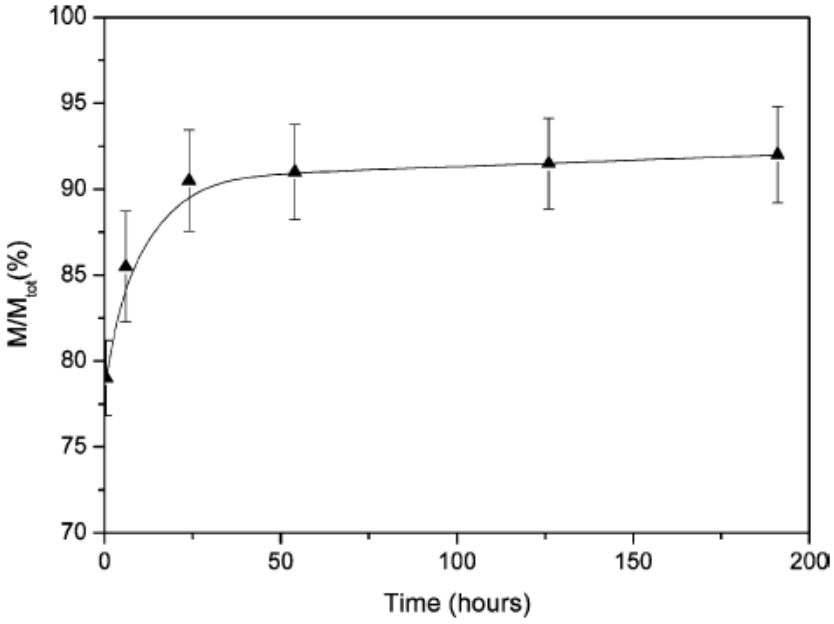

Figure 4.11 Kinetics of the adsorption of alendronate onto synthetic biomimetic hydroxyapatite nanocrystals: M/M_{tot} (%) (mass percentages of alendronate adsorbed onto HA with respect to the initial amount of drug) vs time.

The adsorption kinetic of myoglobin onto the alendronate-HA conjugate is dramatically affected by the alendronate functionalization of nanocrystals (Figure 4.12). The percentage of myoglobin adsorbed onto the HA/alendronate conjugates with respect to the initial protein concentration after 300 h was about 25% against 75% on the free support. The mass percentage of myoglobin adsorbed onto the conjugate is probably due to adsorption onto the partially free surface. The surface is able to undergo the adsorption of protein because of the insufficient quantity of alendronate covering the surface during functionalization and because of the small amount of alendronate released from the nanocrystals. After 24 h, the mass percentage of alendronate released in Hepes buffer from hydroxyapatite is about 30%.17 Mb adsorption is in agreement with the contemporary alendronate desorption and the resulting HA free-site enhancement. After that time, an almost steady state it has been reached in which the alendronate release is very slow and almost absent. This means that a stable alendronate-HA conjugate interacting with myoglobin is present. The supernatants were analyzed by UV-Vis spectroscopy, and in all of the samples any relevant shifts of the Soret band from 409 nm and of any other band have been observed. Therefore, it can be assumed that the surface functionalization of HA with alendronate avoids the adsorption of myoglobin and protects the protein from the modification of the coordination and the change in the spin of the heme moiety.

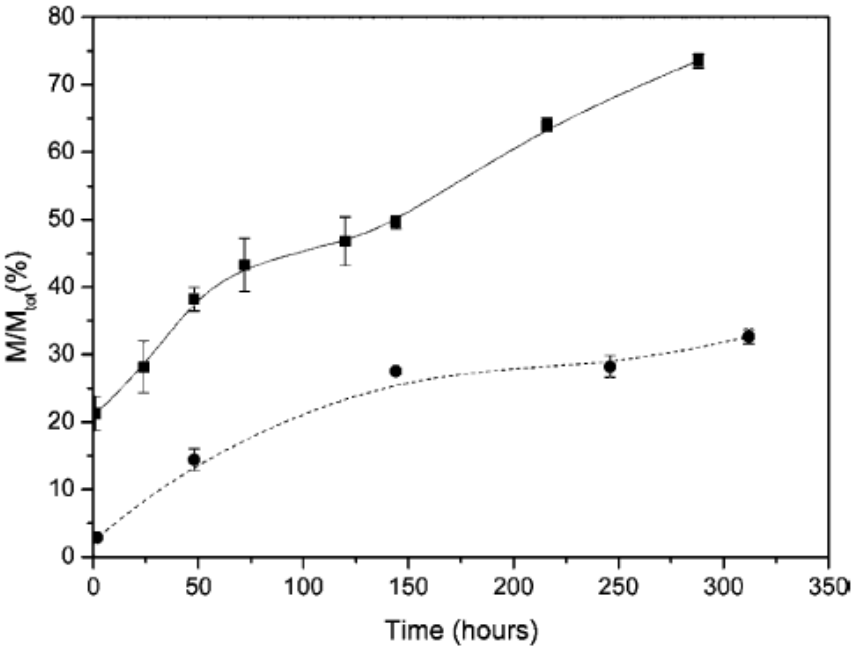

Figure 4.12 Comparison of adsorption kinetics of Mb onto HA nanocrystals (-) and Mb onto HA/alendronate (---).

4.8 CONCLUSIONS

Biomimetic hydroxyapatite nanocrystals represent an ideal bone-substitute material; the clarification of its interaction with proteins is central to understanding the integration of an implanted device or material with tissue. The HA-myoglobin interaction mechanism has been elucidated, pointing out that the maximum adsorption capacity of the support is higher than that of other inorganic phosphates, the adsorption isotherm can be described by both the Langmuir and Freundlich models, and the inorganic substrate affects the conformation of protein with respect to its adsorbed status. In particular, using UV-Vis and SERS, we found that the spin state of the myoglobin heme moiety changes from the six-coordinate high-spin native state to the six-coordinate low spin state as a consequence of the interaction with biomimetic hydroxyapatite nanocrystals. The spin state of myoglobin is relevant in relation to the catalytic activity of the protein. The surface electrostatic potential map of the protein allows us to hypothesize a preferential interaction mechanism through one defined region of the protein surface in spite of the random adhesion mechanism toward other inorganic supports. The heme moiety is attracted to the apatitic surface as a consequence of the surface disorder of the nanocrystals, which is connected to a negative surface charge with respect to the crystalline core. The immobilization of bisphosphonates onto HA is an important strategy for setting up a bone-specific drug-delivery device. Considering that the interaction of protein with HA-biomolecule conjugates tailored for specific therapeutic applications

plays a key role as a biological probe, we tested the myoglobin affinity for HA-alendronate bioconjugates. We found that alendronate avoids both the adsorption and the conformational changes of the myoglobin heme moiety. Myoglobin behavior toward alendronate-grafted HA crystals shows that this functionalization imprints surface selectivity to HA and drives the biological environmental response toward them.

The interaction mechanism of BSA and HSA with two kinds of carbonate-hydroxyapatite (CHA) nanocrystals has been elucidated, pointing out some important discriminating factors. First, the two proteins reach a very different maximum coverage versus the CHA nanoparticles provided with higher surface area, CHAps, showing a distinct affinity towards the same surface. Second, the adsorption isotherms can be described by both the Langmuir and Freundlich models because of the matrix behaviour as a mixture of an energetically homogeneous support surface and an energetically heterogeneous one , with non-identical adsorption sites.

Finally, the protein conformation are deeply and differently affected by the inorganic substrate showing a quite different structural stability among themselves. In particular, by using FT-IR spectroscopy, it has been found that BSA and HSA behaviour after desorption from the surface of both the synthetic CHA plate-acicular and plate-shaped nanocrystals differs due to the adsorption effects on both the adducts and the detached protein, depending on the nature of the sorbent surface and, possibly, the mode of interaction. It is well known that soft proteins are able to rearrange easily at solid-liquid interface; after desorption at low protein concentration structural modifications become more evident, while decreasing as a function of the surface coverage extent, with respect to their native structure as observed in the same conditions at pH 7.4 .

Since interaction of both BSA and HSA with CHA is mainly electrostatic in nature, a different behaviour may only be ascribed to differences in sorbent surface features.

REFERENCES

- Akawa, T.; Kobayashi, M.; Yoshida, M.; Matsushima, K.; Minoshima, H.; Sugimura, H.; Kanno, T.; Horiuchi, J. *J. Chromatogr. A* **1999**, *863*, 217.
- Bajpai, A. *Polym. Int.* **2005**, *54*, 304.
- Barroug, A.; Lernoux, E.; Lemaitre, L.; Rouxhet, P. *J. Colloid Interface Sci.* **1997**, *189*, 37.
- Bellezza, F.; Cipiciani, A.; Costantino, U.; Marmottini, F. *Langmuir* **2006**, *22*, 5064.
- Bellezza, F.; Cipiciani, A.; Costantino, U.; Nicolis, S. *Langmuir* **2004**, *20*, 5019.
- Bizzarri, A. R.; Cannistraro, S. *Appl. Spectrosc.* **2002**, *56*, 1531.

- Boix, T.; Gomez-Morales, J.; Torrent-Burgue, J.; Monfort, A.; Puigdomenech, P.; Rodrıguez-Clemente, R. *J. Inorg. Biochem.* **2005***, 99,* 1043.
- Bouropoulos, N.; Moradian-Oldak, J. *Calcif. Tissue Int.* **2003**, *72*, 599.
- Brunauer, S. P.; Emmet, P. H.; Teller, E. *J. Am. Chem. Soc*. **1938**, *60*, 309.
- Bummer, P. M. *Int. J. Pharm.* **1996**, *132*, 143.
- Carter, D. C.; Ho, J. X. *Adv. Protein Chem.* **1994**, *45*, 153.
- Droghetti, E.; Smulevich, G. *J. Biol. Inorg. Chem.* **2005**, *10*, 696.
- Falini, G.; Foresti, E.; Lesci, I. G.; Lunelli, B.; Sabatino, P.; Roveri, N. *Chem. Eur. J.* **2006**, *12*, 1968.
- Feng, M.; Tachikawa, H. *J. Am. Chem. Soc.* **2001**, *123*, 3013.
- Fujii, E.; Ohkubo, M.; Tsuru, K.; Hayakawa, S.; Osaka, A.; Kawabata, K.; Bonhommed, C.; Babonneaud F. *Acta Biomaterialia* **2006**, *2*, 69.
- Gray, J. J. *Curr. Opin. Struct. Biol.* **2004**, *14*, 110.
- Hughes, Wassell, D. T.; Hall, R. C.; Embery, G. *Biomaterials* **1995**, *16*, 697.
- Iafisco, M.; Palazzo, B.; Falini, G.; Di Foggia, M.; Bonora, S.; Nicolis, S.; Casella, G.; Roveri, N. *Langmuir* **2008**, *24*, 4924.
- Jager, C.; Welzel, T.; Meyer-Zaika, W.; Epple, M. *Magn. Reson. Chem.* **2006**, *44*, 573.
- Kandori, K.; Fudo, A.; Ishikawa, T. *Phys. Chem. Chem. Phys*. **2000**, *2*, 2015.
- Kandori, K.; Masunari, A.; Ishikawa, T. *Calcif. Tissue Int.* **2005**, *76*, 194.
- Kitagawa, T.; Ozaki, Y.; Kyogoku, Y. *Adv. Biophys.* **1978**, *11*, 153.
- Kondo, A.; Mihara, J. *J. Colloid Interface Sci.* **1996**, *177*, 214.
- Kosa, T.; Maruyama, T.; Otagiri, M. *Pharm. Res.* **1997**, *14*, 1607.
- Kosa, T.; Maruyama, T.; Otagiri, M. *Pharm. Res.* **1998**, *15*, 449.
- Leopold, N.; Lendl, B. *J. Phys. Chem. B* **2003**, *107*, 5723.
- Liu, T. Y.; Liu, S. Y.; Liu, D. M.; Liou, S. C. *J. Control. Release* **2005**, *107*, 112.
- Lu, H.; Hu, N. *J. Phys. Chem. B* **2006**, *110*, 23710.
- Miller, I.; Gemeiner, M. *Electrophoresis* **1993**, *14*, 1312.
- Moreno, E.; Kresak, M.; Hay, D. I. *Calcif. Tissue Int.* **1984**, *36*, 48.
- Mura-Galelli, M. J.; Voegel, J. C.; Behr, S.; Bres, E. F.; Schaaf, P. *Proc. Natl. Acad. Sci. USA* **1991**, *88*, 5557.
- Nicholls, A.; Sharp, K. A.; Honig, B. *Proteins: Struct., Funct., Genet.* **1991**, *11*, 281.
- Ouizat, S.; Barroug, A.; Legrouri, A.; Rey, C. *Mater. Res. Bull.* **1999**, *34*, 2279.

- Palazzo, B.; Iafisco, M.; Laforgia, M.; Margiotta, N.; Natile, G.; Bianchi, C. L.; Walsh, D.; Mann, S.; Roveri, N. *Adv. Funct. Mater.* **2007**, *17*, 2180.
- Paul, W.; Sharma, C. P.; *J. Mater. Sci. Mater. Med.* **1999**, *10*, 383.
- Peters T. *Adv. Protein Chem.* **1985**; *37*, 161.
- Peters T. *All about albumin; biochemistry, genetics, and medical applications.* San Diego: Academic Press; 1996.
- Roat-Malone, R. M. *Bioinorganic Chemistry*; John Wiley & Sons: New York, 2002.
- Roncone, R.; Monzani, E.; Labò, S.; Sanangelantoni, A. M.; Casella, L. *J. Biol. Inorg. Chem.* **2005**, 10, 11.
- Sabatino, P.; Casella, L.; Granata A.; Iafisco, M.; Lesci, I. G.; Monzani, E.; Roveri N. *J. Colloid Interface Sci.* **2007**, *314*, 389.
- Sharma, S.; Agarwal, G. P. *J. Colloid Interface Sci.* **2001**, *243*, 61.
- Spiro, T. G.; Stong, J. D.; Stein, P. *J. Am. Chem. Soc.* **1979**, *101*, 2648.
- Taha, E. A.; Youssef, N. F. *Chem. Pharm. Bull.* **2003**, *51*, 1444.
- Takemoto, S.; Kusudo, Y.; Tsuru, K.; Hayakawa, S.; Osaka, A.; Takashima, S. *J. Biomed. Mater. Res.* **2004**, *69*, 544.
- Tayyab, S.; Khan, N. J.; Khan, M. A.; Kumar, Y. *Biol. Macromol.* **2003**, *31*, 187.
- Tofani, L.; Feis, A.; Snoke, R. E.; Bert, D.; Baglioni, P.; Smulevich, G. *Biophys. J.* **2004**, *87*, 1186.
- Tubio, G.; Nerli, B.; Pico, G. *J. Chromatogr. B* **2004**, 799, 293.
- Wright, J. E. I.; Gittens, S. A.; Bansal, G.; Kitov, P. I.; Sindrey, D.; Kucharski, C.; Uludag, H. *Biomaterials* **2006**, *27*, 769.
- Xu, T.; Zhang, N.; Nichols, H. L.; Shi, D.; Wen, X. *Mater. Sci. Eng., C* **2007**, *27*, 579.
- Yin, G., Liu, Z., Zhan, J.; Ding, F.; Yuan, N. *Chem. Eng. J.* **2002**, *87*, 181.

CHAPTER 5
SILICA GEL STRUCTURE EFFECT ON CALCIUM PHOSPHATES CRYSTALLIZATION

5.1 STATUS OF THE ART

Traditionally, biomimeticists are inspired by biological structures and their functions, and focused on emulating or duplicating biosystems using mostly synthetic components and following traditional approaches (Veis, 2005). With the recent developments of molecular and nanoscale engineering in physical sciences and advances in molecular biology, biomimetic approach is now entering the molecular scale (Sarikaya *et al.*, 2003) By combining nature's molecular tools with synthetic nanoscale constructs, molecular biomimetic is emerging as a hybrid methodology (Sanchez *et al.*, 2005). Materials have uniquely functional properties at nanometre-scale dimensions that, if harnessed effectively, could lead to novel engineering systems with highly useful characteristics. Mechanical properties of nanostructured composites, electronic properties of low-dimensional semiconductors, magnetic properties of single-domain particles, and solution properties of colloidal suspensions, are all attractive and interesting, and directly correlate to the nanometre-scale structures that characterize these systems (Meyers *et al.*, 2008). However, the realization of the full potential of nano-technological systems has been limited due to the difficulties in their synthesis and subsequent assembly into useful functional structures and devices. Despite all the promise of science and technology at the nanoscale, the control of nanostructures and ordered assemblies of materials in two- and three dimensions still remains largely elusive. In particular the synthesis and characterization of biocompatible materials to be used in medicine have acquired a great deal of importance in material science and engineering (Hench *et al.*, 2002). Among them hydroxyapatite (HA) is prominent since it is a natural component in several human and animal mineralized tissue. In fact, hydroxyapatite represents 69% of the weight of bone, 75% of dentine and 95% of enamel. Pure stoichiometric hydroxyapatite chemical formula is $Ca_5(PO_4)_3OH$ (Dorozhkin *et al.*, 2002).

The recent trend in biomaterials research is focused on overcoming the limitations of calcium phosphates, more specifically hydroxyapatite ceramics, and in improving their biological properties via exploring the unique advantages of the nano-size materials. This trend towards nanotechnology is guided by the aim to improve their biological responses, since nano-HA is a constituent of bone. The chemical and biological properties of the latter are strictly linked to their nano-dimensions, the regulation of which requires a high level of biological and chemical control. Thus, from nano-

medicine to nanofabrics, the use of the nano-technology has encompassed almost all disciplines of human life. In fact, nano-structured materials offer more improved performances than their larger particle sized counterparts, due to their high surface–volume ratio and unusual chemical/electronic synergistic effects. In particular, the mineral phase of bone and tooth is constituted of hydroxyapatite crystals with length of about 100 nm, width of 20-30 nm and thickness of 3-6 nm and having low crystallinity, non-stoichiometric composition, crystalline disorder, and presence of carbonate ions in the crystal lattice (Lowestan *et al.*, 1989). Biomimetic calcium phosphates need to be synthesized with similar dimensions, structural and chemical properties (López-Macipe *et al.*, 1998). The excellent biological properties of hydroxyapatite nanocrystals, such as the lack of toxicity, inflammatory and immunitary responses, and high bioresorbability can be significantly increased by improving their biomimetism (Legeros, 1991).

Other remarkable consideration to set up a biomaterial is its bioactivity. A material to be bioactive must form links between its surface and living tissue, so that it becomes covered with a material layer. In the case of HA and bone, on starting mineralized layer the osteoblasts of living bone can proliferate and produce apatite and collagen, a process termed osteointegration. Recently, it has been shown that glasses of type Na_2O-CaO-SiO_2 are materials that favour osteointegration. This is because they interchange Na^+ and Ca^{2+} ions with protons in the surrounding fluid, a process that gives rise to Si-OH groups, which induce the nucleation of hydroxyapatite. The presence of Na^+ and Ca^{2+} ions also favours the nucleation of hydroxyapatite. (Hench *et al.*, 1998; Ning *et al.*, 2005).

A promising method to amplify HA nano-crystals bioactivity is the functionalization of their surface with bioactive molecules, which makes them able to act selectively on a specific iological environment (Palazzo *et al.*, 2007). Thus, the synthesis of apatite nano-crystals loaded with drugs, which can be released with a controlled kinetic, represents an attractive goal for their application in therapeutic treatments. The release of bioactive molecules is strongly affected not only by the chemical properties of the molecule but also the chemical and structural characteristics of the HA substrates in terms of their links with biomolecules and dissolution rate in the biological environment. An interesting way of tuning the hydroxyapatite dissolution kinetics would be to coat HA with layers of biocompatible amorphous silica, which is bioactive. Furthermore, a much wanted aspect of bone-substitute materials is to introduce an on-site working drug in combination with the implant (Sousa *et al.*, 2008; Andersson *et al.*, 2005). The advantage of localized biodegradable therapy includes high local drug concentration at the site of infection, as well as, obviation of the need for removal of the implant after treatment. A controlled drug release from the implant could also help to minimize the toxic side effects and further complications that might occur due to long drug therapy. In this way the synthesis of hydroxyapatite in silica matrix opens many possibilities to

set up a very powerful biomaterials as bone substitute and drug delivery platforms. (Villacampa *et al.*, 2000; Diaz *et al.*, 2006; Vallet-Regí *et al.*, 2006; Slowing *et al.*, 2007).
The sol-gel technology is now widely used to produce hybrid materials because it has allowed to overcome the difficulty of using the classical silica glass-based biomaterials. This difficulty was ue to the high process temperature employed in traditional methods of synthesis and the consequent difficulty of manipulating the internal microstructure of the matrix. Moreover the physical characteristics (including density, pore size and nanostructure) of the silica can be tailored by controlling the sol-gel reaction kinetics and in particular the relative rates of hydrolysis and condensation (Roveri *et al.*, 2008)

5.1 AIM OF THE WORK

We have investigated the possibility of coating synthetic calcium phosphates with porous silica layers, which could serve both to enhance bioactivity and tune biocomposite dissolution rate.
Here, it has been report a straightforward, low-temperature, template-based method of synthesizing an osteoconductive, hierarchically porous, multifunctional calcium phosphates/silica composite material by diffusion of Ca^{2+} ions through a metasilicate gel, set with phosphoric acid, at several pHs. The resulting material is deposited as a powder but can be also easily moulded into monolithic forms. In this work we performed a complete characterization of the composite calcium phosphates/silica synthesized in gel varying the pH and density of the silica solution. We highlighted the crystallization of different calcium phosphates phases and the covering silica differently structured as a function of the pH. This study put in evidence the emergence of a new generation of biomaterials that could be induce the development of functional composite materials. In this field, the use of innovative processes to combine a graded architecture and chemical composition in association with different active molecules might be promising. This study could lead to significant improvements of the performances of implants in term of osteointegration, in possible association with the ability to deliver biologically active substances to the target tissues.

5.3 SYNTHESIS AND CHARACTERIZATION OF CALCIUM PHOSPHATES IN SILICA GEL

A series of calcium phosphate crystallization experiments have been performed into silica gel prepared from metasilicate solutions with two different densities and several pH values in the range from 5.4 to 10.3 (Table 1). The gels were prepared in a glass vial having a diameter of 15 mm starting from solutions of sodium metasilicate (Aldrich, SiO_2 44-47% w/w) at 1.03 or 1.09 g/cm^3

density acidified with 1.2 M H_3PO_4 (Riedel-de Haën, 85% v/v). Ultrapure water (0.22 μS, 25 °C) was used. Experiments were performed at pH values ranging from 5 to 11, using different amounts of phosphoric acid. The pH values of gels after the polymerization were measured using a Sentron IntelliCupFet probe. We did not carry out experiments using a 1.03 g/cm3 metasilicate solution density at a pH higher than 11 because of the long gelation time.

One millilitre of a 1.00 M $CaCl_2$ (Aldrich 98% w/w) solution was poured onto 1.00 ml of the gel and allowed to diffuse and react with the phosphoric acid used to set the silica gel. The diffusion process was carried out for 7 days and after that period the materials were washed twice with water, freeze-dried at −60 °C under vacuum (3 mbar) for 12 h and well milled.

At the density of 1.03 g/cm3 periodical precipitation calcium phosphates Liesegang rings (Liesegang, 1896) were observed. The number of these rings increased with the time and the distance between two consecutive rings increased towards going from the up to the bottom of the vial. On the contrary, using metasilicate solution with density of 1.09 g/cm3 a continuous precipitation of white material through the vial was observed.

Table 5.1 Experimental conditions of silica gels formation

density (g/cm^3)	pH				
1.03	5.45	6.83	7.64	9.38	10.28
1.09	5.42	6.90	7.54	9.33	10.30

Powder X-ray diffraction patterns were collected using a PanAnalytical X'Pert Pro equipped with X'Celerator detector powder diffractometer using Cu Kα radiation generated at 40 kV and 40 mA. The instrument was configured with a 1/32° divergence and 1/16° antiscattering slits. A standard quartz sample holder 1 mm deep, 20 mm high and 15 mm wide was used. The diffraction patterns were collected within the 2θ range from 1.5° to 60° with a step size (Δ 2θ) of 0.017° and a counting time of 3 s.

The powder X-ray diffraction pattern profiles of the calcium phosphates precipitated in the gels at density 1.03 g/cm^3 as function of pH values are reported in figure 5.1. In them the background has been subtracted, thus the two broad bands produced by the amorphous silica are absent. The marked peaks at 5° 2θ (100), 12° 2θ (020) and 26° 2θ (002) are the distinguishing reflections of the three main phases revealed: octacalcium phosphate ($Ca_8H_2(PO_4)_6{\cdot}5H_2O$; OCP), di-calcium phosphate di-hydrate or brushite ($CaHPO_4{\cdot}2H_2O$; DCPD) and hydroxyapatite ($Ca_5(PO_4)_3OH$; HA), respectively. The other diffraction peaks identified the same phases but were not labelled for clarity. An

important observation is that the diffraction peaks associated to the crystalline planes (020) of brushite and (002) of HA are more intense than those ones in the reference patterns (PDF files); this fact indicates a preferential orientation and/or growth of the crystals along the *b* and *c* axis of DCPD and HA, respectively. It is to note that at high pH values (>7) the formation of HA takes place. Brushite forms in high proportion at low pH values but is still present at high pH values.

Using the metasilicate gel with density 1.03 g/cm^3 at high pH values (9-10) the formation of octacalcium phosphate, the hydrated form and a precursor of hydroxyapatite is also observed together with HA.

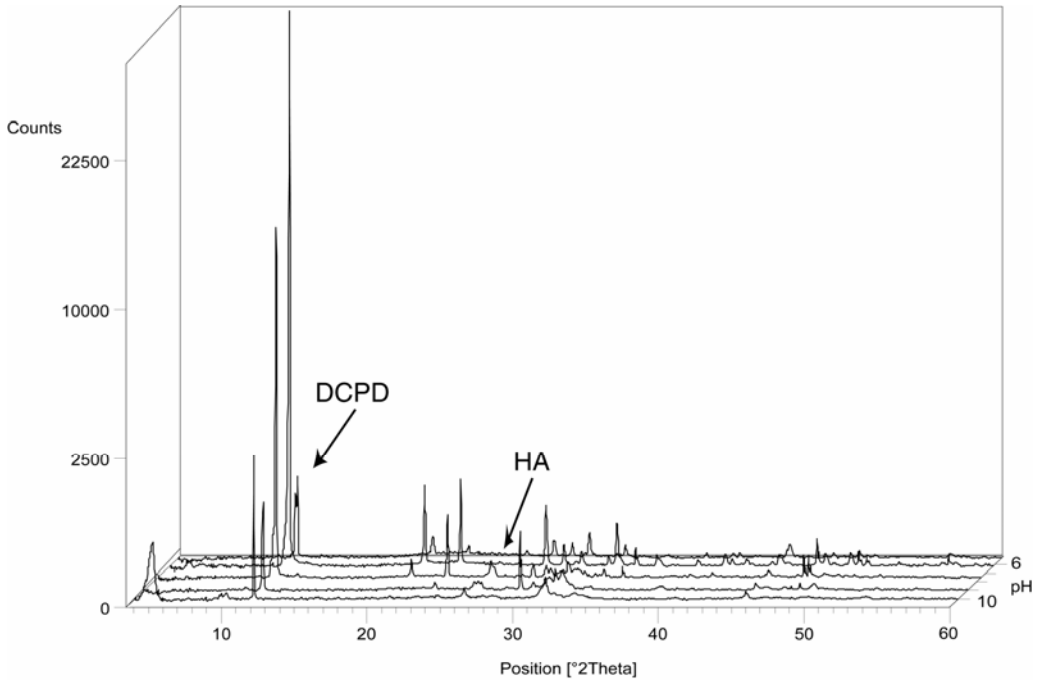

Figure 5.1 Powder X-ray diffraction patterns of the precipitates obtained at different pH values of the silica gel prepared from metasilicate solution of density 1.03 g/cm^3

Figure 5.2 shows the powder X-ray diffraction patterns of the crystalline phases precipitated in gels obtained from metasilicate solution of density 1.09 g/cm^3 as a function of gel pH. Also in this case the amorphous background has been subtracted to facilitate the reading of the diffraction patterns. The peaks marked are those ones characteristic of OCP, DCPD and HA at 5° 2θ (100), 12° 2θ (020) and 32° 2θ (112), respectively. In this set of experiments at high pH values (>9) the selective formation of hydroxyapatite at the expense of brushite is favoured. Also at this density the diffraction peaks associated to the reflections in the crystalline planes (020) of brushite and (002) of HA indicate a preferential orientation of the crystals. In this set of experiments HA crystallized together with OCP at pH values >10 only.

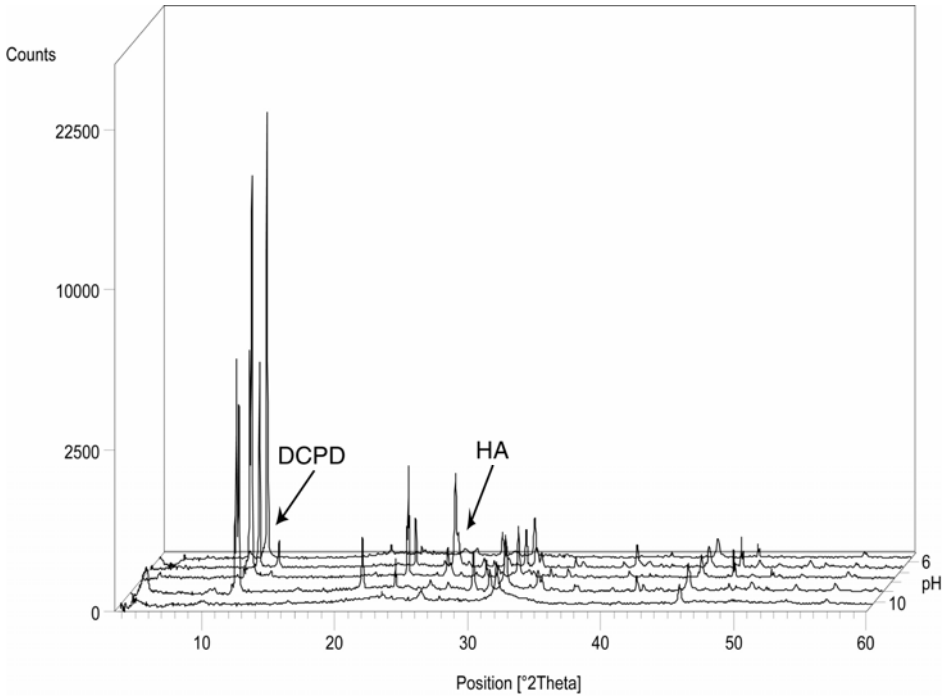

Figure 5.2 Powder X-ray diffraction patterns of the precipitates obtained at different pH values of the silica gel prepared from metasilicate solution of density 1.09 g/cm^3

DCPD crystallizes in the monoclinic system and its crystal consists of chains of Ca^{2+} and PO_4^{3-} ions each one arranged parallel to each other. Lattice water molecules are interlayered between the calcium and phosphate chains (Johnsson *et al.*, 1992). OCP has a layered structure involving apatitic and hydrated layers. The apatitic layers contain calcium and phosphate ions distributed in a manner similar to that one for HA, while the hydrated layer contains lattice water and less densely packed calcium and phosphate ions (Hill *et al.*, 1987).

The quantitative analysis of the crystalline phases was carried out using QUANTO (Altomare *et al.*, 2001), a Rietveld (McCusker *et al.*, 1999) computer program for quantitative phase analysis of polycrystalline mixtures. The crystallographic structures of HA, DCPD, DCP and OCP (Miyake *et al.*, 1986; Curry *et al.*, 1971; Jones *et al.*, 1961; Beevers, 1958) were used as structural models for quantitative phases analysis in the Rietveld refinement of diffraction patterns. Profile fitting refinements were obtained by varying scale factor, background coefficient, profile function parameters, unit cell parameters and preferential orientation of DCPD along (020) and HA along (002). Atomic thermal factors, site occupancies and atomic positions were kept fixed during the refinement.

The percentage (% wt) of each calcium phosphate phase in the samples obtained at different condition is reported in table 5.2. It is worthy to note that increasing the pH values the formation of hydroxyapatite increases at the expense of the brushite, a phase which preferentially forms close to neutral one. Comparing the two working densities in the pH range from 5.4 to 10.3 the phase

percentage of brushite decreases, whereas that one of HA increases sharply when the density was 1.03 g/cm^3 and smoothly when it was 1.09 g/cm^3. At pH 10.3, the HA/OCP ratio at 1.09 g/cm^3 density is inverted respect to what happens in 1.03 g/cm^3. Moreover using the metasilicate solution of density 1.09 g/cm^3, in the pH range from 6 to 8 the formation of DCP takes place. These observations are consistent with the fact that OCP and DCPD the hydrated form of HA and DCP respectively can be preferentially formed in the less dense gel. In fact in it the amount of water entrapped into the pore is higher with respect to that one in 1.09 g/cm^3 dense gel.

Table 5.2 Weight percentage (%) of each calcium phosphate phase calculated by Rietveld refinement of diffraction patterns.

Density (g/cm^3)	pH	DCPD (% wt)	HA (% wt)	OCP (% wt)	DCP(% wt)
1.03	5.45	100	-	-	-
	6.83	100	-	-	-
	7.64	70.3 ± 1.5	15.7 ± 5.4	-	-
	9.38	66.1 ± 1.2	19.7 ± 4.4	14.2 ± 1.6	-
	10.28	10.0 ± 0.9	23.4 ± 1.9	66.6 ± 0.4	-
1.09	5.42	100	-	-	-
	6.90	71.3 ± 4.7	18.1 ± 6.5	-	10.6 ± 1.5
	7.54	65.7 ± 8.1	24.3 ± 7.0	-	10.0 ± 2.9
	9.33	34.4 ± 0.9	65.0 ± 1.2	-	-
	10.30	-	89.8 ± 0.9	10.2 ± 0.9	-

Both DCPD and OCP have been implicated as possible precursors for the formation of apatite. It has been demonstrated that under neutral or basic conditions the metastable phases brushite and OCP transform to HA through dissolution and reprecipitation processes, following the Ostwald rule of crystals ripening (Zhan *et al.*, 2005). The unexpected large amount of brushite at basic pH values is probably due to two important factors, usually ignored in the crystallization in silica gels by diffusion. The first effect is that the diffusion of the concentrated calcium chloride solution in the gel decreases the pH at the front of crystallization. The second effect is that at the interface between gel and calcium chloride solution occurs a massive precipitation of very long crystals of brushite (about 1 mm). In this zone the pH is controlled by the calcium chloride solution, which is in the range of stability of brushite. This strongly influence the calcium phosphates phase composition of the gels.

The phase variation in the precipitate was also monitored by Fourier Transformed Infrared (FT-IR) spectroscopy. The infrared spectra were recorded in the wavelength range from 4000 cm^{-1} to 400 with 2 cm^{-1} resolution using a Thermo Nicolet 380 FT-IR spectrometer. A powdered sample

(approximately 1 mg) was mixed with about 100 mg of anhydrous KBr. The mixture was pressed at 10t pressure into 7 mm diameter discs. Pure KBr disc was used as blank.

The spectra (Figure 5.3a and 5.3b) recorded in the wavelength region between 400 cm^{-1} and 700 cm^{-1} show two peaks at 576 cm^{-1} and 528 cm^{-1} due to the bending modes of the O-P-O bonds of the phosphate group of brushite (dotted lines) and two peaks at 561 cm^{-1} and 602 cm^{-1} due to the bending modes of the O-P-O bonds of the phosphate group of hydroxyapatite (straight lines) (Koutsopoulos, 2002).

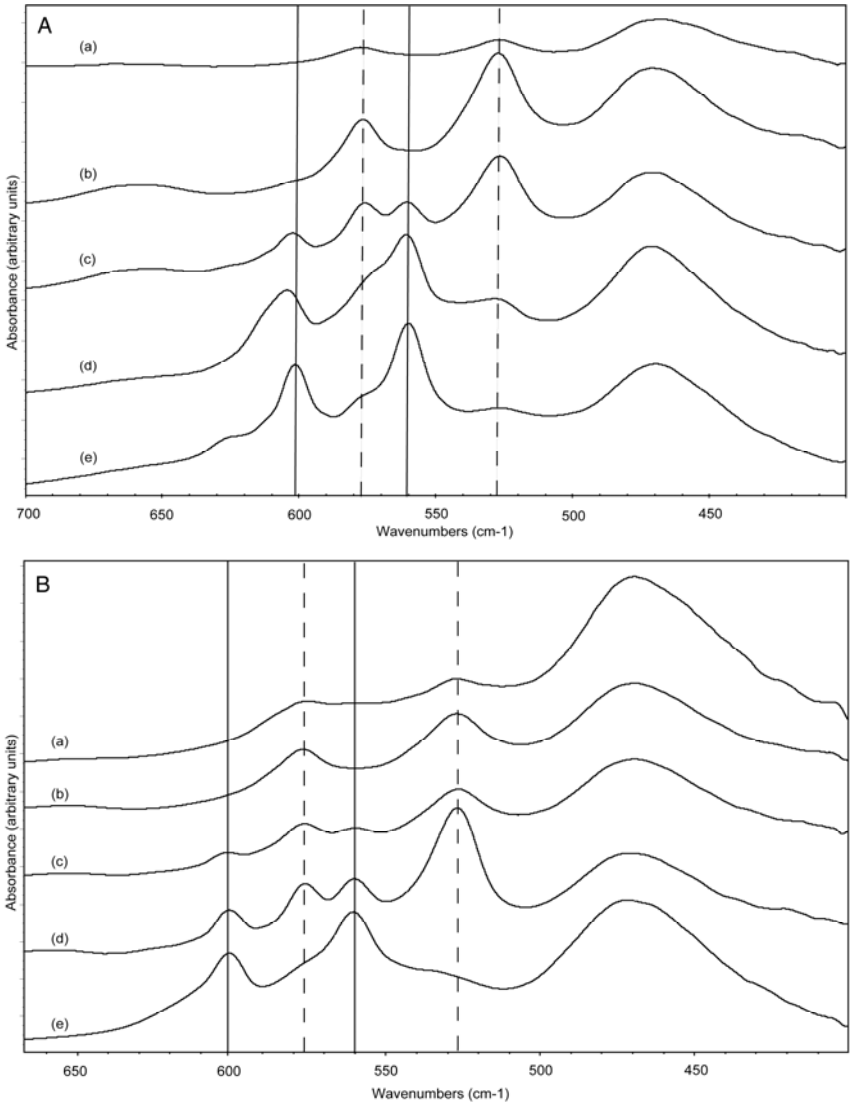

Figure 5.3 FT-IR spectra of the samples obtained at pH 5.45 (a), 6.83 (b), 7.64 (c), 9.38 (d), 10.38 (e) (density 1.03 g/cm^3) (A) and pH 5.42 (a), 6.90 (b), 7.54 (c), 9.33 (d), 10.30(e) (density 1.09 g/cm^3) (B). The peaks at 561 cm^{-1} and 602 cm^{-1} correspond to the bending modes of the O-P-O bonds of the phosphate group of hydroxyapatite (-). The peaks at 576 cm^{-1} and 528 cm^{-1} correspond to the bending modes of the O-P-O bonds of the phosphate group of brushite (---).

The transition with the pH increases of the calcium phosphate precipitate from brushite to hydroxyapatite is clear. In fact, increasing the pH values, the bands of brushite disappear whereas bands of hydroxyapatite appear. Comparing the two densities, it is observed that the peaks of brushite at high pH value (>10) using the 1.03 g/cm^3 silica density are present, while they are absent using the 1.09 g/cm^3 silica density. These observations are consistent with the calcium phosphates phases founded by XRD.

In order to study the structure and water content of the produced silica, and how these properties influence the calcium phosphates formation the dried gels structure was monitored by differential scanning calorimetry (DSC). Differential scanning calorimetric investigations have been carried out on dried samples using a DSC Q100 instrument (TA Instruments, New Castle, DE, USA). Heating was performed in nitrogen flow (25 ml/min) using an aluminium sample holder at a rate of 10 °C/min up to 300 °C. The initial weight of samples was around 5 mg. The thermal analyses (Figure 5.4) revealed two endothermic peaks around 50° C and 120° C due to two different water losses, one imputable to the adsorbed water and the other one, at higher temperature, imputable to water entrapped into "funnel shaped" pores.

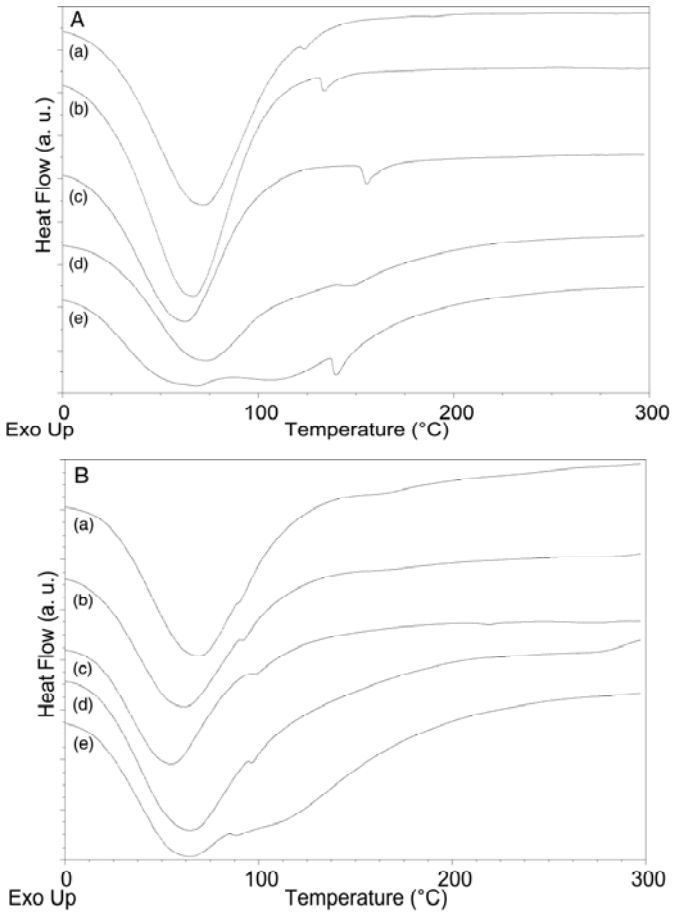

Figure 5.4. DSC curves of the dried silica obtained at pH 5.45 (a), 6.83 (b), 7.64 (c), 9.38 (d), 10.38 (e) (density 1.03 g/cm^3) (A) and pH 5.42 (a), 6.90 (b), 7.54 (c), 9.33 (d), 10.30 (e) (density 1.09 g/cm^3) (B)

Increasing the pH until 7, the temperature of the higher transition increased, whereas from 7 to 10 pH values the temperature of the peak decreased, according to a modified silica structure.

The effect of the pH during the synthesis on the pore structure and morphology has been extensively studied (Brinker *et al.*, 1990). Changes in solution pH alter the relative rates of hydrolysis and condensation, yielding products ranging from weakly branched to particulate silica sols. The polymerisation process can be divided into two approximate pH domains: pH 2-7 and pH > 7. pH 7 appears as a boundary because the silica solubility and dissolution rates are maximised at or above pH 7. The kinetics and growth mechanisms of the reaction depend on the pH value of the solution. With acidic pH, particle growth stops as soon as the size of 2 to 4 nm is reached. Above pH 7 particle growth is mainly dependent on the temperature, and particles of more than 100 nm in diameter can be formed. Above pH 7 particles are negatively charged and repel each other and no aggregation of particles occurs. At low pH, repulsive forces between particles are weak and particles collide and form continuous networks leading to gels (Zhan *et al.*, 2005).

This behaviour is present in both silica gels set at 1.03 g/cm^3 and 1.09 g/cm^3 density but with the difference that the second endothermic peak in figure 5b is shifted to temperatures below 100°C. This fact is due to a weak interaction of silica set at 1.09 g/cm^3 density with structural water in agreement with the less time of gelation of this material. The silica gelation time was of few seconds using solutions with 1.09 g/cm^3 density, while using solutions at 1.03 g/cm^3 density, it was of few minutes for the pH values of 5.45 and 6.83 and of about one day for pH values of 9.38 and 10.28.

The relative rates of hydrolysis and condensation effectively determine the morphology of the final silica. Generally, silica particles are positively charged at low pH and negatively charged at high pH. At the isoelectric point of silica (between pH 1 and 3), where the electrophoretic mobility of particles is zero, or at the point of the zero charge, the condensation rate is the lowest (Iler, 1979). The weakly basic and moderate acidic sols have significant amounts of deprotonated silanol groups (SiO^-) which increase the condensation rate causing a formation of highly branched silica species. Gelation of these branched species results in the formation of mesoporous regions with a pore size between 2 nm and 50 nm. As the pH is lowered to the isoelectric point (between 1 to 3), the gelation times are increased in the same way as in the basic sol, and this leads to linear or randomly branched silica gel having in this case highly microporous structure with the pore diameter < 2 nm. At very high acid concentrations, below isoelectric point (< 1) the dried gels become more mesoporous. This is due to the protonation of silanols that produce ($SiOH_2^+$) groups, which are good leaving groups and act to increase the rate of condensation (Meixner *et al.*, 1999; Curran *et al.*, 1999).

The evolution of the silica structure was monitored by FT-IR spectroscopy. The spectra (Figure 5.5) recorded in the wavenumber region between 1400 cm^{-1} and 800 cm^{-1} show a broad peak at 1080 cm^{-1} due to the asymmetric stretching of Si-O-Si and a peak at around 950 cm^{-1} due to the stretching of Si-OH (Fidalgo *et al.*, 2001).

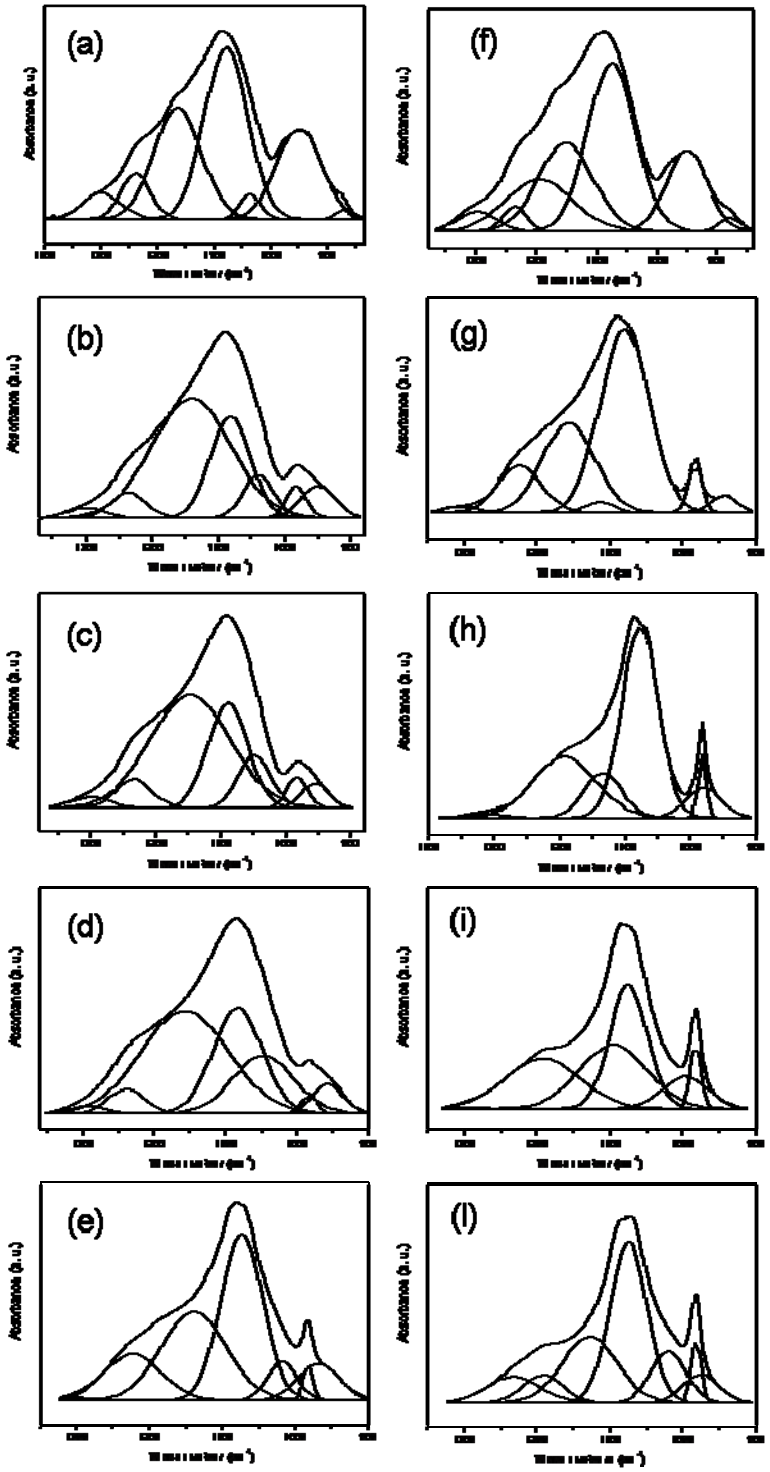

Figure 5.5 Deconvolution of the Si-O-Si and Si-OH stretching bands of the dried silica obtained at pH 5.45 (a), 6.83 (b), 7.64 (c), 9.38 (d), 10.38 (e) (density 1.03 g/cm^3) and pH 5.42 (f), 6.90 (g), 7.54 (h), 9.33 (i), 10.30 (l) (density 1.09 g/cm^3)

Infrared spectroscopy has been employed over the last three decades to investigate the structure and the defects on the chemical structure of silica gels. The 1080 cm^{-1} band has been largely used to obtain information on the Si-O-Si bond tensile strain (angle and length), porosity and density of silica (Sun *et al.*, 2005; Almeida *et al.*, 1990).

The Si-O-Si stretching vibration band can be deconvoluted in four or five peaks at around 1055 cm^{-1}, 1110 cm^{-1}, 1160 cm^{-1}, 1080 cm^{-1}, 1200 cm^{-1} (Lenza *et al.*, 200). According to the literature (Hench *et al.*, 1990), the 1080 cm^{-1} and 1055 cm^{-1} peaks correspond to transversal optical (TO) and longitudinal optical (LO) asymmetric stretching modes of Si-O-Si, respectively. The silica structure contains cyclic and linear structures. (Sun *et al.*, 2005). We assigned that the 1080 cm^{-1} and 1200 cm^{-1} vibrations of Si-O-Si belong to cyclic structures. The other peaks 1050 cm^{-1}, 1100 cm^{-1} and 1160 cm^{-1} are assigned to stretching vibrations of Si-O-Si belonging to a more linear less cross-linked structure (Lenza *et al.*, 200). It is clear that the wave numbers of the bands at 1080 cm^{-1} and 1055 cm^{-1} increase until pH 7 and decrease at higher pH (Table 5.3). The shift of both components to lower wave numbers is usually related to a more porous structure, larger Si-O-Si angles and Si-O bond lengths (Sun *et al.*, 2005). The evolution of the bands seem not to be influenced by the density of the metasilicate solution.

Table 5.3 Wave number of the Si-O-Si stretching modes

	pH	5.45	6.83	7.64	9.38	10.28
Density 1.03	$\upsilon_{Si\text{-}O\text{-}Si}$ (LO) (cm^{-1})	1078	1082	1088	1083	1074
	$\upsilon_{Si\text{-}O\text{-}Si}$ (TO) (cm^{-1})	1151	1157	1164	1156	1145
	pH	5.42	6.90	7.54	9.33	10.30
Density 1.09	$\upsilon_{Si\text{-}O\text{-}Si}$ (LO) (cm^{-1})	1075	1080	1078	1075	1075
	$\upsilon_{Si\text{-}O\text{-}Si}$ (TO) (cm^{-1})	1151	1157	1154	1152	1151

The development of the network can be also monitored by following the progression of the band due to the stretching of Si-OH (950-980 cm^{-1}). The bands at around 950 cm^{-1} and 980 cm^{-1} are due to stretching of SiO^- and SiOH, respectively. The deconvoluted spectra show clearly as increasing the pH, the band at 950 cm^{-1} decreases in intensity and disappears as well as the band at 980 cm^{-1} appears and its intensity increases. The infrared spectra of the composites in the region between 1400 cm^{-1} and 900 cm^{-1} show the same bands of the pure silica together with the characteristic bands of calcium phosphates detected by X-ray analyses. No shifts are been recorded (data not shown).

Scanning electron microscopy (SEM) was used to study texture and morphology of silica/calcium phosphate composite material. Scanning Electron Microscopy observation were done with Philips XL-20 scanning electron microscope.

Comparing the two densities, at the same pH values, any difference in the morphology was observed. However, samples texture and morphology appeared very different as a function of pH. Here we report only few representative examples.

In figure 5.6a is shown a brushite single crystal obtained at pH 5.42 using a metasilicate solution at 1.09 g/cm3 density. The crystal is about 20 μm long and 10 μm wide. The elongation of the crystal along one axis is in agreement with their preferential orientation supposed by the diffraction patterns analyses. The surface of the crystal appears strongly etched and characterized by the presence of channels and pores. The orientation of the channels reflects the growth direction of the crystal (figure 5.6b). We suppose that they hosted amorphous porous silica that is still partially present in the crystals. These crystals diffracted as a single crystal (data not reported). Figure 5.6c shows a single crystal of octacalcium phosphate precipitated at pH 9.33 using a metasilicate solution at 1.09 g/cm3 density. The crystal is 100 μm long and 60 μm wide. In figure 5.6d is reported a texture of the sample obtained at pH 10.30 using a metasilicate solution at density 1.09 g/cm3. The figure show plate like hydroxyapatite crystal and silica aggregates that covers and/or are embedded in the OCP crystal. This observation suggests that the OCP surface converts in HA plate-like crystals.

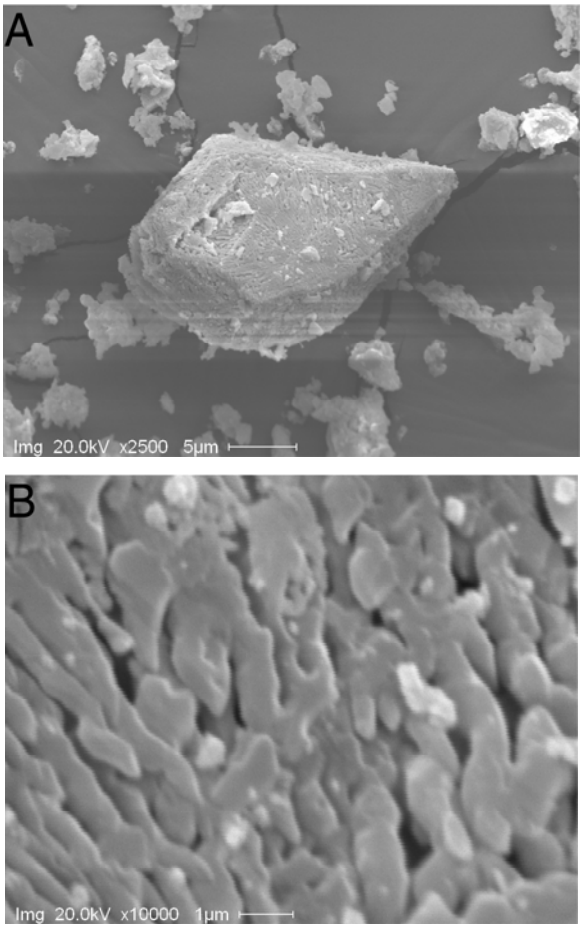

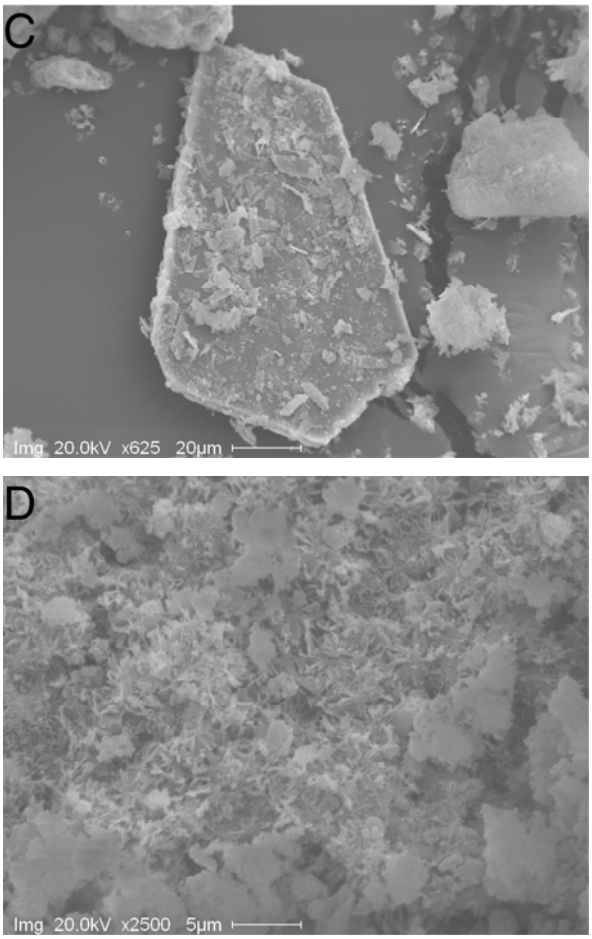

Figure 5.6 Scanning electron microscope (SEM) pictures of a) single crystal of brushite (pH 5.42 density 1.09 g/cm^3) (A), surface of the brushite crystal (pH 5.42 density 1.09 g/cm3) (B), single crystal of octacalcium phosphate (pH 9.38 density 1.09 g/cm^3) (C) and texture of the sample precipitated at pH 10.28 (density 1.09 g/cm^3) (D).

The TEM observations were performed on the samples obtained at the two highest pH values at each density. Transmission Electron Microscopy (TEM) investigations were carried out using a Philips CM 100 instrument (80 kV). The powdered samples were dispersed in water and then few droplets of the slurry deposited on holey-carbon foils supported on conventional copper microgrids. The figures 5.7a and b show crystals of HA and a crystal of OCP formed in a gel with 1.03 density and at pH of 9.38 and 10.28 respectively. HA appears as needle like100 nm long and 10 nm wide crystals that have tendency to aggregate along the long axis. The OCP crystal shows its almost perfectly aligned crystalline domains among which silica is intercalated. The silica appears as sponge-like material.

Figures 5.7c and 5.7d show the calcium phosphate crystals obtained at the two highest pH values using a metasilicate solution at density 1.09 g/cm^3. At pH 9.33 the HA nano-crystals appears

completely covered by unstructured materials and are almost not visible. The same images appears for the OCP crystal formed at pH 10.30.Comparing the figures is possible to observe that using the lower density the calcium phosphates result only partially covered instead using the higher density the crystals are completely covered by the silica.

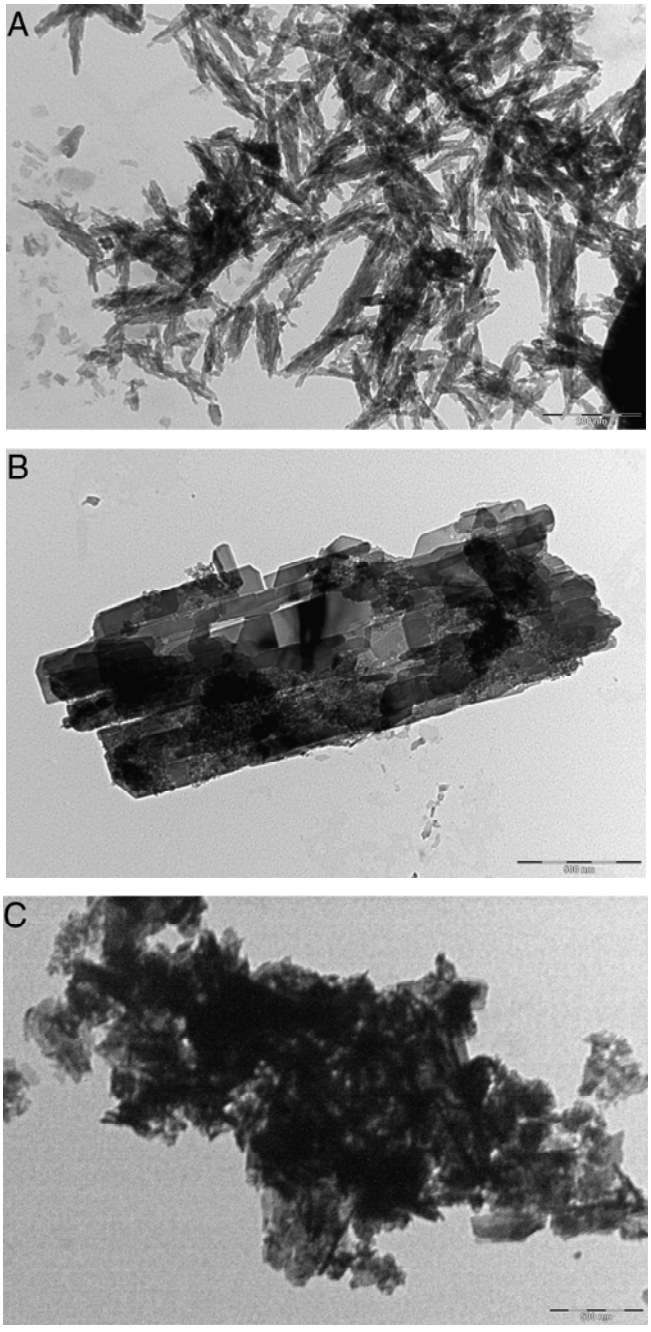

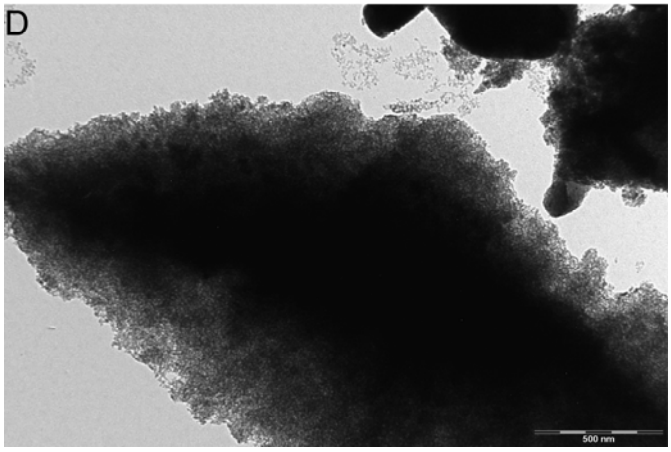

Figure 5.7 Transmission electron microscopy (TEM) images of calcium phosphates obtained at pH 9.38 (A), 10.38 (B) (density = 1.03 g/cm^3) and pH 9.33 (C), 10.30 (D) (d 1.09 g/cm^3).

5.4 CONCLUSIONS

In this work a simple method to crystallize different calcium phosphates phases is presented. The diffusion of a calcium chloride solution through a metasilicate gel set with phosphoric acid allows the specific precipitation of a calcium phosphate phase as function of pH and silica density.

The silica structure variation as a function of pH and silica density has been determined, above all in terms of silica pores volume and entrapped structural water. According to the literature, at fixed density, the silica "structuration", in terms of linear or randomly branched chains formation, presents a maximum at around pH 7 and two minima at extreme pH values. Subsequently, silica has larger pores at extreme pH, while is microporous at around pH 7. Increasing the experimental densities, an enhancement of the entrapped structural water has been observed. These findings, obtained for dried silica gels, have been correlated to the different calcium phosphates phases obtained as a function of gel pH and density. Experimental pH has allowed to discriminate between HA/OCP or DCP/DCPD, because of the different solubility of these phases. On the other hand, at fixed pH, experimental density has allowed to discriminate between HA and OCP, or between DCP and DCPD, due to the fact that HA and DCP are dehydrated phases and form in silica gels with a lower entrapped water content and thus more dried environment.

Simply combining the two parameters as pH and density, it is possible: to tailor silica structure, differentiate the calcium phosphate phase that can be crystallized, modulate the amount of silica covering the CaP nanocrystals. This method represents a straightforward, economic, and controllable system for obtaining functional composite biomaterials.

Moreover, this material could lead to significant improvements of the performances of implants in term of osteointegration, in possible association with the ability to deliver biologically active substances to the target tissues.

REFERENCES

- Almeida, R.; Pantano, C. *J. Appl. Phys.* **1990**, *68*, 4225.
- Altomare, A.; Burla, M. C.; Giacovazzo, C.; Guagliardi, A.; Moliterni, A. G. G.; Polidori, G.; Rizzi, R.; *J. Appl. Crystallogr.* **2001**, 34, 392.
- Andersson, J.; Areva, S.; Spliethoff, B.; Linden, M. *Biomaterials* **2005**, *26*, 6827.
- Beevers, C. A. *Acta Crystallogr.* **1958,** *11,* 273.
- Brinker, C. J.; Scherer, G. W. *The physics and chemistry of sol-gel processing*, Academic Press Inc., San Diego, CA, USA 1990.
- Curran, M. D.; Stiegman, A. E. *J. Non-Cryst. Solids* **1999**, *249*, 62.
- Curry, N. A.; Jones, D. W. *J. Chem. Soc. A* **1971**, *1971*, 3725.
- Diaz, A.; Lopez, T.; Manjarrez, J.; Basaldella, E.; Martinez-Blanes, J. M.; Odriozola, J. A. *Acta Biomaterialia* **2006**, *2*, 173.
- Dorozhkin, S.V.; Epple, M. *Angew. Chem. Int. Ed.* **2002**, *41*, 3130.
- Fidalgo, A.; Ilharco, L. M. *J. Non-Cryst. Solids* **2001**, *283*, 144.
- Hench, L. L.; Polak, J. M. *Science* **2002**, *295*, 1014.
- Hench, L. L.; West, J. K. *Chem. Rev.*, **1990**, *90*, 33.
- Hench, L. L.; Wheeler, D. L.; Greenspan, D. C. *J. Sol-Gel Sci. Technol.* **1998**, *13*, 245.
- Hill, R. J.; Howard, C. J. *J. Appl. Crystallogr.* **1987**, *20*, 467.
- Iler, R. K. *The chemistry of silica*, John Wiley & Sons, New York 1979.
- Johnsson, M. S. A.; Nancollas, G. H.*Crit. Rev. Oral Biol. M.* **1992**, *3*, 61.
- Jones, D. W.; Cruickshank, D. W. J. *Z. Kristallogr., Kristallgeom., Kristallphys., Kristallchem*. **1961**, *116*, 101.
- Koutsopoulos S. *J. Biomed. Mater. Res.* **2002**, *62*, 600.
- LeGeros, R. Z. *Calcium Phosphates in Oral Biology and Medicine. Monographs in Oral Sciences*; Myers, H., Ed.; Karger: Basel, 1991; Vol. 15.
- Lenza, R. F. S.; Vasconcelos, W. L. *Mater. Res.* **2001**, *4*, 175.
- Liesegang, R. E. *Naturwiss. Wochenschr.* **1896**, *11*, 353.
- López-Macipe, A.; Gómez-Morales, J.; Rodríguez-Clemente, R. *Adv. Mater.* **1998***, 10*, 49.

- Lowestan, H. A.; Weiner, S. *On Biomineralization,* Oxford University Press, New York 1989.
- McCusker, L. B.; Von Dreele, R. B.; Cox, D. E.; Louer, D.; Scardi, P. *J. Appl. Crystallogr*. **1999**, *32*, 36.
- Meixner, D. L.; Dyer, P. N. *J. Sol-Gel Sci. Technol.* **1999**, *14*, 223.
- Meyers, M. A.; Chen, P. Y.; Yu-Min Lin, A.; Seki, Y. *Progr. Mater. Sci.* **2008**, *53*, 1.
- Miyake, M.; Ishigaki, K.; Suzuki, T. *J. Solid State Chem.* **1986**, *61*, 230.
- Ning, C. Q.; Mehta, J.; El-Ghannam, A. *J. Mater. Sci. - Mater. Med.* **2005**, *16*, 355.
- Palazzo, B.; Iafisco, M.; Laforgia, M.; Margiotta, N.; Natile, G.; Bianchi, C. L.; Walsh, D.; Mann, S.; Roveri, N. *Adv. Funct. Mater.* **2007**, *17*, 2180.
- Roveri, N.; Palazzo, B.; Iafisco M. *Expert Opin. Drug Deliv.* **2008**, *5*, 861.
- Sanchez, C.; Hervé Arribart, H.; Guille, M. M. G. *Nat. Mater.* **2005**, *4*, 277.
- Sarikaya, M.; Tamerler, C.; Jen, A. K. Y.; Schulten, K.; Baneyx, F. *Nat. Mater.* **2003**, *2*, 577
- Slowing, I. I.; Trewyn, B. G.; Giri, S.; Lin, V. S. Y.; *Adv. Funct. Mater.* **2007**, *17*, 1225.
- Sousa, A.; Sousa, K. C.; Sousa, E. M. B. *Acta Biomaterialia* **2008, *4,*** 671.
- Sun, L. N.; Zhang, H. J.; Fu, L. S.; Meng, Q. G.; Peng, C. Y.; Yu, J. B. *Adv. Funct. Mater.* **2005**, *15*, 1041.
- Vallet-Regí, M.; Ruiz-González, L.; Izquierdo-Barba, I.; González-Calbet, J. M.; *J. Mater. Chem.* **2006**, *16*, 26.
- Veis, A. *Science* **2005**, *307*, 1419.
- Villacampa, A. I.; Garcia Ruiz, J. M. *J. Cryst. Growth* **2000**, *211*, 111.
- Zhan, J.; Tseng, Y.H.; Chan, J. C. C.; Mou, C.Y. *Adv. Funct. Mater.* **2005**, *15*, 2005.

CHAPTER 6
SURFACE ENAMEL REMINERALIZATION: HYDROXYAPATITE CRYSTALS VS FUORIDE IONS

6.1 STATUS OF THE ART

Dental erosion is the chemical wear of the dental hard tissue without the involvement of bacteria (Eccles, 1979). Its clinical relevance is becoming wider and wider (Deery *et al.*, 2000; Dugmor *et al.*, 2004; Al-Dlaigan *et al.*, 2001; Nunn *et al.*, 2003), and it is considered one of the main tooth pathologies able to cause patient discomfort, after periodontal diseases and caries.

Its aetiology is related to the enormous increase in consumption of soft drinks, fruit juices and sport drinks consumption. However, other acid sources such as drugs containing syrups, analgesics and vitamin C intake and environmental acid exposure in working conditions are claimed to be related to enamel erosion (Da Costa *et al.*, 2006; Kitchens *et al.*, 2007; Lussi *et al.*, 2006).

The mechanisms involved in the damage of dental hard tissue are the acid attacks on the outer few micrometers of the enamel, which brings to demineralization and dissolution of the mineral phase (West *et al*., 1998; West *et al.*, 1999; Hughes *et al.*, 1999).

Hydroxyapatite is the main constituent of the dental tissues representing in enamel and dentine the 95 wt % and 75 wt % respectively.

The primary determinant of dissolution rate is the solubility of hydroxyapatite (HA) which is related to pH and the presence of salivary pellicle also appears to be important (Amaechi *et al.*, 1999; Nekrashevych *et al.*, 2003).

Frequent application of a high concentration of topical fluoride may be of some benefit in preventing further demineralization and increasing the abrasion resistance of erosion lesions (Zero, 2005).

In vitro studies have shown that synthetic carbonated-hydroxyapatite (CHA) dissolution inhibition is a logarithmic function of the fluoride concentration in solution (Featherstone *et al.*, 1990).

Systemic intake of fluoride during tooth formation has been claimed to be effective in caries prevention just by means of the apatite demineralization inhibition. According to RDA (Recommended Daily Allowances) panel of European Food Safety Authority, an intake of 0.1mg fluoride/Kg body weight/day in children up to the age of eight years can be considered as the dose below which there will be no significant occurrence of moderate forms of fluorosis in permanent teeth.

However it is important to consider that fluoridated water, fluoride supplements in diet, fluoride toothpastes and topical fluoride applications have been identified as sources of enamel fluorosis

(Pendrys *et al.*, 1990). Moreover, the "probably toxic dose" of fluoride - the dose which should trigger therapeutic intervention and hospitalization- is 5 mg/Kg of body weight, but as currently packaged, many dental products contain sufficient fluoride to exceed the "probably toxic dose" for young children (Whitford, 1990).

Most of the products and devices used to contrast enamel and dentine erosion such as fluoride (Ganss *et al.*, 2001; Ganss *et al.*, 2004; Wiegand *et al.*, 2003), behave by reducing apatite dissolution rather than aiming to promote mineralization through apatite crystallization or replacement of the lost mineral. Hydroxyapatite, as well as in bone, is responsible for the mechanical behaviour of the dental tissues. Unlike bone, in enamel and dentine, when HA is dissolved or abraded, it cannot spontaneously remineralize because enamel contains no cells and dentine apposition occurs only towards the pulp tissues. Therefore both enamel and dentine can be reconstructed only by the application of alloplastic materials providing a sort of prosthetic restoration. In view of this situation, the demineralized area and micrometric sized scratches, which normally occur on enamel surface as a consequence of micro wear and acid attack (Teaford, 1988), cannot be repaired biologically, nor prosthetically.

Hydroxyapatite has been widely subjected to experiment as bone filler and prosthetic coating due to its biocompatibility and osteo-conductivity, representing an elective material covering a wide range of applications for bone substitution and interface. Poorly crystalline HA nanocrystals, in addition to the excellent biological properties of HA, such as non-toxicity and lack of inflammatory and immunitary responses, have bio-resorption properties under physiological conditions. This property can be modulated by modifying its degree of crystallinity, which is achieved by implementation of innovative synthesis with a nanosize crystals control. In the last decade advanced technology has been utilized to synthesize a new generation of biomimetic apatitic alloplastic materials which can optimize the interaction with biological entities thanks to their strong surface bioactivity (Palazzo *et al.*, 2007).

6.2 AIM OF THE WORK

The aim of the present study is the design of biomimetic carbonate-hydroxyapatite nanocrystals in order to obtain a new remineralization method of the altered enamel surfaces, highlighting the effect of the hydroxyapatite crystals respect the fluoride ions into the remineralization in vitro of human enamel surface.

6.3 SYNTHESIS AND CHARACTERISATION OF BIOMIMETIC CARBONATE-HYDROXYAPATITE NANOCRYSTALS

Biomimetic carbonate-hydroxyapatite nanocrystals have been synthesized with a nearly stoichiometric in bulk Ca/P molar ratio of about 1.6-1.7 and containing 4 ± 1 wt% of carbonate ions replacing prevalently phosphate groups. CHA nanocrystals have been synthesized both about 100 nm and 20 nm sized with an acicular and plate morphology respectively. Plate-acicular shaped carbonate-hydroxyapatite nanocrystals about 100 nm in size, were synthesized according to a modification of method previously reported (Landi *et al.*, 2000) and patented (Guaber *et al.*, 2006). CHA nanocrystals about 100 nm in size were precipitated from an aqueous suspension of $Ca(OH)_2$ (0.17 M) by slow addition of H_3PO_4 (0.15 M). The reaction mixture was stirred at 37 °C for 12 hours, and then stirring was suspended allowing the deposition of CHA nanocrystals. Synthesized CHA 100 nm sized nanocrystals were isolated by filtration of the mother liquor, repeatedly washed with water and freeze-dried. The fraction of plate-acicular shaped crystals about 100 nm in size with a granular dimensions ranging from 100 to 150 μm was selected for the study. Aliquot of plate-acicular shaped crystals about 100 nm in size have been allowed, after synthesis to intergrowth in the reaction mixture up to the formation of clusters having dimension ranging from about 0.5 to3.0 μm. The cluster aggregation process has been stopped by adding a surfactant (Protelan MST35 8% wt) in the mother solution.

Plate shaped carbonate-hydroxyapatite nanocrystals about 20 nm sized were synthesized according to the method of Liou et al. (Liou *et al.*, 2004) with some modifications. The nanocrystals were precipitated from an aqueous solution of $(NH_4)_3PO_4$ (5.1 mM) by slow addition of an aqueous solution of $Ca(CH_3COO)_2$ (8.5 mM) keeping the pH at a constant value of 10 by addition of a NH_4OH solution. The reaction mixture was kept under stirring at room temperature for 24 hours, and then stirring was suspended allowing the deposition CHA nanocrystals. Synthesized CHA nanocrystals were isolated by filtration of the solution, repeatedly washed with water, and freeze-dried. The fraction of plate shaped crystals about 20 nm in size having granular dimensions ranging from 100 to 150 μm was selected for the study.

TEM images of synthetic 20 nm sized CHA nanocrystals showing the plate shaped morphology and synthetic 100 nm sized CHA nanocrystals showing the acicular morphology are reported in figure 6.1a and 6.1b respectively. Transmission Electron Microscopy (TEM) investigations were carried out using a Philips CM 100 instrument. The powdered samples were ultrasonically dispersed in ultra pure water and then a few droplets of the slurry deposited on holey-carbon foils supported on conventional copper microgrids.

CHA nanocrystals can aggregate in micro sized crystal clusters, whose dimensions increase prolonging maturation time in mother solution at constant temperature and stirring .

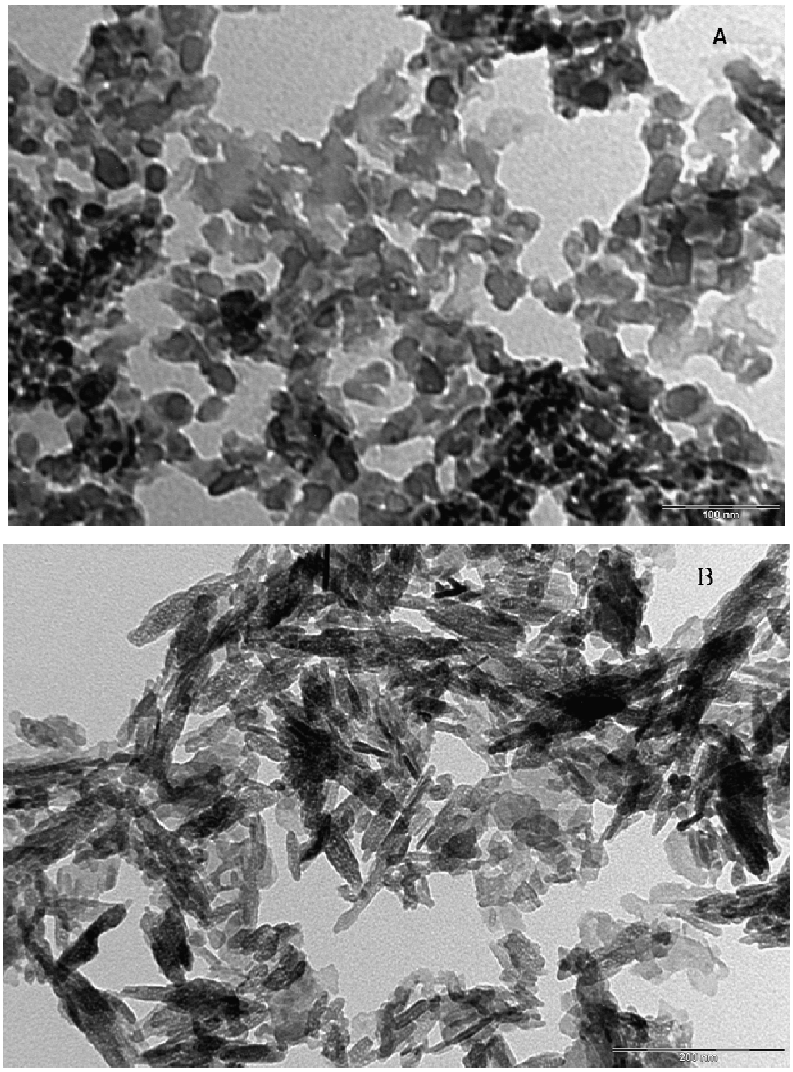

Figure 6.1 TEM images of synthetic plate-shaped 20 nm sized CHA nanocrystals (a), synthetic plate-acicular 100 nm sized CHA nanocrystals (b) (scale bars = 200 nm).

Powder X-ray diffraction patterns of plate shaped about 20 nm sized CHA nanocrystals and acicular shaped about 100 nm sized CHA nanocrystals (Figure 6.2b and 6.2c respectively) show characteristic diffraction maxima of an apatite single phase (JCPDS 01-074-0565).

X-ray diffraction powder and enamel surface patterns were collected using an Analytical X'Pert Pro equipped with X'Celerator detector powder diffractometer using Cu Kα radiation generated at 40 kV and 40 mA. The instrument was configured with a 1° divergence and 0.2 mm receiving slits. The samples were prepared using the front loading of standard aluminium sample holders which are 1 mm deep, 20 mm high and 15 mm wide. The degree of HA crystallinity was evaluated according to the formula (Erkmen, 1999):

$$Crystallinity = \left(\frac{X}{Y}\right)100$$

where X = net area of diffracted peaks, and Y = net area of diffracted peaks + background area. Crystal domain size along the c direction was calculated applying Scherrer's formula:

$$L_{(002)} = \frac{0.94\lambda}{\left[\cos\theta(\sqrt{\Delta r^2 - \Delta_0{}^2})\right]}$$

where θ is the diffraction angle for plane (002), Δr and Δ_0 the widths in radians of reflection (002) at half height for the synthesized and the reference HA materials, respectively, and λ=1.5405 Å.

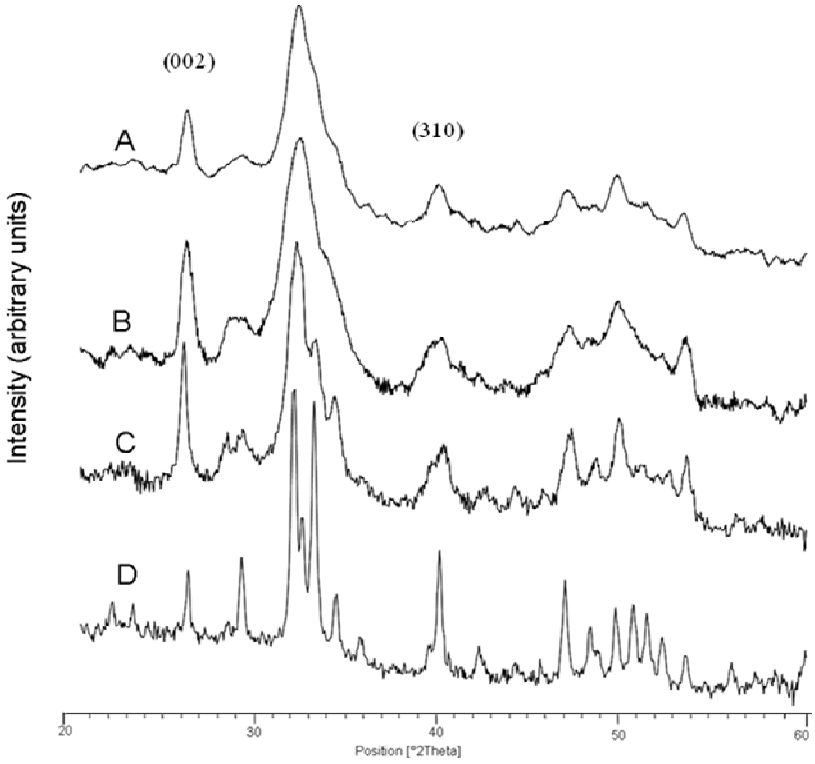

Figure 6.2 X-ray diffraction patterns of natural carbonate-hydroxyapatite from deproteined dentine (a), synthetic plate shaped 20 nm sized CHA nanocrystals (b), synthetic plate-acicular shaped 100 nm sized CHA nanocrystals (c), and natural carbonate-hydroxyapatite from enamel (d).

These X-ray diffraction patterns are compared with those collected for natural carbonate hydroxyapatite from deproteined dentine and enamel reported in figure 6.2a and d respectively. The broadening of the diffraction maxima present in the X-ray diffraction patterns reported in figure 6.2 (a, b, c) indicate a relatively low degree of crystallinity, which was quantified according to previous (Erkmen, 1999). The degree of crystallinity of synthesized about 20 nm sized CHA nanocrystals with plate morphology and synthesized about 100 nm sized CHA nanocrystals with acicular

morphology is 30% and 50% respectively. The crystallinity degree of about 20 nm sized CHA nanocrystals is very close to that one determined from the X-ray diffraction pattern of deproteined dentine natural carbonate-hydroxyapatite (28%) reported in figure 6.2a. Furthermore the crystallinity degree of natural hydroxyapatite of deproteined enamel, reported in figure 6.2d is 70%. The crystal domain sizes along the c direction have been calculated by the Scherrer's formula using the 2θ=26° (002) diffraction peak of the X-ray diffraction patterns reported in figure 6.2 a, b, c. The calculated crystal domain sizes for 20 nm sized CHA nanocrystals and deproteined dentine are 250 Å and 213 Å respectively. These results obtained by X-ray diffraction investigation reveal that the crystal structures of the synthesized CHA nanocrystals are very close to that observed for natural dentine.

The same similarity can be observed from the comparison of the FTIR spectra of synthesized CHA nanocrystals and natural apatite of deproteined dentine reported in Figure 6.3a and b respectively. In these spectra the characteristic absorption bands of phosphate and carbonate groups are clearly resolved. ATR-IR spectra were recorded on a Thermo Nicolet 380 FT-IR spectrometer equipped with a commercial ATR accessory.

The infrared spectra were registered from 4000 to 400 cm^{-1} at 2 cm^{-1} resolution using a Bruker IFS 66v/S spectrometer using KBr pellets. ATR spectra were recorded with the cell empty to be used as a blank for subsequent experiments. Samples were made by placing the powder sample onto the Ge ATR crystal. Spectra were collected by averaging 32 scans at 4 cm^{-1} resolution.

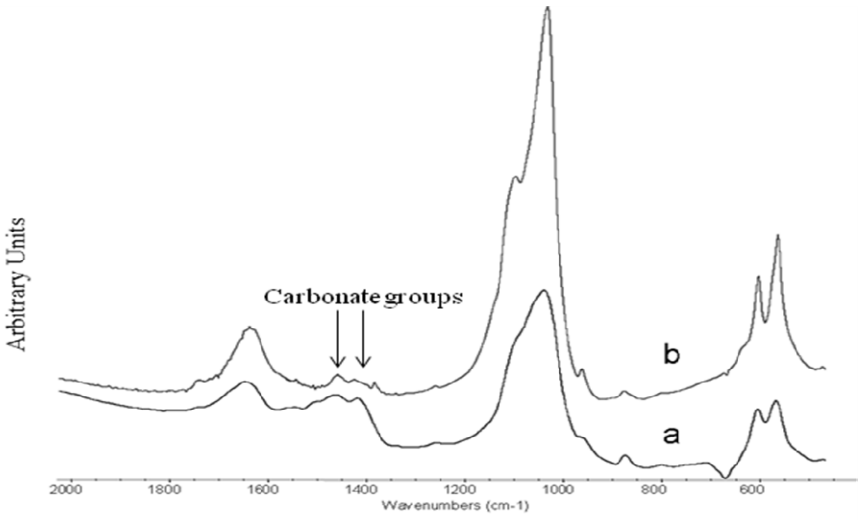

Figure 6.3 FTIR spectra of synthetic 20 nm sized CHA nanocrystals (a), natural carbonate-hydroxyapatite from deproteined dentine (b).

The absorption band at 1468 cm^{-1} is related to the carbonate group substitution to the phosphate one, while the shoulder at 1545 cm^{-1} can be considered the contribution of the carbonate group substituting the hydroxyl group in the apatite structure. This finding reveals that synthesized CHA nanocrystals not only contain a similar carbonate amount, but also, underline that the carbonate substitution to the phosphate and /or hydroxyl group is very similar in the synthetic and biological crystals.

A surface characterization of the synthetic carbonate-hydroxyapatite nanocrystals has been carried out in order highlight their surface chemical-physical characteristic which directly interfaces and reacts with exposed dental tissues. The ATR spectra (data not shown) of the synthetic about 20 nm and 100 nm sized CHA nanocrystals reveal a 4% and 3% wt surface carbonate respectively. The consistent amount of surface of carbonate percentage present in synthetic CHA is appreciably higher than the surface carbonate percentage present in enamel and dentine about 2 % wt.

Specific surface area of 100 m^2g^{-1} and 80 m^2g^{-1} has been determined for 20 nm sized CHA nanocrystals with plate morphology and synthesized 100 nm sized CHA nanocrystals with acicular morphology respectively. These specific surface area values obtained for synthetic nanocrystals are only slightly lower than the 110 m^2g^{-1} obtained for biological nanocrystals.

The surface Ca/P molar ratio determined by XPS analysis for CHA nanocrystals and CHA crystals micro-clusters do not reveal appreciably differences and result significantly lower than Ca/P molar ratio determined by ICP analysis in bulk indicating a surface calcium deficiency probably due to surface disorder. In fact the Ca/P molar ratios of 1.7 determined in bulk for synthetic CHA nanocrystals reduces to a value of 1.4 -1.5 when determined on the crystals surface by XPS analysis (Table 6.1). XPS analyses were performed in an M-Probe Instrument (SSI) equipped with a monochromatic Al Kα source (1486.6 eV) with a spot size of 200 × 750 μm and pass energy of 25 eV, providing a resolution for 0.74 eV. With a monochromatic source, an electron flood gun was used to compensate the build up of positive charge on the insulator samples during the analyses. 10 eV electrons were selected to perform measurements on these samples. The accuracy of the reported binding energies (BE) was estimated to be ± 0.2 eV. The quantitative data were also accurately checked and reproduced several times (at least ten times for each sample) and the percentage error was estimated to be ± 1%. Calcium and phosphorus contents were measured using Inductively Coupled Plasma (ICP) Optical Emission Spectrometry (OES) using a Perkin Elmer Optima 4200 DV.

XPS analysis of spectral features of the O 1*s* region of the synthetic 100 nm sized CHA nanocrystals (Figure 6.5c) shows a definite O 1*s* shape fitted by three components: a first, very intense, peak at lower BE attributed to oxygen in phosphate group, a second peak due to OH of the

carbonate-hydroxyapatite and a final peak at very high BE, which can be attributed to trapped undissociated water and carbonates.

6.4 IN VITRO ENAMEL SURFACE REMINERALIZATION BY BIOMIMETIC CARBONATE HYDROXYAPATITE NANOCRYSTALS VS FLUORIDE IONS

Slabs of enamel (3x3mm) were obtained from interproximal surfaces of premolars extracted for orthodontic reasons. After the extraction, the teeth were cut with diamond disks and the obtained slabs were sonicated for 10 min in 50% ethanol in order to remove any debris. Then the specimens were etched with 37% phosphoric acid for 1 min. Etched slabs were washed in distilled water for 10 minutes under stirring and then air dried. Two different in vitro remineralization procedures have been performed.

The first *in vitro* remineralization procedure utilises a 10% wt CHA in range 100 to 150 μm granules slurries constituted of both 20 nm or 100 nm sized nanocrystals. CHA nanocrystals aqueous slurries were applied for 10 min on the surfaces of the enamel slabs at room temperature with 100% relative humidity and then removed by water washing and air dried.

The second *in vitro* remineralization process utilises toothpastes containing booth fluoride ions or CHA 0.5-3.0 μm sized clusters constituted by intergrowth of 100 nm sized nanocrystals.

Comparable etched enamel slabs were divided into 3 groups of treatment using respectively fluoride or CHA based toothpaste and only water (control). Each slab was brushed three times a day for a period of 15 days. The intervals between brushing sessions were at least 5 hours. Every brushing session has been performed for 30 sec by an electric toothbrush using constant pressure and a bean sized toothpaste aliquot wetted with tap water, closely resembling the in vivo usual tooth brushing procedure. After every treatment, the single enamel slab was washed with tap water using a cleaned toothbrush in order to remove residual toothpaste.

SEM analysis allows investigating the morphology of both demineralized enamel and the features observed after remineralization procedures induced by biomimetic CHA nanocrystals *in vitro* application.

The demineralization procedure by ortophosphoric acid 37% for 1 minute removes the aprismatic enamel and exposed hydroxyapatite prisms became evident. figure 6.4a shows demineralization of both interprismatic and prismatic enamel structures.

After treatment for 10 minutes by aqueous slurry of both synthetic 20 nm and 100nm sized CHA nanocrystals, the surface of the demineralized enamel appears covered by the CHA phase (Figure 6.4b and 6.4c respectively) arranged in a thick and homogeneous apatitic layer.

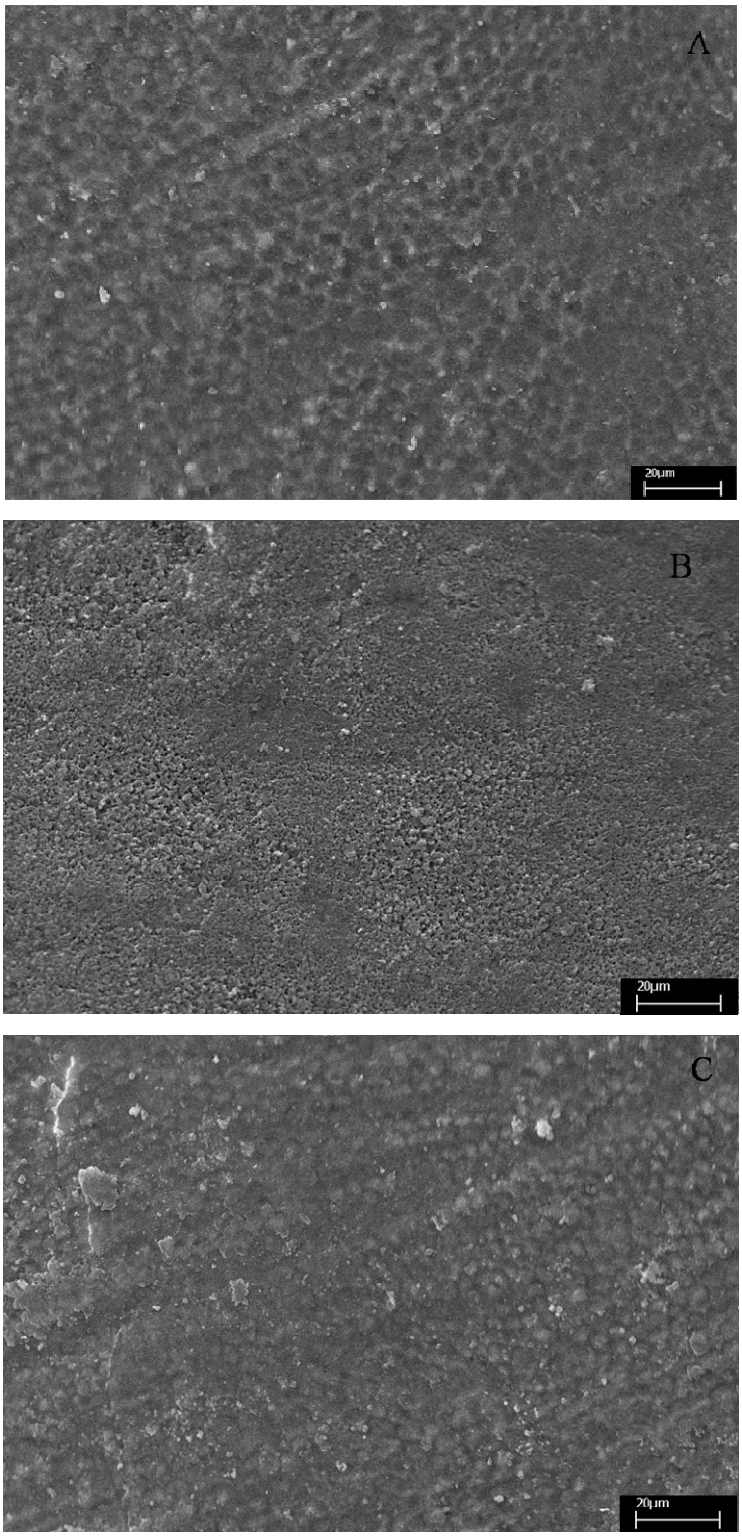

Figure 6.4 SEM image of enamel surface after application of 37% ortophosphoric acid for 1 min. The etching treatment removed aprismatic layer and exposed prismatic and interprismatic hydroxyapatite structures (a), remineralized enamel surface after treatment by synthetic CHA micro-clusters constituted of nanocrystals 20 nm (b) and 100 nm sized (c) and synthetic CHA micro-clusters.

XPS analysis of spectral features of the O 1*s* region of the enamel demineralized by ortophosphoric acid 37% for 1 minute shows a single broad band, in which it is difficult to determine precisely and to quantify the binding energy (BE) and, therefore, the kind of the surface oxygen components (Figure 6.5a). On the contrary the enamel remineralized by synthetic 100 nm sized CHA nanocrystals for 10 minutes show a definite O *1s* shape fitted by three components at different binding energy (Figure 6.5b). These components correspond to the same three ones used to fit O *1s* shape recorded for synthetic 100 nm sized CHA nanocrystals (Figure 6.5c): the first at lower BE very intense peak is attributed to oxygen in phosphate group, the second peak is due to OH of the carbonate-hydroxyapatite and a final peak at high BE, can be attributed to trapped undissociated water and carbonate groups.

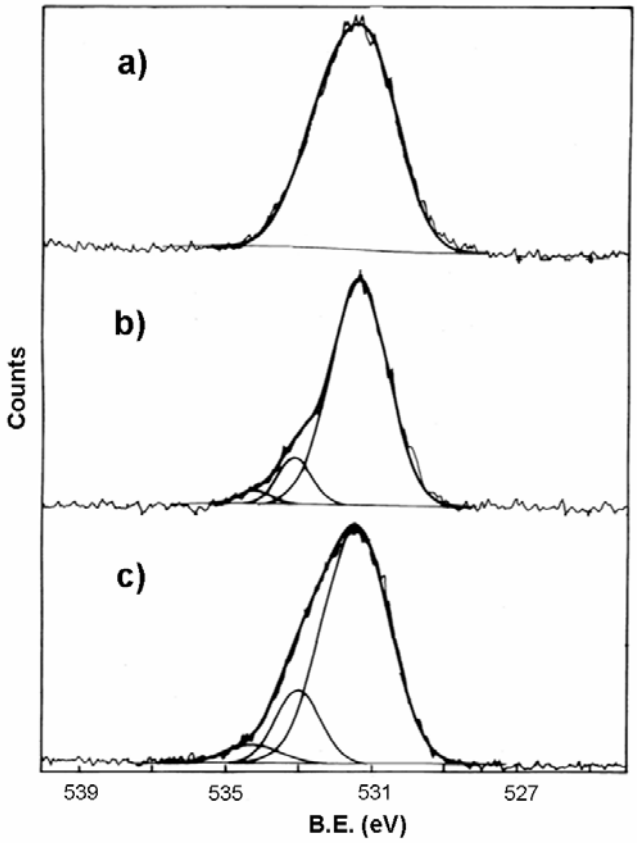

Figure 6.5 XPS analysis of spectral features of the O 1*s* region of the enamel demineralized by ortophosphoric acid 37% for 1 minute (a), enamel remineralizated by a treatment with synthetic micro clusters of CHA nanocrystals 100 nm sized for 10 minutes (b), and synthetic micro clusters of CHA nanocrystals 100 nm sized (c).

These results unequivocally confirm the presence of synthetic CHA at the surface of the treated enamel and the consequent validation of the enamel remineralization. The same finding is pointed

out by the ATR spectrum of enamel treated for 10 minutes by synthetic 100 nm sized CHA nanocrystals, showing appreciable higher intensity of the characteristic absorption bands of carbonate ions (1420-1460 and 1680 cm^{-1}) in respect of the same absorption bands present in the demineralized enamel ATR spectrum. No differences are appreciable in the phosphate ions bands (1000-1100 and 530-580 cm^{-1}). ATR spectrum (data not shown) of remineralized enamel reveals that surface apatite is richer in carbonate than natural one, such as synthetic 100 nm sized CHA nanocrystals.

SEM analysis allowed us to investigate the morphology of both demineralized enamel and the features observed after a remineralization process which utilises in vitro application of toothpastes containing either fluoride or CHA micro-clusters constituted of 100 nm in size nanocrystals.

The surfaces of the teeth treated with fluoride (Figure 6.6b) were not consistently changed respect to that of demineralization by ortophosphoric acid (Figure 6.6c). Actually both the interprismatic and prismatic enamel structures appear still evident. On the contrary after treatment of the enamel slabs with a toothpaste containing synthesized CHA micro-clusters constituted of 100 nm sized nanocrystals the interprismatic and prismatic enamel structures appear to be completely hidden by a thick homogeneous apatitic layer (Figure 6.6a).

The XRD patterns collected on the surface of enamel slabs after treatment with CHA or fluoride tooth-pastes and water are recorded and compared with the XRD pattern of CHA micro-clusters constituted of 100 nm sized nanocrystals utilized to prepare the used CHA toothpaste (data not shown). The XRD diffraction maxima recorded on the surface of enamel slabs treated with fluoride containing toothpaste appear slightly more sharpened than those obtained on the enamel etched slabs brushed only with water. This observation reveals an increased crystallinity degree probably due to a partial structural conversion of hydroxyapatite into fluoride substituted hydroxyapatite. On the contrary, the XRD pattern obtained on the surface of enamel slabs brushed with CHA containing tooth-paste shows the broadened diffraction maxima characteristic of the synthetic biomimetic CHA, revealing its presence on the enamel surface. The CHA not removed by brushing procedures suggests the formation of chemical bonds between the synthetic CHA micro-clusters constituted of 100 nm sized nanocrystals and natural enamel apatite crystals. These bonds allow the formation of a persistent CHA coating on the enamel surface whose morphology was detected by SEM analysis.

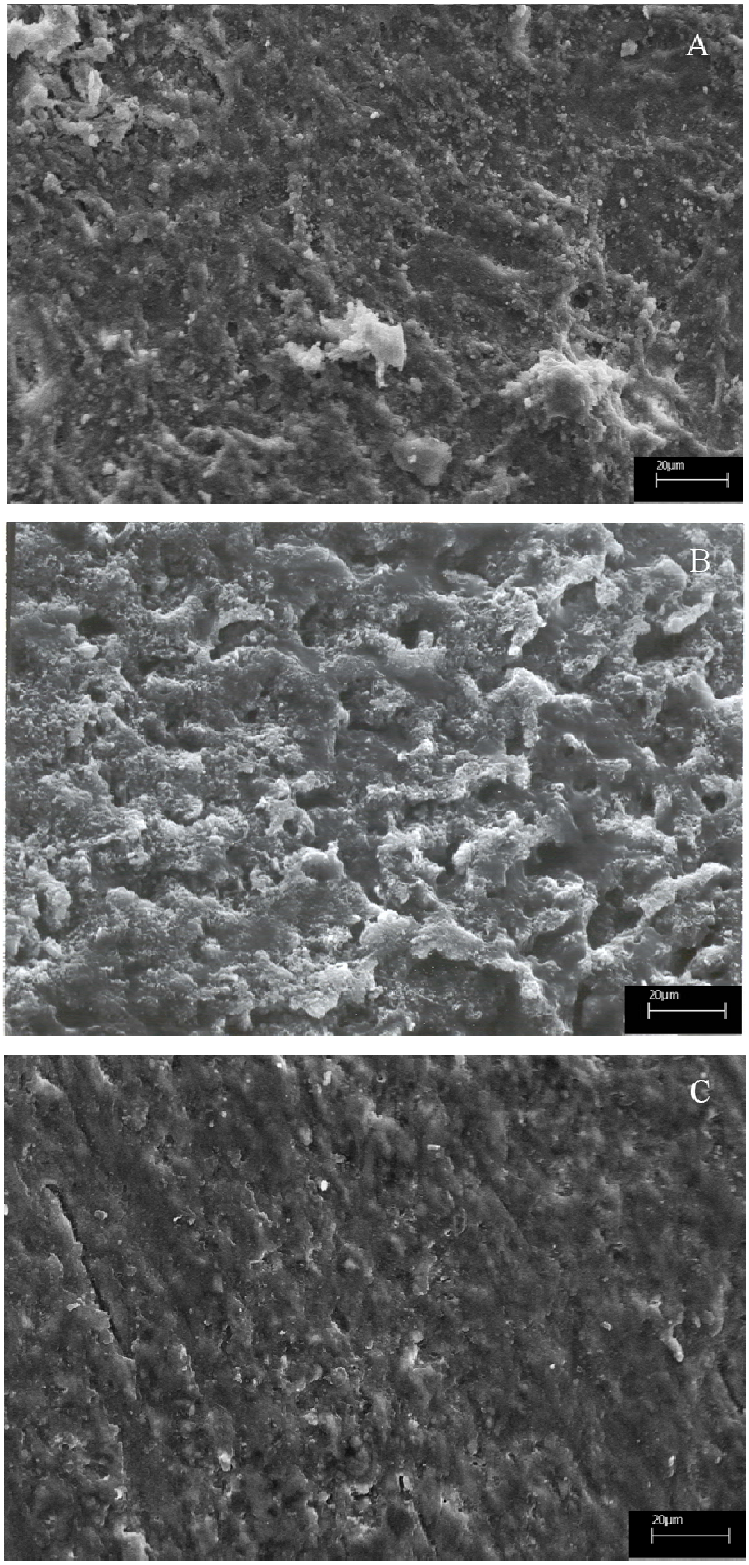

Figure 6.6 SEM images of enamel after brushing treatment with: a) CHA toothpaste containing (b), fluoride containing toothpaste and (c) ortophosphoric acid application.

The surface Ca/P molar ratio determined by XPS analysis for demineralized enamel slabs before and after in vitro remineralization by brushing whit toothpastes containing either fluoride or CHA

are compared in table 6.1. In this table a comparison with the Ca/P molar ratio of CHA micro-clusters constituted of 100 nm sized nanocrystals also present.

Table 6.1 XPS analysis of CHA nanocrystals, enamel tooth treated with ortophosphoric acid before and after treatment with either CHA 20 or 100 nm sized nanocrystals and after brushing with toothpastes containing booth CHA or fluoride.

Sample	O (%)	C (%)	Ca (%)	P (%)	N (%)	Si (%)	Na (%)	F (%)	Ca/P
20 nm CHA nanocrystals	50.4	17.6	19.4	12.6	-	-	-	-	1.5
100 nm CHA nanocrystals	48.4	18.0	19.6	13.9	-	-	-	-	1.4
Tooth treated with ortophosphoric acid	30.7	49.4	5.4	5.3	5.9	1.9	1.4	-	1.1
Tooth treated with 20 nm CHA nanocrystals	43.3	27.3	13.4	10.1	2.3	-	1.9	-	1.3
Tooth treated with 100 nm CHA nanocrystals	43.7	26.0	14.8	11.2	1	-	1.5	-	1.3
CHA containing toothpaste	30.7	51.9	5.5	4.7	1.6	5.6	0.0	-	1.2
fluoride containing toothpaste	20.9	63.3	4.1	1.2	2.0	4.9	-	3.6	3.4

The enamel surface Ca/P molar ratio changes before and after the brushing treatment with toothpastes containing fluoride, assuming a value of 3.4 very different from the apatite stoichiometric one (Ca/P=1.7).This finding reveals that the only structural modification of enamel hydroxyapatite induced by fluoride is restricted to a partial hydroxyl groups replacement by fluoride ions without affecting appreciably the Ca and phosphate structural network. On the contrary enamel slabs treated with the toothpaste containing synthesised CHA micro-clusters of 100 nm sized nanocrystals exhibit a surface Ca/P molar ratio very similar to that one of the synthetic CHA.

This coating is highly less crystalline than native enamel apatite, and consists of a new apatitic mineral deposition which progressively fills the scratches and pits. On the contrary, the surface remineralisation observed on the specimens treated with fluoride containing toothpaste, is mainly

based on chemical-physical enamel apatite surface modifications rather than a formation of a new mineral deposition.
The CHA biomimetic coating formation is a remineralization process corresponding to a new apatite deposition in the demineralized area of enamel surface.

6.5 CONCLUSIONS

Enamel is the hardest and most mineralized tissue of human body. It is structured in order to resist to mechanical injuries, abrasion and chemical attack. Differently from all the other mineralized tissues, it lacks of proteins even if they are essential to its formation. Actually, matrix proteins are cleaved by proteinases secreted by the ameloblasts during tooth formation; hence, the matrix proteins of enamel are not incorporated into enamel prisms (Simmer *et al.*, 1995). Degradation and resumption of enamel matrix proteins is the reason why enamel prisms, once formed, cannot be remodelled. After enamel prism formation only the amount of hydroxyapatite within the prisms may decrease in consequence of chemical changes into the oral environment.
Acid attack is one of the major causes of enamel hydroxyapatite loss. It may occur even in young age as a consequence of plaque metabolism or simply due to food and beverage intakes [2-4].
In the present study synthetic carbonate-hydroxyapatite biomimetic nano-crystals have been chemical-physical characterized and investigated regarding the possibility to obtain an *in vitro* remineralization of the altered enamel surfaces.
The experimental model used in the present investigation was the demineralization by means of ortophosphoric acid of sound enamel of the interproximal surfaces and its subsequent remineralization.
This model was chosen because the demineralizing effect of ortophosphoric acid is well known in terms of chemical and micro-histological features because it is an essential part of the procedures of adhesive restoration applications.
The SEM observations showed that the enamel is characterized by both amorphous and prismatic hydroxyapatite and by an irregular surface even. The use of ortophosphoric acid causes an exposure of prism and a loss of both interprismatic and prismatic substances.
The treatment of demineralized enamel only for ten minutes, by synthetic CHA nanocrystals, induces a consistent enamel remineralization through the formation of a surface carbonate-hydroxyapatite coating. This coating is due to the chemical bond of the synthetic CHA nanocrystals biomimetic for composition, structure, size and morphology on the surface prismatic hydroxyapatite enamel. It can be supposed that the application of CHA nanocrystals 20 nm sized allows a better

mineralization in the lower surface fissure, because the interprismatic and prismatic enamel structures appear totally hidden. Using an equal time of treatment, the application of CHA nanocrystals 100 nm sized produce the formation of a homogeneous coating which hides interprismatic and prismatic enamel structures when examined with SEM.

In this work an *in vitro* enamel surface remineralization by brushing with toothpastes containing either fluoride or biomimetic CHA nanocrystals micro-clusters has been also carried out. The XRD patterns, SEM images and XPS spectra collected on the surface of enamel slabs before and after treatment with CHA or fluoride toothpastes underline the possibility to obtain an enamel remineralization through the formation of a surface apatite coating which covers the enamel structure avoiding the most probably health dangerous fluoride effects, to contrast the mechanical abrasion and acid attacks to which tooth enamel is exposed. The documented CHA biomimetic coating formation which is less crystalline than enamel natural apatite represents an enamel repair process corresponding to an apatite deposition inside the demineralised area of enamel surface and may be considered an innovative approach to contrast enamel demineralization.

REFERENCES

- Al-Dlaigan, Y. H.; Shaw, L.; Smith, A. *Brit. Dent. J.* **2001**,*190*, 145.
- Amaechi, B. T.; Higham, S. M.; Edgar, W. M.; Milosevic, A. *J. Dent. Res.* **1999**, *78*, 1821.
- Da Costa, C. C.; Almeida, I. C.; Costa Filho, L. C. *Int. J. Paediatr. Dent.* **2006**, *16*,174.
- Deery, C.; Wagner, M. L.; Longbottom, C.; Simon, R.; Nugent, Z. J. *Pediatr. Dent.* **2000**, *22*, 505.
- Dugmor, C. R.; Rock, W. P. *Brit. Dent. J.* **2004**, *196*, 279.
- Eccles, J. D. *J. Prosthet. Dent.*, **1979**, 24, 649.
- Erkmen, Z. E. *J. Biomed. Mater. Res.* **1999**, *48*, 861.
- Featherstone, J. D. B.; Glena, R.; Shariati, M.; Shields, C. P. *J. Dent. Res.* **1990**, *69*, 620.
- Ganss, C.; Klimek, J.; Brune, V.; Schurmann, A. *Caries Res.* **2004**, *38*, 561.
- Ganss, C.; Klimek, J.; Schaffer, U.; Spall, T. *Caries Re*s. **2001**, *35*, 325.
- Guaber S.p.A., Gazzaniga, G.; Roveri, N.; Rimondini, L.; Palazzo, B.; Iafisco M.; Gualandi P. EU Patent 005146, 2006.
- Hughes, J. A.; West, N. X.; Parker, D. M.; Newcombe, R. G.; Addy, M. *J. Dent.* **1999**, *27*, 285.

- Kitchens, M.**;**Owens, B. M. *J. Clin. Ped. Dent.* **2007**, *31*, 153.
- Landi, E.; Tampieri, A.; Celotti, G.;Sprio, S. *J. Europ. Cer. Soc.,* **2000**, **20**, 2377.
- Liou, S. C. , Chen, S. Y. , Lee, H. Y.; Bo, J. S. *Biomaterials* **2004**, *25*, 189.
- Lussi, A.; Hellwig, E.; Zero, D.; Jaeggi, T. *Am. J. Dent.* **2006**, *19*, 319.
- Nekrashevych, Y.; Stosser, L. *Caries Res.* **2003**, *37*, 225.
- Nunn, J. H.; Gordon, P. H.; Morris, A. J.; Pine, C. M.; Walker, A. *Int. J. Paediatr. Dent.* **2003**, *13*, 98.
- Palazzo, B.; Iafisco, M.; Laforgia, M.; Margiotta, N.; Natile, G.; Bianchi, C. L.; Walsh, D.; Mann, S.; Roveri, N. *Adv. Funct. Mater.* **2007**, *17*, 2180.
- Pendrys, D. G.; Stamm, J. W. *J. Dent. Res.* **1990**, *69*, 529.
- Simmer, J. P.; Fincham, A. G. *Crit. Rev. Oral Biol. M.* **1995**, *6*, 84.
- Teaford, M. F. *Scanning Microscopy*, **1988**, *2*, 1149.
- West, N. X.; Maxwell, A.; Hughes, J. A.; Parker, D. M.; Newcombe, R. G.; Addy, M. *J. Dent.* **1999**, *27*, 341.
- West, N. X.; Maxwell, A.; Hughes, J. A.; Parker, D. M.; Newcombe, R. G.; Addy, M. *J. Dent.* **1998**, *26*, 329.
- Whitford, G. M. **1990**, *69*, 539.
- Wiegand A.; Attin, T. *Oral Health Prev. Dent.* **2003**, *1*, 245.
- Zero, D. T. *Int. Dent. J.* **2005**, *55*, 285.

LIST OF PUBBLICATIONS

1) Palazzo Barbara, Walsh Dominic, **Iafisco Michele**, Foresti Elisabetta, Bertinetti Luca, Martra Giammario, Bianchi Claudia Letizia, Cappelletti Giuseppe, Roveri Norberto. Amino acid synergetic effect on structure, morphology and surface properties of biomimetic apatite nanocrystals. ACTA BIOMATERIALIA. *In press.*

2)Roveri Norberto, Battistella Elisa, Bianchi Claudia Letizia, Foltran Ismaela, Foresti Elisabetta, **Iafisco Michele**, Lelli Marco, Naldoni Alberto, Palazzo Barbara, Rimondini Lia. Surface enamel remineralization: biomimetic apatite nanocrystals and fluoride ions different effects. JOURNAL OF NANOMATERIALS. *In press*

3) **Iafisco Michele**, Palazzo Barbara, Roveri Norberto**.** (2009). Interazione tra proteine e substrati inorganici biomimetici. LA CHIMICA E L'INDUSTRIA. vol. Marzo, pp. 104-105.

4) Tigani Domenico, Zolezzi Claudia, Trentani Federico, Ragaini Alessandro, **Iafisco Michele**, Manara Silvia, Palazzo Barbara, Roveri Norberto. (2008). Controlled release of vancomycin from cross-linked gelatine. JOURNAL OF MATERIALS SCIENCE. MATERIALS IN MEDICINE. vol. 19, pp. 1325-1334.

5) **Iafisco Michele**, Palazzo Barbara, Falini Giuseppe, Di Foggia Michele, Bonora Sergio, Nicolis Stefania, Casella Luigi, Roveri Norberto. (2008). Adsorption and Conformational Change of Myoglobin on Biomimetic Hydroxyapatite Nanocrystals Functionalized with Alendronate. LANGMUIR. vol. 24 (9), pp. 4924-4930.

6) Roveri Norberto, Palazzo Barbara, **Iafisco Michele**. (2008). The role of biomimetism in developing nanostructured inorganic matrices for drug delivery. EXPERT OPINION ON DRUG DELIVERY. vol. 5, pp. 861-877

7) Bonora Sergio, Di Foggia Michele, **Iafisco Michele.** (2008). DSC and Raman study on the interaction of DDT [1,1,1-trichloro-2,2-bis(p-chlorophenyl)ethane] with liposomal phospholipids. PESTICIDE BIOCHEMISTRY AND PHYSIOLOGY. vol. 92(3), pp. 144-149

8) Bonora Sergio, Di Foggia Michele, **Iafisco Michele.** (2008). SERS nell'analisi di pesticidi (erbicidi triazinici). LA CHIMICA E L'INDUSTRIA. vol. Dicembre, pp. 98-100

9) Palazzo Barbara, **Iafisco Michele**, Laforgia Mariarita, Margiotta Nicola, Natile Giovanni, Walsh Dominic, Mann Stephen , Bianchi Claudia Letizia, Roveri Norberto. (2007). Hydroxyapatite nanocrystals as local anticancer platinum complexes delivery system. ADVANCED FUNCTIONAL MATERIALS. vol. 17, pp. 2180–2188.

10) Rimondini Lia, Palazzo Barbara, **Iafisco Michele**, Canegallo Lorenza, Demarosi Federica, Merlo Michela, Roveri Norberto. (2007). The remineralizing effect of carbonate-hydroxyapatite nanocrystals on dentine. MATERIALS SCIENCE FORUM. vol. 539-543, pp. 602-605

11) Sabatino Piera, Casella Luigi, Granata Alessandro, **Iafisco Michele**, Lesci Isidoro Giorgio, Monzani Enrico, Roveri Norberto. (2007). Synthetic chrysotile nanocrystals as a reference standard to investigate surface-induced serum albumin structural modifications. JOURNAL OF COLLOID AND INTERFACE SCIENCE. vol. 314(2), pp. 389–397.

12) Palazzo Barbara, Roveri Norberto, **Iafisco Michele**, Rimondini Lia, Gazzaniga Giancarlo. (2007). Biologically active nanoparticles of a carbonate-substituted hydroxyapatite, process for their preparation and composition incorporating the same. WO 2007/137606 A1. COSWELL.